Chair of Physical Metallurgy and Metallic Materials

Doctoral Thesis

Investigation into the mechanical character of grain boundaries in technically pure and micro-doped molybdenum

Dipl.-Ing. Severin Jakob, BSc

August 2021

MONTANUNIVERSITÄT LEOBEN
www.unileoben.ac.at

AFFIDAVIT

I declare on oath that I wrote this thesis independently, did not use other than the specified sources and aids, and did not otherwise use any unauthorized aids.

I declare that I have read, understood, and complied with the guidelines of the senate of the Montanuniversität Leoben for "Good Scientific Practice".

Furthermore, I declare that the electronic and printed version of the submitted thesis are identical, both, formally and with regard to content.

Date 19.08.2021

Signature Author
Severin Jakob

Acknowledgments

First and foremost, I want to thank my supervisors Priv.-Doz. Dr.-Ing. Verena Maier-Kiener and Univ.-Prof. Dr.mont. Helmut Clemens from the Department Materials Science of the Montanuniversität Leoben as well as Univ.-Prof. Dr.mont. Reinhard Pippan of the Erich Schmid Institute of Materials Science of the Austrian Academy of Sciences for their support, guidance and discussions throughout the work on this thesis. Furthermore, thanks to Dr.mont. Alexander Leitner for his supervision and support especially during Nanoindentation experiments.

I want to express my gratitude to Dr.mont. Wolfram Knabl, Dr.mont. Alexander Lorich and Dr.mont. Michael Eidenberger-Schober from the industrial partner Plansee SE for their trust in me and the starting point for this work. I very much enjoyed the cooperation. During the project meetings, everybody's expertise was pooled together in an amicable atmosphere and the goal was always to further the knowledge about the refractory metal Mo.

The support and initiative of Dr.mont. Anton Hohenwarter during the bending tests at the Erich Schmid Institute are highly appreciated, especially during the time of a global health crisis, when experiments in the lab and in-person meetings were restricted.

I would like to thank the former and current members of the 'MEH' research group. Dr.mont. Katharina Leitner made it easy to build upon her distinguishing work on the chemical composition of Mo grain boundaries. Dipl.-Ing. Anna Sophie Ebner, Dr.mont. Johann Kappacher and Dipl.-Ing. Maximilian Siller ensured a fun and collegial atmosphere in this generation of future PhDs. Now it is time for Dipl.-Ing. Gerald Schaffar, Dipl.-Ing. Lea Lumper and Dipl.-Ing. Michael Sommerauer to inspire the scientific community.

Special thanks to the 'Suppen'-Crew and especially Dr.mont. Mathias Hofinger. A 'Thank you' for the jovial and/or technical discussions at the table further extends to Dr.mont. Irmgard Weissensteiner, Dr.-Ing. Andreas Landefeld, Dr.mont. Christina Hofer and more friends and colleagues from the department.

I would like to extend my thanks to Thomas Weissenböck, BSc who performed a large part of bending tests and was the second examiner for crack tip opening angles during his Bachelor's degree. The cooperation with mutual respect is ongoing for his Master's thesis.

Last but not least, I want to express my gratitude to my family and friends as well as my girlfriend. Without their support and patience, the journey would have been far more demanding.

Abstract

Technically pure Mo has a broad field of applications. It has a high melting point of 2620°C with no phase transformation. Therefore, its physical and mechanical/technological properties experience no abrupt changes up to elevated temperatures. Furthermore, the high electrical and thermal conductivity in combination with a low thermal expansion coefficient offers unique functional applications. The limiting factor as a structural material is, beside a brittle-to-ductile transition somewhere around room temperature, the tendency for brittle intercrystalline failure at low temperatures. Modern grain boundary engineering and in particular segregation engineering offers the possibility to mitigate this Achilles' heel. The addition of B and/or C in small amounts to technically pure Mo is known to enhance the cohesion of grain boundaries and changes the fracture mode from intercrystalline to transcrystalline failure. So far, only this qualitative comparison has been described.

In this thesis, the chemical composition of the recrystallization front on semi-recrystallized samples is explored by atom probe tomography and diffusion considerations. The main part of this work deals with the mechanical response of grain boundaries. Investigations were carried out with micromechanical testing methods, such as nanoindentation, pillar compression and micro-sized bending beams on technically pure Mo and B micro-doped Mo. The possible influences during instrumented hardness testing at or near grain boundaries are elucidated and the crucial impact of indenter shape and rotation angle in combination with grain orientation is discussed. Pillar compression is performed to analyze slip transfer at the grain boundary and criteria for a comparison between material variants are presented. Experimentation on micro-sized bending beams is carried out on cantilevers with and without the introduction of a sharp notch. The amount of plastic deformation before fracture at a grain boundary might give insight into the resistance to tensile loading of the interface.

Moreover, a new meso-scale approach to examine crack initiation on the tensile-loaded extreme fiber of mm-sized bending samples is presented. In this way, a large number of grain boundaries are loaded and the influence of individual grain orientation pairings is negligible. The length of separated grain boundaries is measured on scanning electron micrographs and put into context to the total boundary length per sample area. The addition of B reduces the relative length of separated boundaries to one third, when comparing

samples with similar microstructures. Furthermore, the grain boundaries' propensity to fracture is analyzed concerning possible slip transmission at the interface and cross-checked with the appearance of cracks. A distinct differentiation of regimes is apparent at 30° misorientation of the grain boundaries. 90% of cracks are at higher misorientation, which also correlates with a reduced potential for slip transmission.

The meso-scale testing approach was applied to industrial-scale quality control. Samples from semi-finished mill products were tested at the equipment of the industrial partner and appearing cracks were investigated. They show the same tendency towards lesser relative crack length in samples with B additions.

Zusammenfassung

Das Refraktärmetall Mo hat durch seine physikalischen und mechanisch/technologischen Eigenschaften ein breites Anwendungsfeld. Es zeigt keine Phasenumwandlung bis zur Schmelztemperatur von 2620°C und daher auch keine plötzliche Veränderung in seinen Eigenschaften bis zu erhöhten Temperaturen. Die hohe elektrische und thermische Leitfähigkeit in Kombination mit einem geringen Wärmeausdehnungs-koeffizienten erlaubt einzigartige Einsatzmöglichkeiten. Begrenzt wird das Anwendungsfeld als Strukturwerkstoff durch eine Spröd-Duktil-Übergangstemperatur, welche im Bereich der Raumtemperatur liegt, und durch welche eine Neigung zu interkristallinem Sprödbruch bei tiefen Temperaturen resultiert. Moderne Technologien erlauben das gezielte Einstellen der chemischen Belegung der Korngrenzen, um die Kohäsion der Grenzflächen zu verbessern. Die Zugabe kleinster Mengen von B und/oder C zu technisch reinem Mo führt zu einem Übergang von interkristallinem zu transkristallinem Bruchbild. Bis jetzt wurde nur dieses qualitative Kriterium zur Darstellung der verbesserten Korngrenzkohäsion beschrieben.

In dieser Arbeit wurden die chemische Beschaffenheit der Rekristallisationsfront mittels Atomsondentomographie sowie eine Abschätzung zu Diffusionswegen untersucht. Der Hauptteil der Arbeit beschäftigt sich mit dem mechanischen Verhalten von Korngrenzen. Zum einen wurden mikromechanische Testmethoden wie Nanoindentation, Mikrosäulen-Druckversuche sowie Mikrometer große Biegebalken an technisch reinem und mit B mikrodotiertem Mo durchgeführt. Die Einflüsse während instrumentierter Härtemessungen werden beschrieben und der entscheidende Einfluss der Prüfkörperform und des Rotationswinkels in Bezug zur Kornorientierung werden diskutiert. Mikrosäulen-Druckversuche wurden genutzt, um die Übertragung von Gleitung an Kristallebenen über die Korngrenze hinweg zu beschreiben. Notwendige Kriterien zur Vergleichbarkeit von Mikrosäulen an unterschiedlichen Materialien werden beschrieben. Es wurden außerdem Biegebalken mit und ohne eine scharfe Kerbe gezielt verformt. Die plastische Verformung vor dem Bruch könnte Aufschlüsse über die Kohäsion der Korngrenze geben.

Darüber hinaus wurde eine neuartige Methodik zur Untersuchung der ersten Schädigung der Korngrenzen an Millimeter großen Biegeproben entwickelt. Durch diese Herangehensweise auf der Meso-Skala können viele Korngrenzen gleichzeitig belastet werden. Die Länge der offenen Korngrenzen wurde an Panorama-Aufnahmen eines

Rasterelektronenmikroskops vermessen und in Relation zur gesamten Korngrenzlänge gesetzt. An Proben mit B-Dotierung und mit technisch reinem Mo vergleichbarer Mikrostruktur ist der Anteil offener Korngrenzen auf ein Drittel reduziert. Des Weiteren wurde die Möglichkeit für Gleitübertragung an den Korngrenzen untersucht. Es zeigt sich ein Rückgang zu verminderter Verformungsübertragung von einem Korn auf das andere ab einer Korngrenzen-Missorientierung von 30°. Dieser Wert stimmt mit einem erhöhten Auftreten von beobachteten Rissen an Korngrenzen mit hohen Missorientierungen überein.

Die entwickelte Methodik zur Untersuchung der Korngrenzschädigung an Millimeter großen Proben wurde an Blechen aus dem Produktionsprozess angewandt. Die Biegeversuche wurden an den Geräten des Industriepartners durchgeführt und die untersuchten Oberflächen der Biegeproben zeigen dieselbe Tendenz zu verminderter Rissneigung an B-dotierten Proben.

Content

Abbreviations

APT	atom probe tomography
bcc	body-centered cubic
BDT	brittle to ductile transition
BDTT	brittle to ductile transition temperature
BSE	backscattered electrons
CSM	continuous stiffness measurement
CTOA	crack tip opening angle
DIC	differential interference contrast
EBSD	electron backscatter diffraction
fcc	face-centered cubic
FIB	focused ion beam
GB	grain boundary
GROD	grain reference orientation deviation
IFE	interfacial excess
IPF	inverse pole figure
IQ	image quality
K&W	Kammrath and Weiß
LOM	light optical microscope
LSCM	laser scanning confocal microscope
ND	normal direction
RD	rolling direction
RT	room temperature
RX	recrystallized grain
SE	strength of embrittlement
SEM	scanning electron microscope
SR	stress-relieved grain
TD	transverse direction

List of symbols

H	hardness
P_{max}	maximum load
A_r	residual indentation area
E_r	reduced modulus
β	geometry factor
S	stiffness
A_p	projected area
h_c	contact depth
$\nu_{i,s}$	Poisson ratio of indenter/sample
$E_{i,s}$	Young's modulus of indenter/sample
$\overrightarrow{b_{in}}$, $\overrightarrow{b_{out}}$	Burgers vectors of incoming and outgoing slip systems
$\overrightarrow{b_r}$	residual Burgers vector
d_{in}, d_{out}	incoming and outgoing slip directions
l_{in}, l_{out}	intersection lines of slip planes and grain boundary
γ	angle between n_{in} and d_{out}
δ	angle between d_{in} and n_{out}
θ	angle between l_{in} and l_{out}
κ	angle between d_{in} and d_{out}
ψ	angle between n_{in} and n_{out}
N	N-factor criterion
LRB	criterion including intersection lines
m'	m'-parameter for slip transfer
D	diffusion coefficient
D_0	diffusion pre-factor
Q	activation energy
R	universal gas constant; indenter radius
T	absolute temperature
x	diffusion distance; distance towards the grain boundary
t	annealing time
ϕ_1, Φ, ϕ_2	Euler-Bunge angles
α	Rotation angle
P	indentation load
h	indentation depth
τ	shear stress
P_{Pop-in}	load at pop-in
σ_r	representative indentation stress
C^*	constrain factor
y	hardness fit function
y_0	hardness fit far from the boundary
A	scaling factor
w	length scaling parameter
ΔH_{a_c}	relative hardness increase
a_c	contact radius
φ	misorientation
A_{real}	contact area with delayed surface detection
h_s	distance between sample surface plane and surface detection
$A_{apparent}$	seeming contact area
A_{true}	actual contact area
E_{ref}	reference Young's modulus
STr	slip transfer parameter
m_{in}, m_{out}	Schmid-factor of incoming and outgoing slip systems

1. Motivation & Scope of work

Molybdenum (Mo) is an essential material in our modern life, but rarely visible to the eyes of the everyday user. It is a refractory metal with a high melting point of 2620 °C and high electrical and thermal conductivity while having a low thermal expansion coefficient. These physical and mechanical properties are highly advantageous for its applications. On the one hand, it is often used as functional part of more complex devices. For example, the conducting electrodes/data lines in displays for smartphones up to large liquid crystal displays are made of Mo via thin film deposition. Another example are X-ray tubes, where the main body of the rotating anode is composed of a Mo-based alloy with a small W-Re layer on top for the generation of X-rays. Further applications are heat sinks for microelectronics and feedthroughs in lighting devices. On the other hand, Mo is used during production processes for instance as extrusion molds or forging dies. The glass industry employs Mo for melting electrodes, claddings and mixing tools because of its corrosion resistance against molten glass. The same is true for crucibles for the production of sapphire single crystals. The high-temperature strength is further utilized for furnace equipment such as charge carriers, heating elements and shieldings. [1–3]

Mo has a broad field of application at elevated temperatures. However, the use at moderate to low temperatures is to a certain extent limited due to its plastic deformation capability. The crystal structure of Mo is body-centered cubic (bcc) and therefore it has a brittle to ductile transition (BDT). This transition temperature lies, depending on the processing state and the testing conditions, at or around room temperature (RT). Especially in the recrystallized state, Mo tends to fail brittle in the manner of intercrystalline fracture without extensive plastic deformation [4,5]. Intrinsically weak grain boundaries (GBs) as well as the decoration of them with segregation elements are responsible for this behavior [6–8]. In recent investigations, technically pure Mo was intentionally doped with boron as well as carbon to enhance the cohesion of the GBs [9]. The success of this approach was qualitatively demonstrated by a change in fracture behavior from intercrystalline to transcrystalline fracture in combination with atom probe tomography (APT) measurements of the GB chemistry and reduction of the brittle to ductile transition temperature (BDTT) [9,10].

One aspect of the chemistry of GBs is yet to be elucidated, namely the role of the recrystallization front on the distribution of segregations. Subsequently to the chemical characterization of the interfaces, the mechanical structure of GBs is of interest. A comprehensive method to measure the interface cohesion strength and support the qualitative phenomenon of enhanced GBs is desired to further understand GB decohesion in Mo. Therefore, in this work, micromechanical methods such as deformation of bending beams, pillar compression and nanoindentation were employed on technically pure and micro-doped Mo. Furthermore, meso-scale bending experiments on mm-sized specimens were performed to investigate early stages of crack initiation and propagation.

This thesis aims to provide knowledge on the potential application of different micro- and meso-scale characterization techniques to study the mechanical behavior of GBs and their cohesion in technically pure and micro-doped Mo.

2. State of the art

Mo is a refractory metal in the group VI of the periodic table. The term 'refractory' derives from the latin *refractarius* which means stubborn. Mo has earned its place in this group of metals with its high melting point of 2620°C. Other remarkable physical properties are high thermal and electric conductivity and a low coefficient of thermal expansion. It has no phase transformation and therefore experiences no abrupt degradation of its mechanical/technological properties up to its recrystallization temperature [1,11]. Mo shows good resistance against molten glass as well as molten metals and a variety of chemicals. It is therefore used for crucibles for sapphire crystals, claddings and melt stirrer in the glass industry as well as for components in lighting, electronics or thin film technologies [2]. However, precautions have to be implemented for high temperature applications, since it forms volatile MoO_3 above 500°C in air. The downside of Mo for its application is the limited deformability at low temperatures. It has a BDTT depending on the processing state and the testing conditions at or about RT [4,5,12,13].

Most of the industrial production of Mo involves roasting of the sulfidic ore, purifying the oxide in a chemical plant and a two-step reduction of the oxide with dry hydrogen, followed by cold isostatic pressing and sintering under protective atmosphere (i.e. fabrication via the powder metallurgy route). The sintered ingot then receives its thermo-mechanical deformation to achieve full density as well as the desired dimensions and grain structure. During the sheet production in a first deformation step, the ingot is hot-rolled at temperatures above 1000°C and followed by subsequent deformation steps at lower temperatures. In the final step, the Mo sheet is cold-rolled at RT to the dimensions of the wanted semi-finished product [3,14]. The schematic steps of the production sequence are illustrated in Fig. 2.1. Alternatively, a pressed ingot can be used as an electrode and arc-melted to achieve a highly dense and pure material. However, the resulting large grain size impairs the workability of the cast ingot. [2]

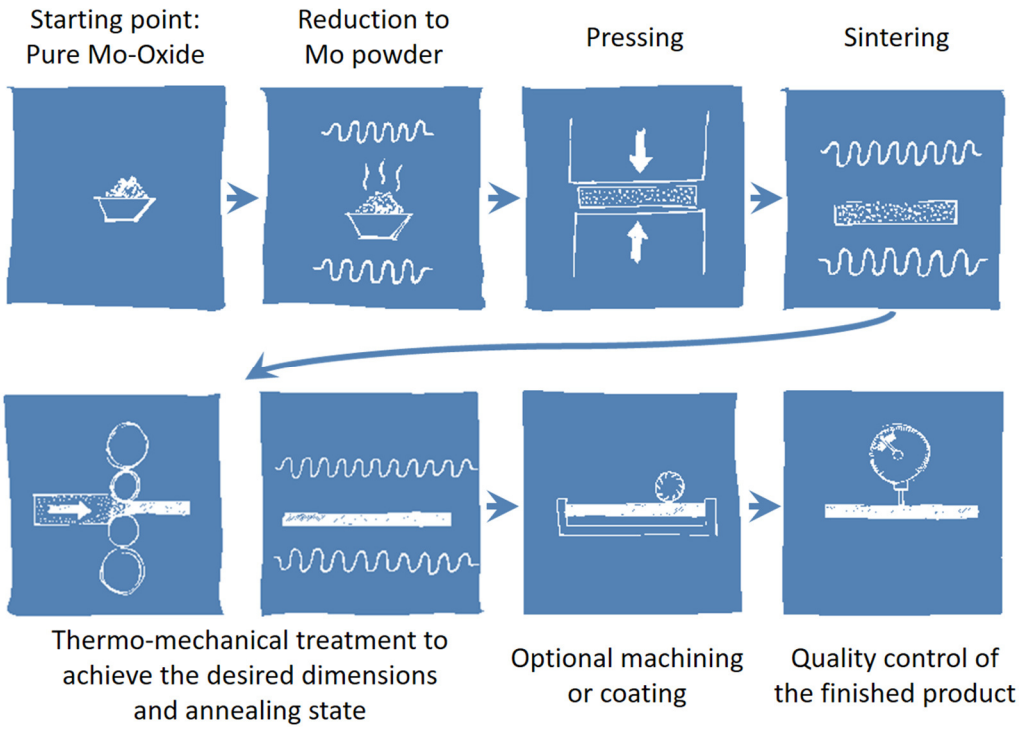

Fig. 2.1: Schematic representation of the processing steps during the fabrication of Mo products via powder metallurgy. [15]

Because of its functional and thermo-mechanical properties, Mo has a wide range of applications. However, the brittle failure mode at low temperatures, mostly via intergranular fracture, limits its use as structural material in this temperature regime as well as the workability during deformation or subsequent forming processes.

2.1. Intrinsic brittleness of Mo

Mo has a bcc crystal structure and as such a BDT. Depending on the processing state, this transition lies at or even above RT. In contrast to other metals, Mo gains a better formability in the deformed state compared to recrystallized Mo [4,16,17]. Especially in the recrystallized state, fracture in its brittle regime occurs in intercrystalline fashion along the GBs. In literature one aspect for Mo's tendency to fracture preferentially in intercrystalline manner is presumed to be intrinsically weak GBs [7,12,18,19]. These studies have found that the fracture stress of the GB depends on the misorientation and correlates well with the GB

energy. *Ab-initio* calculation of a variety of GBs in Mo, W and Fe show that both Mo and W have higher GB energies, and therefore weaker interfaces, than Fe with similar trend depending on the crystal orientations for all three elements [6]. Furthermore, the investigation supports the tendency of Mo and especially W for intercrystalline fracture. Therefore, efforts were taken to eliminate the proportion of weak random GBs and increase the share of low coincidence site lattice boundaries [20–22]. Tsurekawa et al. showed that the fracture strength of a polycrystal could be enhanced by increasing the frequency of low energy GBs like small-angle GBs and low sigma boundaries. Also specific texture development to achieve more favorable GB configurations were tried [22]. The aforementioned approaches can be summarized under the term 'GB engineering' [21,23,24]. The goal is to limit the number of GBs that are susceptible for damage initiation in the microstructure.

2.2. Effect of segregations

The second aspect playing a major role for the brittleness of Mo are the segregations at the GBs [8,10,25–27]. It is impossible to eliminate all impurities whether the production route is based on powder metallurgy or arc-melting. The amounts of these impurities are in the range of µg/g. Table 1 depicts a typical chemical composition of technically pure Mo.

Table 1: Typical impurities of technically pure, powder metallurgical Mo.

Element	**W[a]**	**O[b]**	**N[b]**	**C[c]**	**P[a]**	**S[c]**	**K[a]**	**Fe[a]**	**Si[d]**	**Zr[a]**
Content [µg/g]	152	18	<5	17	<10	<5	6	7	<5	<5

a…Inductively coupled plasma-atomic emission spectrometry, b...Carrier-gas analyses, c...Combustion analyses, d...Graphite tube-atomic adsorption spectrometry

Depending on the element and its properties in regard to Mo, different solubility is expected. W is a substitutional impurity and has a high solubility. However, other elements like O, N and C have a low solubility and therefore a high tendency to segregate to regions

with more atomic spacing like GBs, see Fig. 2.2a [28–30]. The amount of segregation elements further depends on the type of boundary [31,32].

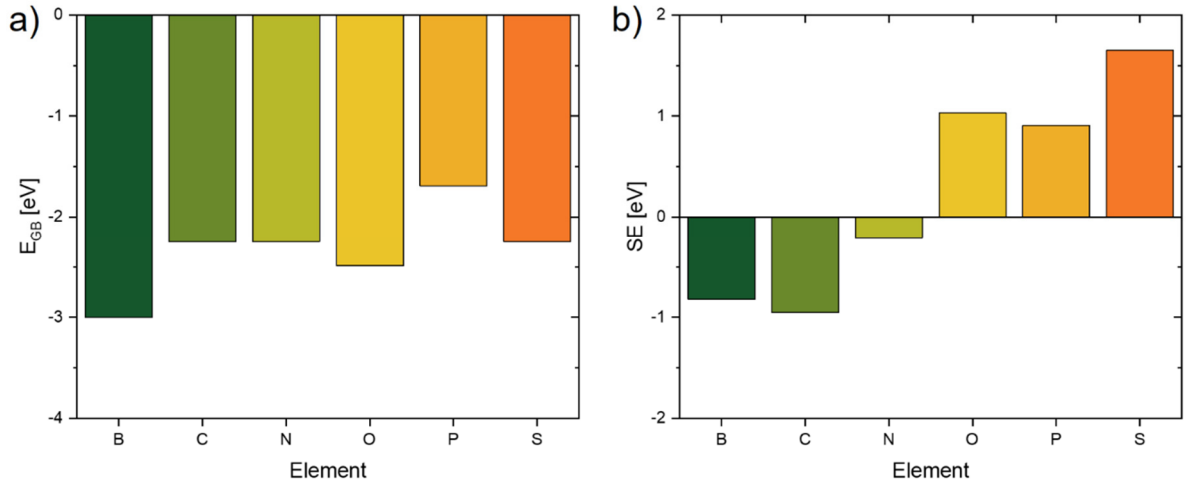

Fig. 2.2: a) Segregation energies to interstitial lattice positions at the GB according to [30]*. b) Strength of embrittlement (SE) for the GB with segregations. Values <0 represent improved cohesion of the interface whereas positive values promote decohesion.*

In literature, a lot of studies document the detrimental effect of O and a beneficial effect of C on the cohesion of interfaces [8,12,33–37]. Already at the end of the 1960s, studies suggested the beneficial effect of C on the GBs [38,39]. Other studies investigated additionally the influence of different elements, showing beneficial impact of B and Re, and brittle fracture with Si additions [40–42]. Miller and coworkers suggested a beneficial effect of Zr and B alongside C on the ductility of Mo weldments with reduced O and N at the GB [34,43]. More recent investigations by Leitner et al. [10] demonstrate the enhancement of the GBs by a change in fracture mode from intercrystalline to transcrystalline fracture. The changed fracture behavior could be linked to increased amounts of C and a reduced share of O at the GBs, measured by APT. One such measurement of a GB is shown in Fig. 2.3. The interface is enriched by C and to a smaller amount B, whereas O and N are almost not present (Fig. 2.3c).

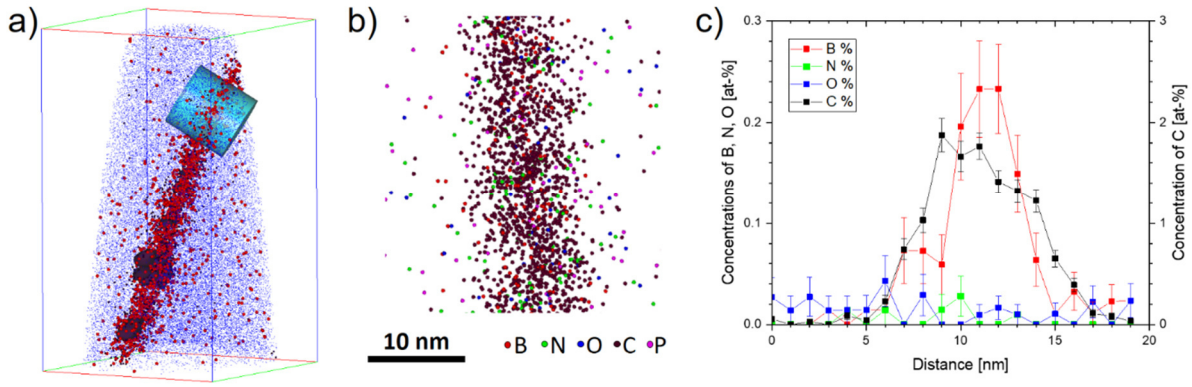

Fig. 2.3: Measurement of a Mo GB with APT. a) Reconstruction of the tip with cylindrical region of interest perpendicular to the interface. b) Detail of the segregation elements at the GB; c) Concentration profile along the region of interest. Note, that the scale for C is different. Adaptation from [10].

The improvement of computational resources in the last decades has opened up the possibility to investigate interface cohesion from an atomistic standpoint. Simulations can help to inform, where impurity element sites are located and how the interface energy is influenced [44–46]. Scheiber et al. [30,47] performed *ab-initio* calculations to not only analyze the segregation tendency of different impurity elements, but also the influence on the interface cohesion. Segregation energies and the effect on interface cohesion are depicted for selected elements in Fig. 2.2. The calculated work of separation, labelled also strength of embrittlement (SE), showed a beneficial effect for impurities like B and C. Detrimental to the GB cohesion are foremost O but also S and P. N seems to have only a minor influence on GB cohesion. Further calculations investigated the impact of interactions of different solutes in Mo as well as effects such as favored clustering and site-competition. Especially B has a strong segregation tendency that leads to the suppression of O segregation [48,49].

Insights like that provide the basis for GB segregation engineering, where the chemistry of the material is finely tuned by micro-doping GB enhancing elements. For instance Leitner et al. showed the improved ductility of sintered Mo by C and B additions, see [9].

2.3. Micromechanical testing methods

Normally the mechanical properties for example flow stress, strain to failure, ultimate tensile strength etc. of an alloy or a material are assessed by standardized tests like the uniform tensile test. These tests evaluate the overall bulk material behavior and therefore average the strength and deformation of a multitude of grains for most microstructures. However, modern high performance materials often consist of a fine microstructure with components ranging from a few nanometers to micrometers. To understand the deformation and failure processes the mechanical parameters of the individual constituents are useful information. The development of testing instrumentation at these length scales in the last two decades, especially instrumented hardness testing or nanoindentation, has enabled miniaturized mechanical testing. With the employment of focused ion beam (FIB) milling micro-sample geometries for compression, tension and bending can be fabricated. Therefore, the deduction of mechanical parameters like flow stress, tensile and compressive strain or fracture toughness at the micro-scale is possible. However, since the sample dimensions are no longer in the same order as for standardized tests, special focus has to be placed on validation of the experiments. A thorough review article of Dehm et al. [50] discusses the development and critical issues regarding testing of miniaturized samples with special regard to interfaces.

2.3.1. Nanoindentation

Instrumented hardness testing or nanoindentation has received great technological and methodical progress over the last decades. It is now a versatile tool to probe material properties on the micro-scale and offers fast testing with a high spatial resolution of indents. Fig. 2.4 depicts the two most applied indenter geometries. A three-sided pyramid with an opening angle of 65.3° is known as a Berkovich indenter and has the same projected area as a Vickers indenter (Fig. 2.4a). The rounded tip of a conical indenter tip is used for spherical indentation, as schematically depicted in Fig. 2.4b. Modern nanoindentation devices can perform indentations to a few tens of nanometers up to a few micrometers indentation depth with a force resolution of µN and sub-nanometer displacement-resolution. From the loading

and unloading load/displacement data, hardness and Young's modulus can be deduced by the method of Oliver and Pharr [51]. Fig 2.5 depicts a schematic drawing of an indentation experiment and the involved calculation for material data.

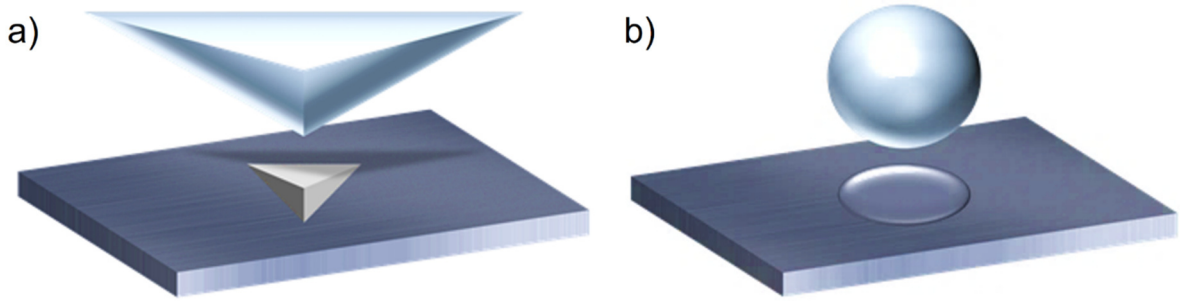

Fig. 2.4: Typical indentation geometries. a) 3-sided pyramidal Berkovich indenter and b) schematic representation of spherical indentation.

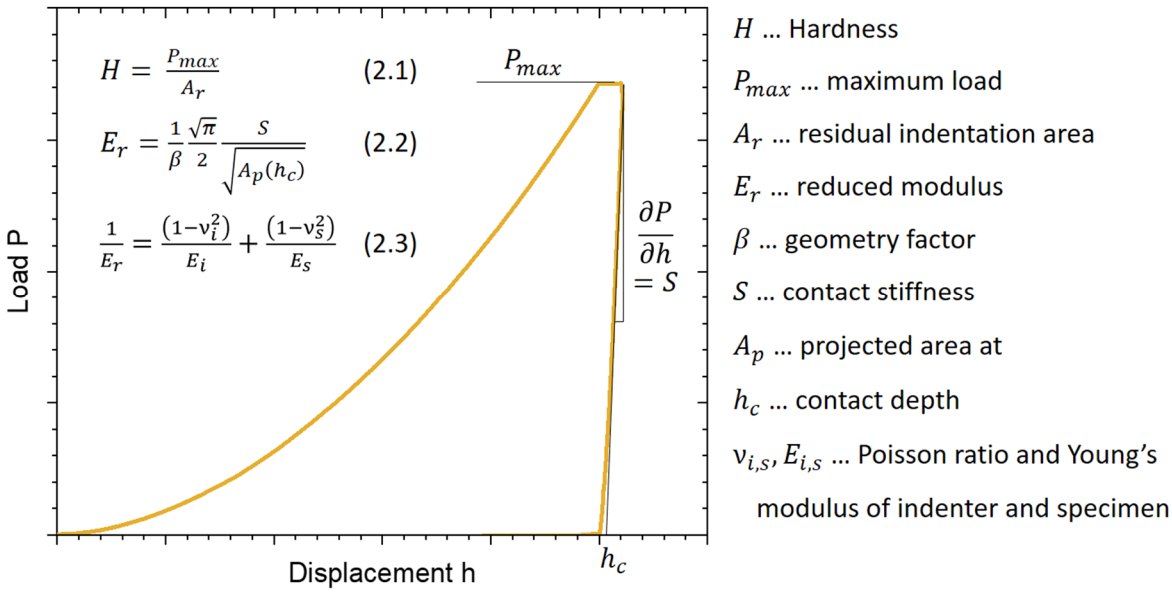

Fig. 2.5: Schematic load-displacement data of an indentation with a Berkovich tip. Relevant formulas for data evaluation are included, for details see [51].

State-of-the-art instruments provide apart from the classic 'static' indentation also dynamic indentation methods. There, the indentation motion is overlaid with a small oscillating displacement and the phase shift of this oscillation-frequency is used for

computation of the current material stiffness [52,53]. When applying so-called Continuous Stiffness Measurement (CSM), modulus and hardness data can be measured continuously during an experiment (see for example Fig. 2.6). The hardness decreases with increasing indentation depth, which is known as indentation size effect, caused by the large strain gradient at small indentation depths due to geometrically necessary dislocations [54,55]. For bulk materials, the indentation modulus should not change during the experiment with increasing displacement and can give further an indication of a valid measurement as it is the case in Fig. 2.6. Beside continuous measurement of hardness and indentation modulus, also the strain rate sensitivity and creep properties can be investigated with modified nanoindentation methods [56].

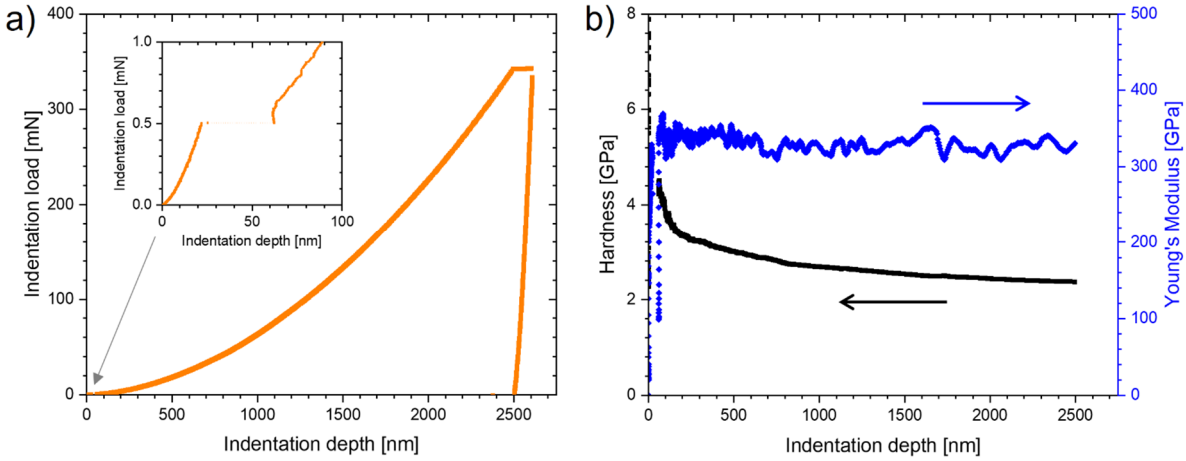

Fig. 2.6: Typical indentation experiment data with CSM. a) Measurement data of indentation load as a function of indentation depth. The inset in (a) shows the initial pop-in, indicative of a low dislocation density in the material. b) Hardness and modulus data can be examined through the whole experiment.

Beside the classic Berkovich indenter tip, spherical indentation has seen a lot of progress in the last couple of years. The average deformation is dependent on the opening angle of the indenter tip. Self-similar indentation geometries like pyramidal indenters (including a Berkovich tip) introduce a self-similar deformation field under the indent. In contrast, spherical indentation introduces different opening angles depending on the tip radius and indentation depth. The deeper the indentation the higher average strain acts on the probed material. This allows with careful calibration of the tip geometry the recording of

a stress-strain curve, since the average deformation under the tip is increasing with the indentation depth [57–59]. A Berkovich indenter with 65.3° opening half-angle represents 7.8% average strain.

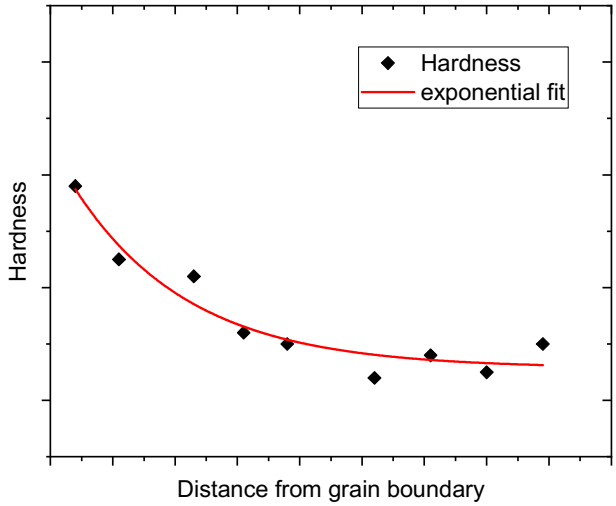

Fig. 2.7: Schematic representation of increased hardness in proximity of a GB. At enough distance from the interface the hardness values match the bulk hardness.

Literature regarding the micro hardness testing in proximity of a GB has shown an increase towards the boundary, schematically illustrated in Fig. 2.7 [60–63]. With improving technologies, modern nanoindentation allows for better spatial resolution due to smaller imprints as well as high through-put of examination [64]. Studies have been performed on different metals with pyramidal [65–68] as well as spherical indentation geometries [69,70]. In the majority of experiments, an increase of hardness in close proximity to the GB is reported. However, the deviations at the GB from the hardness in the grain interior are not unison towards higher hardness, see for example [65,67]. One study by Weaver et al. [71] performed indentations with a Berkovich tip as well as spherical indentation on the same GBs of shock-loaded Ta. They identified in one case an increase in hardness for both Berkovich and spherical indentation. At another GB with similar misorientation, a decrease in measured hardness during Berkovich indentation was reported and the spherical indentations on this specific GB showed inclination towards higher hardness. A low-angle GB examined no hardness deviation in comparison to the grain interior.

For recrystallized metals, a displacement burst at the beginning of indentation experiments results from the transition of elastic to plastic deformation [72,73]. Since the tested volume is so small, the first probed volume is possibly free of any defects. In this case the theoretical strength of the material is needed to introduce the first dislocation [74]. If dislocations are still present in the tested volume the pop-in load is lowered [75]. GBs are believed to be a source of dislocations and the onset of displacement burst at lower forces can be observed during indentation at or near the interface [67,76–78].

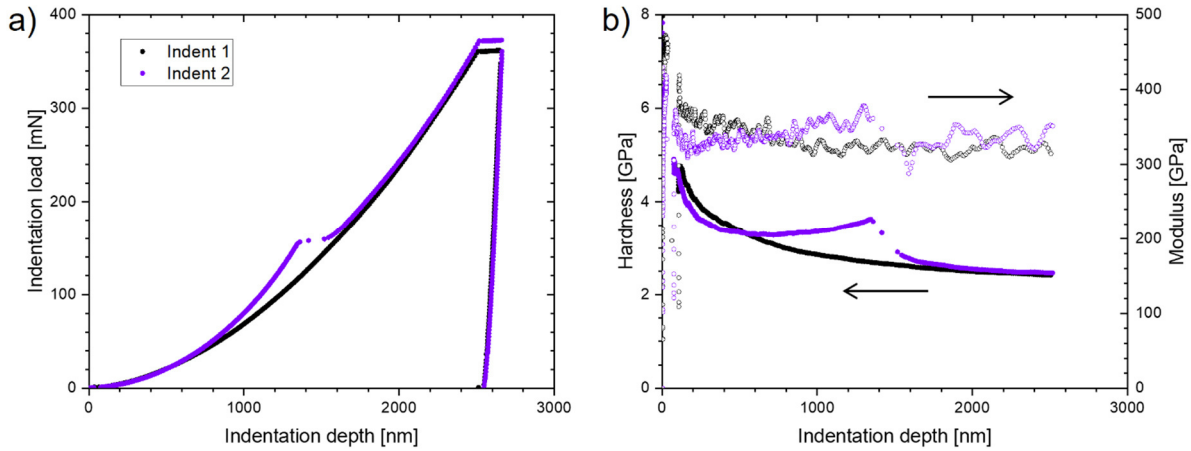

Fig. 2.8: a) Load as a function of indentation depth for indents with (Indent 2) and without (Indent 1) a GB pop-in event. b) Hardness (solid symbols) and modulus (open symbols) data for the two indentations.

Another phenomenon of dislocation burst during nanoindentation near GBs was observed for bcc metals [67,77,79]. A hardness increase is measured before a sudden jump in displacement reduces the hardness back to the plateau of the grain interior. This second displacement burst is called ‘GB pop-in’ and is exemplarily depicted in Fig. 2.8. It is assumed that the GB pop-in originates from impeded dislocation motion at the GB until a high enough back stress has accumulated and the resistance of the interface against dislocation motion can be overcome.

2.3.2. Pillar compression

During nanoindentation, the penetration of the indenter tip induces a complex stress and strain field in the material underneath the tip. In contrast to that, the fabrication of micropillars and the use of a flat-punch indenter enable the application of uniaxial stress within the tested volume of the pillar. The sample and indenter during such an experiment are schematically illustrated in Fig. 2.9. Uchic et al. [80] were the first to publish concise stress-strain data derived from such miniaturized uniaxial testing. This could be achieved by alignment of the sample via a goniometer. Beside proper alignment, a high stiffness of the setup is required [81,82]. The reported stresses exceeded macroscopic tests and showed stochastic behavior. This could be explained by the presence or lack of dislocation sources within the tested volume [83]. Furthermore, the possible introduction of artefacts during preparation has to be acknowledged, especially when using the FIB [84,85].

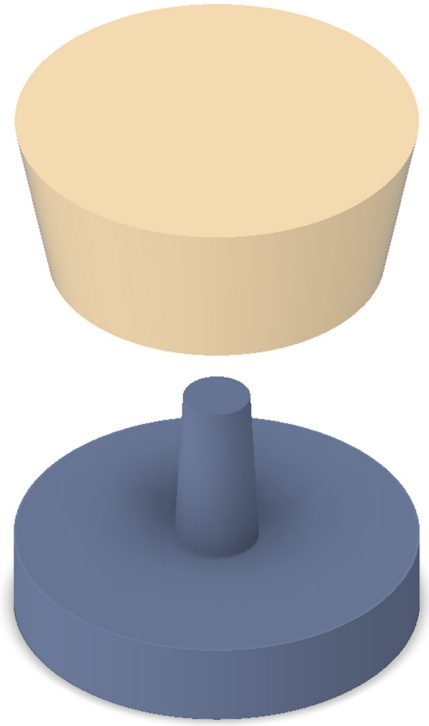

Fig. 2.9: Schematic drawing of a freestanding pillar under a flat-punch indenter. A nanoindenter instrument can record the current load and displacement during the compression of the pillar.

Imrich et al. [86] examined the difference when performing pillar compression on different interfaces. They fabricated rectangular micropillars in Cu with on one hand a twin boundary and on the other hand a high-angle GB. Both interfaces were aligned in the axis of compression. The pillar with the twin boundary shows no noticeable difference in load response in regard to the pillars in the adjacent grains. The pillar with the high-angle GB, however, displayed a strong increase in deformation forces. This could be explained by the GB acting as a dislocation barrier as opposed to the twin boundary. Dislocations were piling up at the GB and increasing the necessary force to deform the micropillar further.

Further investigations on face-centered cubic (fcc) metals deal with the slip behavior of micropillars containing twin and GBs [87–89]. Malyar et al. [90] observed higher stress for bi-crystalline pillars. They attributed this increase in strength to the difference in characteristic length for dislocation motion, which is the pillar diameter in the case of single-crystalline pillars and half the pillar diameter for bi-crystalline pillars. Kheradmand and co-workers [91] identified a strengthening effect of the GB in bi-crystalline pillars from pure Ni samples beyond the mentioned size effect. Further investigations reveal a stronger effect when testing smaller pillars [92]. The character and alignment of the GB is of great impact for slip activation and resulting stress response [93].

To the author's knowledge, studies on micropillars from bcc metals containing a GB are rare. Weaver et al. [94] performed compression tests and slip system analysis on Ta single and bi-crystal micropillars. The investigated high-angle GBs showed varying stress-strain responses and slip transmission behavior. It was shown, that slip transfer was strongly dependent on the particular alignment of involved slip systems. Just recently, Heller et al. [95] reported on the compression of Fe-2.4wt%Si single and bi-crystal micropillars. The higher flow-stress of bi-crystalline samples indicate that the GB acts as an effective barrier for dislocation flow, comparable to the aforementioned study on fcc Cu [90].

2.3.3. Bending beams

Analogous to micropillars, a FIB workstation can be used to fabricate bending beams. A freestanding cantilever can be cut at the edge of a sample or from a wedge sample [96]. More recently, so-called pentagon-shaped cantilevers were developed and used for

micromechanical testing [97–99]. The geometries used in this work are schematically represented in Fig. 2.10. Similarly to micropillars, the beams are deformed by a nanoindenter equipped with a wedge or a pointed indenter. In this case, however, the point of loading leads to a bending stress instead of compression in the specimen. A bending geometry is quite useful to investigate effects of strain and stress gradients within the probed sample [100,101].

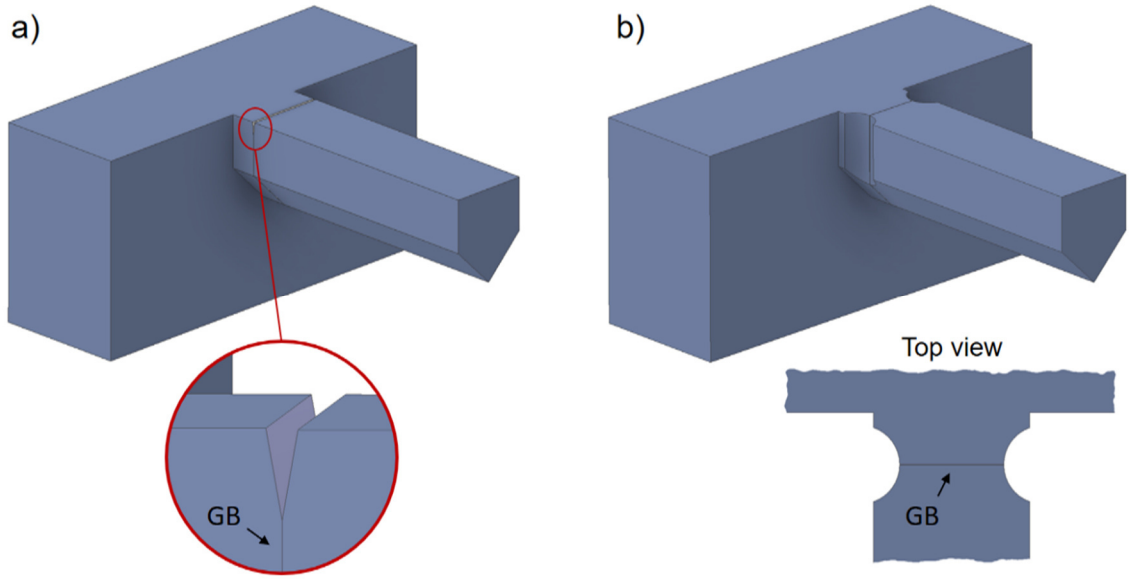

Fig. 2.10: Schematic drawings of pentagon-shaped bending beams with a) a notch cut from the top and b) a bridge-cut to define the weak point near the GB at the base of the beam.

Furthermore, bending beams are used to determine the fracture toughness of materials at the micro-scale. With special care regarding the experimental procedure, the results of micro experiments can be compared to macroscopic toughness values [102,103]. In a lot of fracture tests at the micro-scale, plastic deformation precedes crack propagation and linear elastic fracture mechanics no longer apply. The most used elasto-plastic fracture toughness parameter, the J-integral, requires knowledge of the crack extension during experiment. This crack propagation has to be determined either by *in-situ* experiments in the scanning electron microscope (SEM) or the evaluation of the beam stiffness. Since the elastic response of the beam is dependent on its geometry, a change in cross-section can be detected. Ast et al. [104] used the CSM of their nanoindenter to calculate the crack extension and furthermore the J-integral of NiAl samples. Alfreider et al. [105] performed dynamic

testing of cantilevers *in-situ* in the SEM. They could furthermore show the general applicability of this method.

The use of micro-cantilever as a tool to test mechanical properties is already applied to interfaces [106–111]. The combination of fracture toughness with chemical information is highly desired to understand the interplay between strength and chemical composition at interfaces. Zou et al. [112] performed micro-sized cantilever tests and atom probe tomography on a GB in a high entropy alloy. The observed intercrystalline failure was attributed to formation of oxides and nitrides after impurity segregation to the GB. Hajilou et al. [113] performed cantilever bending on Fe-3wt%Si steel while hydrogen charging to investigate the influence of H on the fracture behavior of GBs.

2.4. Slip transfer phenomenon

Different studies have shown that dislocation glide in one grain can pass over to the adjacent grain if a well aligned slip system is present in the neighboring grain. Apart from geometrical considerations, the resolved shear stress acting on dislocations of a specific crystal plane also play an important role. Fig. 2.11 schematically depicts the geometrical alignment of slip planes and directions at a GB. To evaluate the possibility of slip transfer at the GB, different parameters were presented in literature.

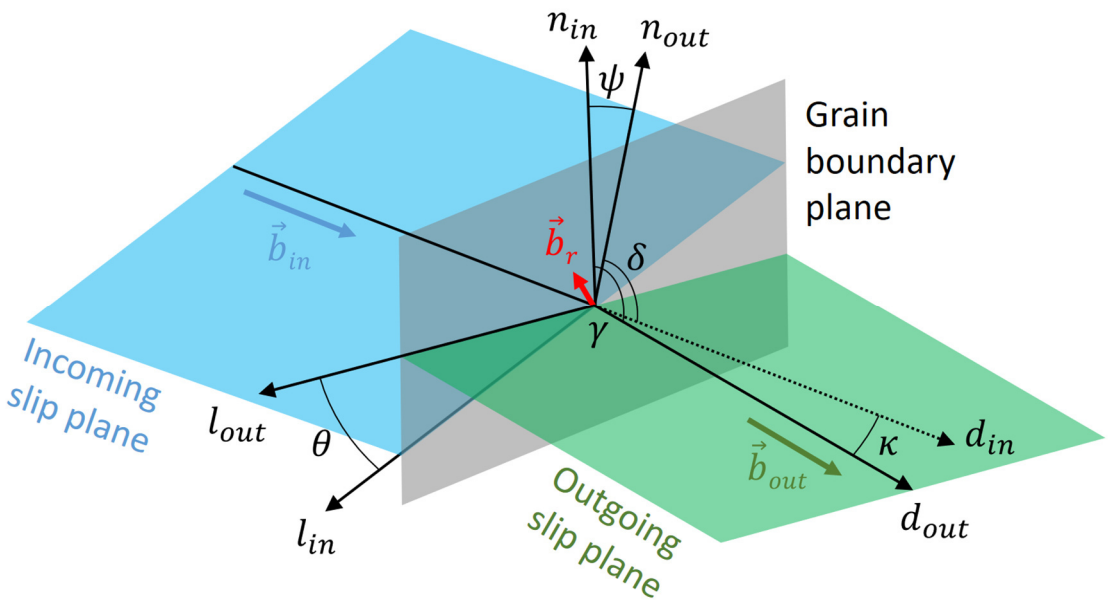

Fig. 2.11: Geometric arrangement of slip planes and directions at a GB.

The first parameter is the so-called N-factor by Livingston and Chalmers [114]. The formulation include the angle between slip planes and slip directions as well as the angles between incoming slip plane with outgoing slip direction and vice versa (see formula 2.4). They performed tension experiments on 24 Al specimens with a GB aligned in the load axis. The authors were able to predict the activated slip system in one grain by association of the primary slip system in the adjacent grain with a high N-factor.

$$N = \cos(\psi)\cos(\kappa) + \cos(\gamma)\cos(\delta) \qquad (2.4)$$

Shen, Wagoner and Clark proposed to minimize the angle between burger vectors, e.g. slip direction, and the angle between the intersection lines of the slip planes with the interface, see formula 2.5 [115,116]. Combining this geometrical consideration with a stress criterion action on the leading dislocation, they were able to predict the slip system in the adjacent grain after slip transmission. If the angle between intersection lines is large, the dislocations have to move a larger distance along the interface until they reach the slip plane of the outgoing slip system. This dislocation movement along the GB is unfavorable and time limiting. If the angles between intersection lines of the incoming and outgoing slip system are well aligned as well as the angle between slip directions is small enough, slip transfer is possible. For this consideration it is necessary to know the inclination of the GB in regard to

the crystal orientations. This information is not accessible from the sample surface. Only with a cross section or during investigations in the TEM, the inclination of the boundary is known.

$$LRB = \cos(\theta)\cos(\kappa) \qquad (2.5)$$

Another important concept for slip transmission is the magnitude of the residual burgers vector. If the dislocation travels through a GB a dislocation in the boundary plane is generated. The size of the burgers vector of this boundary dislocation can be calculated by the difference of burgers vectors of the incoming and outgoing burgers vectors, as described with formula 2.6. Only if the residual burgers vector is low, slip transmission is favored. Lim and Raj [117] studied dislocations impeding on coherent twin boundaries in stainless steel and could correlate slip blockades with a high residual burgers vector. Patriarca et al. [118] investigated the interaction of dislocations with GBs in an FeCr alloy. Strain fields, imaged by digital image correlation, provided insight into the capability of slip transmission or blockade of a GB. The magnitude of the residual burgers vector allowed predictions of slip transmissibility at the GB. Again, the inclination of the boundary has to be known to calculate the residual burgers vector.

$$\overrightarrow{b_r} = \overrightarrow{b_{in}} - \overrightarrow{b_{out}} \qquad (2.6)$$

If one only considers the first part of formula (2.4), it becomes the widely used parameter m' by Luster and Morris [119]. It is probably the most accessible parameter and considers only the angle between incoming and outgoing slip plane as well as the angle between the slip directions (see Fig. 2.11 and formula 2.7). The same idea was already proposed five years earlier by Werner and Prantl [120]. In their paper they proposed a threshold angle of 15° which leads to the same consideration as $m' > 0.93$. The key advantage of this parameter is that only the crystal orientations of the two involving grains have to be known for the calculation. However, the shortfall is the ignorance of the spatial alignment of the interface.

$$m' = \cos(\psi)\cos(\kappa) \qquad (2.7)$$

2.5. Crack initiation at grain boundaries

The last section considered conditions under which dislocations can move from one grain into the adjacent grain. The more common case for random GBs, however, is that the slip systems do not align and slip transfer is restricted at the interface [121–123]. In this case, the dislocation movement is impeded and a pile-up is formed at the boundary. The resulting pile-up stress can shut down the initial dislocation source or activate sources in the adjacent grain. Only if enough slip systems are activated to enable a co-deformation of both involved grains, the material can endure the global strain. If no co-deformation or slip transmission is achieved, the local stresses increase and lead to the failure of the GB, as is depicted in Fig. 2.12 [124].

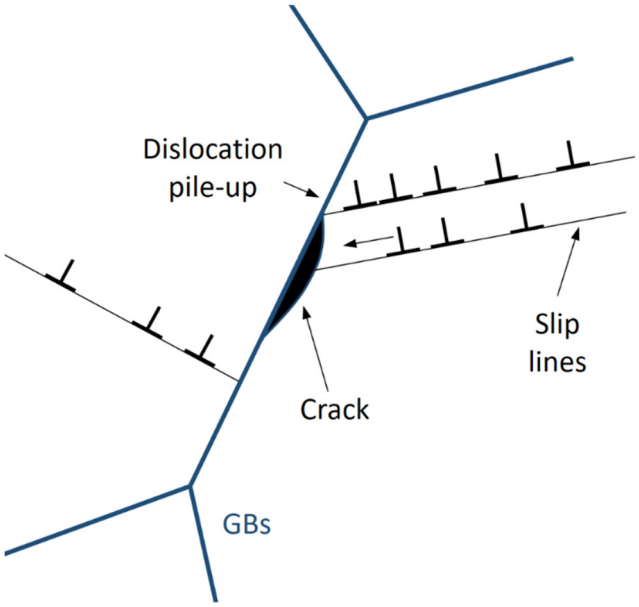

Fig. 2.12: Schematic representation of a mechanically loaded microstructure. The blockage of dislocations at the GB lead to a pile-up and subsequently to a crack at the boundary.

Zhu et al. [125] identified the slip incompatibility and strain localization as the reason for the nucleation of micro-cracks at colony boundaries of a TiAl alloy. Similarly, Knorr et al. [126] assessed the propensity of Σ3 coherent twin boundaries in Ni to crack nucleation during fatigue loading. A combination of slip blockage at the interface with high slip activation in the involved grains could successfully anticipate the occurrence of crack initiation. Bieler et al.

[127] performed four-point-bending tests on mm-sized samples of the bcc metal Ta. They could show that the crystal orientations of adjacent grains play a vital role for the distribution of deformation. In cases where slip lines did not match, ledges between the grains developed during bending deformation.

3. Experimental and methods

The experimental details and methods presented in this section have been partly published by the author in [128] and [129].

The investigated materials were fabricated in industrial-scale manner by the company Plansee SE (Reutte, Austria). Starting point is pure Mo powder, which is pressed and sintered. After sintering, the ingots are hot rolled in several forming steps to achieve semi-finished mill product formats [3]. In this study, samples with two different amounts of deformation were selected for investigations. First, so-called plate material with a thickness of 12.3 mm and second, sheet material with 1.8 mm thickness. One of the investigated materials is technically pure Mo, whereas the other material variant has B additions as a dopant element [130]. However, both materials are within the specifications of technically pure Mo. The different material variants are labelled Mo and MoB for the rest of this work. The amounts of B dopant as well as the other important impurities for the interface cohesion are depicted for the sintered state and the different formats in Table 2. The material variants have been provided in the following thermal conditions: as-worked, stress-relieved, semi-recrystallized, recrystallized and annealed for coarse-grained microstructure.

Table 2: Contents of important segregating elements in the different material variants.

Contents in [µg/g]	**Sintered part**		**Plate**		**Sheet**	
Element	**Mo**	**MoB**	**Mo**	**MoB**	**Mo**	**MoB**
B[a]	<5	20	<5	10	<5	13
C[b]	17	24	12	10	5	14
O[c]	18	10	14	9	20	42

a…Inductively coupled plasma-atomic emission spectrometry, b...Combustion analyses, c...Carrier-gas analyses

For all indentation experiments including pillar compression and bending beams, the recrystallized samples were cut and glued to a special holder to ensure plan parallel top and bottom surfaces. The specimens were ground with SiC abrasive paper down to 2000 grid and 3 µm diamond suspension. In the last preparation step, the deformation layer from polishing was removed by electro-polishing with 12.5 vol.-% H_2SO_4 in ethanol at 25 V for 45 to 90 s. The electro-polishing leads to the formation of GB grooves, which enable to localize the GB in the light-optical microscope (LOM). The topography of the grooves was evaluated with a LEXT OLS4100 laser scanning confocal microscope (LSCM) (Olympus, Tokyo, Japan).

After electro-polishing the samples are ready for indentation experiments. For testing of different geometries like pillars or bending beams, additional preparation steps using focused Ga-ions were carried out with the FEI 3D DualBeam workstation (Thermo Fisher Scientific, Waltham, USA). Pillar were fabricated with milling of successive circle patterns with decreasing ion current from 7 nA to 100 pA at 30 kV acceleration voltage. The pillars had diameters between 1.3 µm and 4 µm and a height of 2 µm to 9 µm. The milling from top causes a slight taper angle of about 3° from the top of the pillar to the base. To prepare bending beams into the surface of the samples the method of cutting pentagon-shaped beams was applied [97]. Similar ion currents as for pillar fabrication were used to mill beams with 3 to 5 µm width and height and about 6 to 12 µm length. The beams were cut free underneath at an angle of 45°.

Electron backscatter diffraction (EBSD) was carried out using the same FEI 3D DualBeam workstation equipped with an EDAX Hikari XP EBSD-system (EDAX Inc., Mahwah, USA; part of AMATEK Materials Analysis Division, AMATEK Inc., Berwyn, USA) to evaluate the microstructure of the samples and the deformation patterns of residual imprints.

For the indentation experiments, a nanoindenter G200 (KLA, Milpitas, USA) equipped with a CSM unit was used. All indentations were conducted at a constant strain rate of 0.05 s^{-1}. A diamond Berkovich tip (Synton-MDP, Nidau, Switzerland) was used to perform reference indentations with a set displacement of 2500 nm and hardness mappings in the proximity of the GB with 200 nm indentation depth. Spherical indentations were performed with a conical diamond tip (Synton-MDP) with a specified tip radius of 5 µm to an indentation depth of 1250 nm. Hardness and Young's modulus were measured continuously as a function of indentation depth utilizing CSM using a frequency of 45 Hz and a harmonic displacement amplitude of 2 nm. Indentation data was evaluated according to the method proposed by

Oliver and Pharr [51] using a Poisson ratio of 0.31 [131] to calculate the Young's modulus. Hardness and modulus data were averaged between 2000 nm and 2400 nm to avoid a major influence of the indentation size effect for the reference indentations and from 175 nm to 190 nm for the mapping indentations. The thermal drift rate, measured at the end of each indentation experiment, did not exceed a maximum value of 0.16 nm/s. Pillar compression tests were done with a flat-punch diamond indenter tip (Synton-MDP) with the displacement speed set to 10 nm/s until a target displacement of 2000 nm was reached. The micro-sized bending beams were loaded by different indenter geometries with 10 nm/s displacement speed until fracture occurred or 3000 nm displacement was achieved.

For meso-scale bending experiments, samples with dimensions 12 x 4 x 1 mm^3 were cut with the long axis aligned in the normal direction from plate material since in this configuration grain separations are most likely. The specimens for sheet material were cut from the transverse direction due to the smaller thickness of this starting material, see Fig. 3.1. One surface was ground and polished in the same manner as mentioned above.

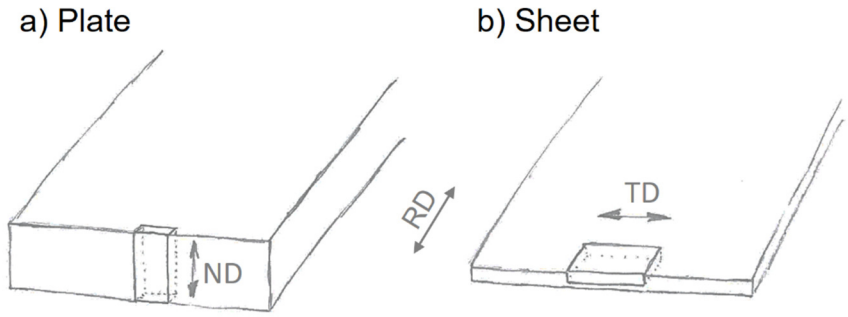

Fig. 3.1: Schematic drawing of the sample alignment for bending experiments from a) plate and b) sheet material. ND…normal direction, RD…rolling direction, TD…transverse direction.

In total 48 three-point-bending experiments were carried out between RT and -28 °C on a Kammrath and Weiß (K&W) GmbH (Dortmund, Germany) bending module, see Fig. 3.2. The sample was positioned in a way that the polished surface experiences tension during the displacement of the support bearings. The bearing distance was 9.2 mm and the diameter of the support rolls were 1 mm.

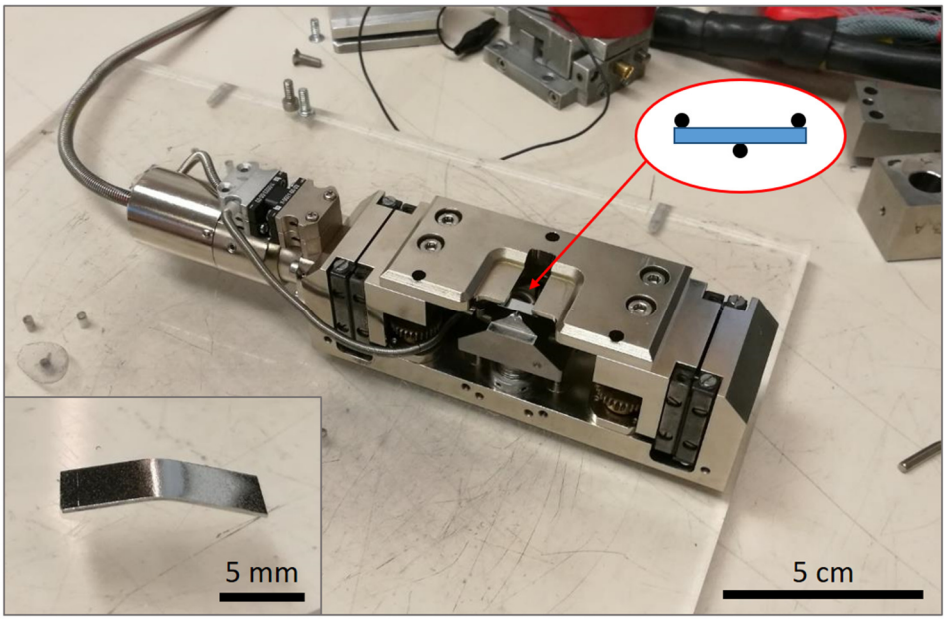

Fig. 3.2: K&W bending apparatus with a bending sample ready for experimentation. The inset shows a deformed sample.

The whole module was placed in a desiccator with connections for motor control, data acquisition and gas flow. A thermocouple was placed near the sample and the closed desiccator was positioned inside the cooling chamber. The experimental setup is illustrated in Fig. 3.3. Dry N_2 gas flow ensured that the bending module was not exposed to excessive humidity. The bending experiment was started with a deformation speed set to 5 µm/s as soon as the target temperature was reached. The samples were deformed until the specimen failed catastrophically or to a maximum displacement of 3000 µm, corresponding to a bending angle of about 90°. After bending, the apparatus was removed from the cooling chamber and warmed up to RT. The gas flow was used again to avoid humidity freezing on the bending module as well as on the sample.

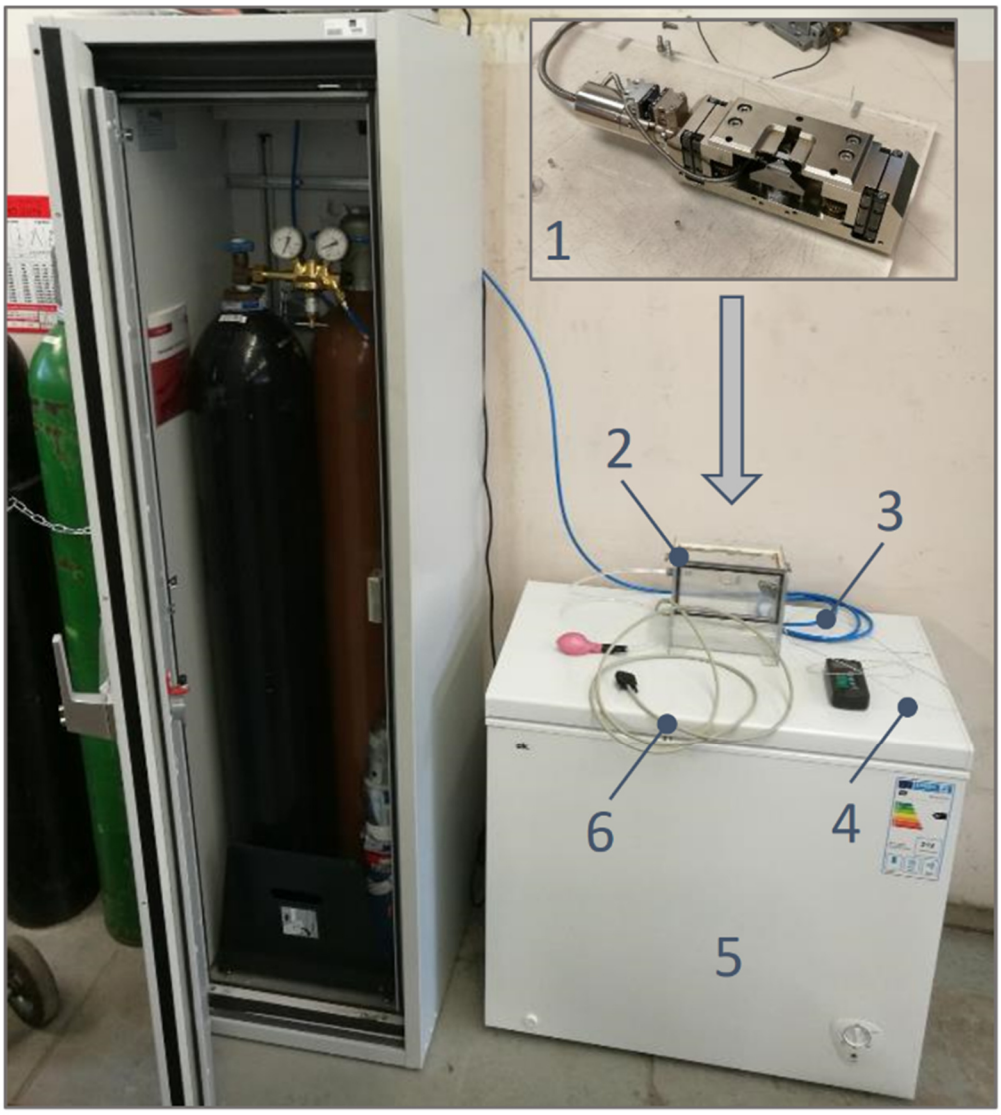

Fig. 3.3: The experimental setup for low-temperature meso-scale bending experiments. The K&W bending module (1) is placed in a desiccator (2), where N_2 gas flow (3) can be introduced. A thermocouple (4) is placed near the sample and the closed desiccator is positioned inside the cooling chamber (5). The motor control and data acquisition (6) as well as temperature measurement (4) is lead out of the cooling chamber and the bending experiment is started after reaching the target temperature.

SEM micrographs were captured on a Tescan CLARA field-emission SEM (TESCAN ORSAY HOLDINGS, a.s., Brno, Czech Republic) in backscattered electron (BSE) contrast mode with 50 nm/pixel resolution. The images were analyzed with the open source imaging software ImageJ [132]. The analysis of grain orientations was done with TSL OIM Analysis 8

and the slip system alignments were evaluated with a MATLAB script using the MTEX toolbox [133].

APT experiments were performed on a CAMECA LEAP 3000HR (CAMECA SAS, Gennevilliers Cedex, France; part of AMATEK Materials Analysis Division) in laser-pulse mode. The APT tips were prepared by a FIB lift-out technique as described in [134] and the used parameter were: laser energy of 0.6 nJ at 250 kHz, 60 K temperature and target evaporation of 0.5%. For the reconstruction, the software IVAS 3.6.14 was employed. The amount of segregations are calculated from concentration profiles perpendicular to the GBs as interfacial excess (IFE) values according to [135,136].

4. Chemistry of the recrystallization front

Extensive work was done previously on the segregation behavior of technically pure Mo by Katharina Leitner (neé Babinsky) [9,10,32,137]. Studies on deformed and recrystallized Mo material revealed higher total IFE values for the recrystallized samples as is depicted in Fig. 4.1. One question however remained, namely if the segregations are carried from the as-worked crystal to the newly forming GBs by the recrystallization front or not? To test this hypothesis, experimental work in the form of APT as well as considerations on diffusion mobility of impurities were undertaken. For the characterization of the recrystallization front, as-worked samples of Mo and MoB plate were annealed slightly below 1000°C for one hour to achieve equal amounts of recrystallized (RX) and stress-relieved (SR) parts in the microstructure.

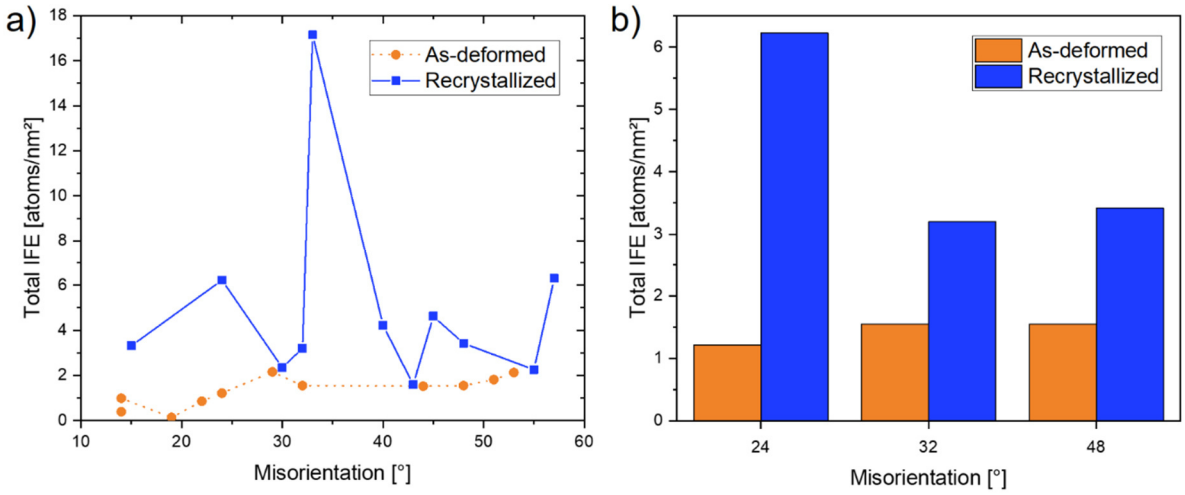

Fig. 4.1: Total amounts of O, N and P segregations at different GBs in deformed and recrystallized Mo samples. a) Total IFE values as a function of misorientation. b) Selected results for GBs with similar misorientation. Adaptation from [32].

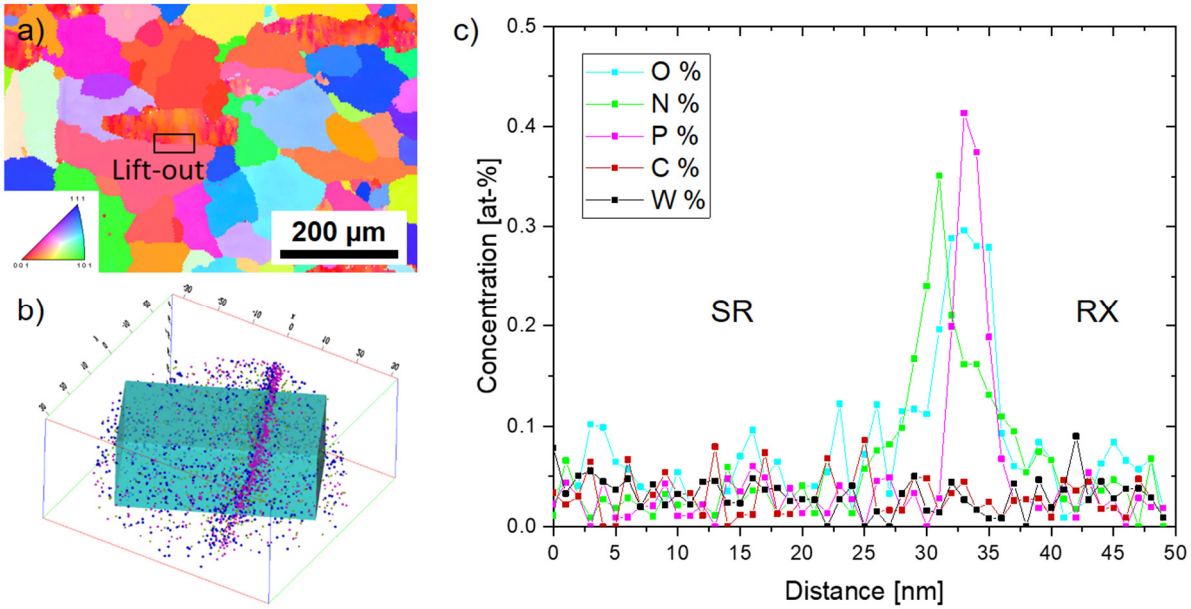

Fig. 4.2: a) EBSD scan of semi-recrystallized Mo material. The position for FIB lift-out for APT sample preparation is indicated. b) APT reconstruction of the recrystallization front showing concentration of impurities at the interface. c) Segregation concentrations along the region of interest depicted in (b).

Figure 4.2a shows an EBSD scan of the semi-recrystallized Mo sample with the position of the FIB lift-out indicated. In Fig. 4.2b the reconstruction of a successful measurement of the recrystallization front is depicted with O, N and P atoms. A prism with rectangular cross-section was selected as a region of interest and the measured concentration profiles are depicted in Fig. 4.2c. The impurities O, N and P are exceedingly located at the interface, as was already observed for recrystallized material. The concentrations within the grains near the recrystallization front are about 0.05 at-% on both sides. Beside the direct measurement of RX and SR grains within one atom probe tip, several tips without an interface from the same lift-out were measured. In total, 39.7 millions of atoms from at least three grains for each annealing state and material variant were analyzed. The average concentrations for the most common impurities O, N, P, C and W are given below in Fig. 4.3. The technically pure material seems to have more impurities than the doped variant, however, the concentrations are still under 0.04 at-%. Concerning the different annealing states, the impurity concentrations seem to be slightly higher for the SR grains in the pure Mo samples. For the doped material, this trend seems to lie in the opposite direction with slightly higher concentrations in the RX

annealing state. However, these slight differences are not significant when looking at the error bars in Fig. 4.3.

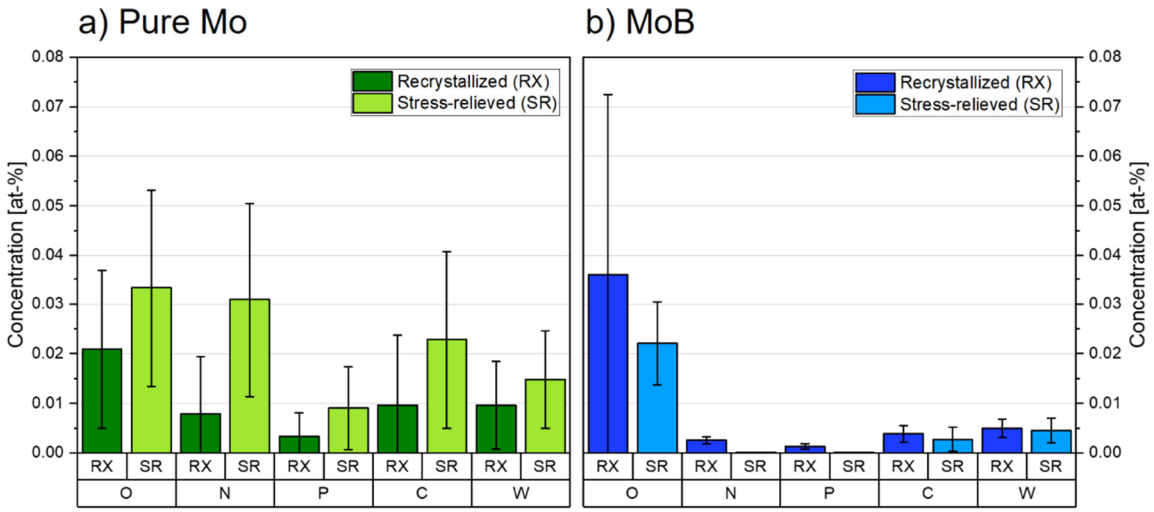

Fig. 4.3: Segregation concentrations of impurities in the RX and SR grains in semi-recrystallized a) pure Mo and b) MoB material.

Beside the APT experiments, the diffusivity of impurities was analyzed. If the impurity elements were faster than the recrystallization front, these atoms would hurry ahead or along with the interface. In the opposite case, the recrystallization front would flush the newly build grain from the impurity elements. The diffusion coefficients D of O, N, P, C and B were calculated between 25 and 1500 °C using the software Thermo-Calc [138], courtesy of Plansee SE. In literature, diffusion data for P in Mo is limited to one source at elevated temperatures [139]. The diffusion coefficient in this study was therefore extrapolated to lower temperatures according to formula 4.1, where D_0 is the diffusion pre-factor, Q the activation energy, R the universal gas constant and T the absolute temperature. Consequently, it represents only an estimation for the diffusivity of P. Table 3 depicts the diffusion coefficients at 1000 °C as well as the diffusion distances x (formula 4.2) for 1 hour annealing time (t) for the mentioned elements. In the last column, the mobility during heating and cooling with 1 K/s are included in the diffusion distance.

$$D = D_0 \cdot exp\left\{\frac{-Q}{R \cdot T}\right\} \qquad (4.1)$$

$$x = \sqrt{6 \cdot D \cdot t} \qquad (4.2)$$

Table 3: Diffusion coefficients and calculated diffusion distances with and without heating and cooling with 1 K/s for common impurities during annealing at 1000°C for 1 h of semi-recrystallized Mo materials. Note, that the data for P is estimated from a reference with diffusion data at higher temperatures, see text.

Element	$D\,(1000°C)$ [m²/s]	$x_{1000°C/1h}$ [µm]	$x_{1000°C/1h+1K/s}$ [µm]
O	$2.01 \cdot 10^{-11}$	660	1290
N	$1.45 \cdot 10^{-11}$	559	1310
C	$3.08 \cdot 10^{-13}$	81.6	162
B	$2.29 \cdot 10^{-9}$	7030	11600
P	$(2.83 \cdot 10^{-19})$	(0.078)	(0.209)

From the presented data, the heating and cooling makes up roughly half the possible diffusion distance of the impurities. Diffusion for O and N seem to be very similar. C has slightly less mobility, whereas B can diffuse up to a few mm. The estimation of the diffusivity of P shows less mobility, which is in agreement with the assumed position of P atoms in the lattice. Density functional theory calculations reveal that P is the only substitutional element for Mo in this list [30]. The diffusivity data of impurities suggest that impurities already move to the more favored positions at the GBs with the exception of P.

Figure 4.4 shows the analysis of a small-angle GB from as-worked material, courtesy of Katharina Leitner (neé Babinsky) [140]. The misorientation of 14° indicates that this boundary was formed during the rolling process and is not part of the initial microstructure after sintering. The absence of P segregation, but the presence of O and N at the interface could be explained by the mobility of these elements.

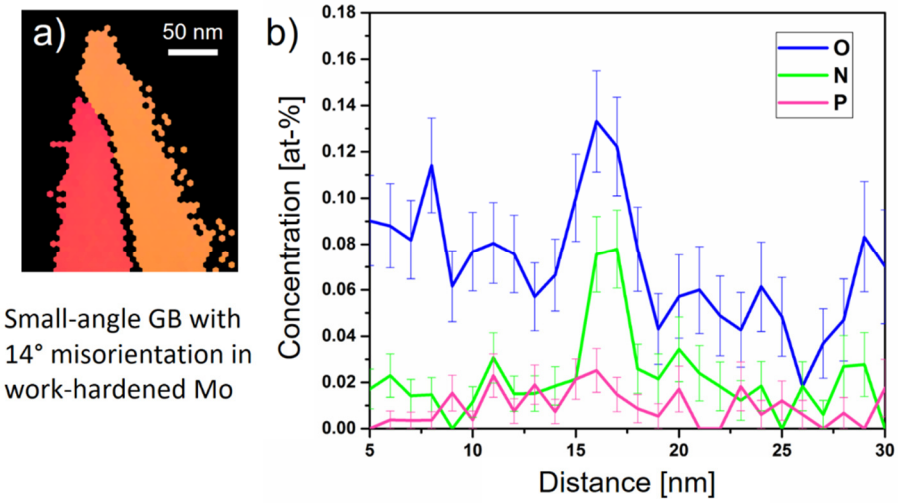

Fig. 4.4: a) Transmission Kikuchi diffraction micrograph of an APT tip including a small-angle GB from as-worked Mo material. b) Concentration profiles of O, N and P through the successfully measured interface. The higher concentrations of O and N indicate the presence of the boundary. [140]

To conclude this chapter, impurity concentrations within the grains in the SR and RX parts of a semi-recrystallized microstructure do not show significant differences. The impurity elements have enough mobility at the recrystallization temperature to diffuse to the favored positions at existing or newly formed GBs with one exception. P is a substitutional element in the Mo matrix and has therefore limited mobility. The absence of elevated P segregation content at a small-angle GB in work-hardened Mo indicates that P stays at the initial boundaries after sintering and may be dragged along by the recrystallization front during the formation of new grains.

5. Micromechanical response of grain boundaries

In this chapter, the results of micromechanical characterization techniques, namely nanoindentation, pillar compression and bending beams, employed near or at GBs are presented. The findings of each method are discussed and put into perspective regarding the applicability of these methods for the characterization of GB properties.

5.1. Nanoindentation testing

The results presented in the following sections have been partly published by the author in [128]. The numbering of figures as well as references was changed to fit the thesis.

For the indentation experiments, samples of a Mo plate were slightly deformed and recrystallized to achieve large grains. EBSD revealed an average grain size of 1267 ± 548 µm on the technically pure Mo sample, as shown in Fig. 5.1. This offered a canvas for indentation experiments on the same crystal as well as along GBs. Classical nanoindentation was performed with a Berkovich indenter tip. Furthermore, indentations were conducted with a spherical tip geometry.

Fig. 5.1: Stitched IPF map of the coarse-grained microstructure on a pure Mo sample.

5.1.1. Pyramidal Berkovich indentations near grain boundaries

The most used indenter geometry for classical nanoindentation is a Berkovich indenter (see Fig. 5.2). It is a three-sided pyramid with the same projected area as a Vickers indenter. To gain information of the properties of the grain interior as well as at the interface, reference indentations to an indentation depth of 2500 nm were carried out away from the boundary in grains with orientations near (001), (101) and (111). Additionally, arrays of indents with indentation depth to 200 nm were placed directly at the GB.

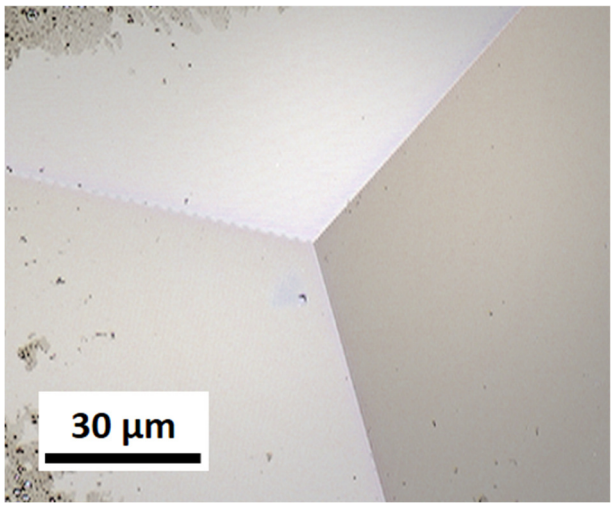

Fig. 5.2: Intensity micrograph of a Berkovich indenter taken with the LSCM.

Table 4 shows the averaged grain orientations expressed as Euler-Bunge angles (ϕ1, Φ, ϕ2), the misorientations of the GBs as well as averaged hardness and Young's modulus. Fig. 5.3b shows a section of an inverse pole figure (IPF) map of the region of interest containing the grains (101), (001) and (111), where the orientations are depicted as unit cells and in the IPF triangle. Adjoining to that in Fig. 5.3c, a scanning electron micrograph, using secondary electron mode, depicts the position of the reference indentation experiments as well as nanoindentation arrays (enlarged images illustrated as Fig. 5.3a and d). The distance between these indentations was set to 6 µm to exclude any interference of the plastic deformation of the individual indentations. The arrays were slightly inclined with respect to the GB to refine the available distance increments from the impression center to the GB.

Table 4: Orientations and micro-mechanical properties of the investigated Mo grains (illustrated in Fig. 5.3) as obtained by reference indentations.

Grain	ϕ1	Φ	ϕ2	Angle from zone axis	Misorientation of the GB		Hardness [GPa]	Young's modulus [GPa]
							(2000 - 2400 nm)	
(101)	82.6°	97.5°	299.4°	17.3°	44.5°		2.46 ± 0.01	321 ± 5
(001)	187.2°	105.7°	10.4°	18.7°		44.1°	2.41 ± 0.01	327 ± 2
(111)	56.4°	136.9°	312.5°	11.8°			2.43 ± 0.01	309 ± 3

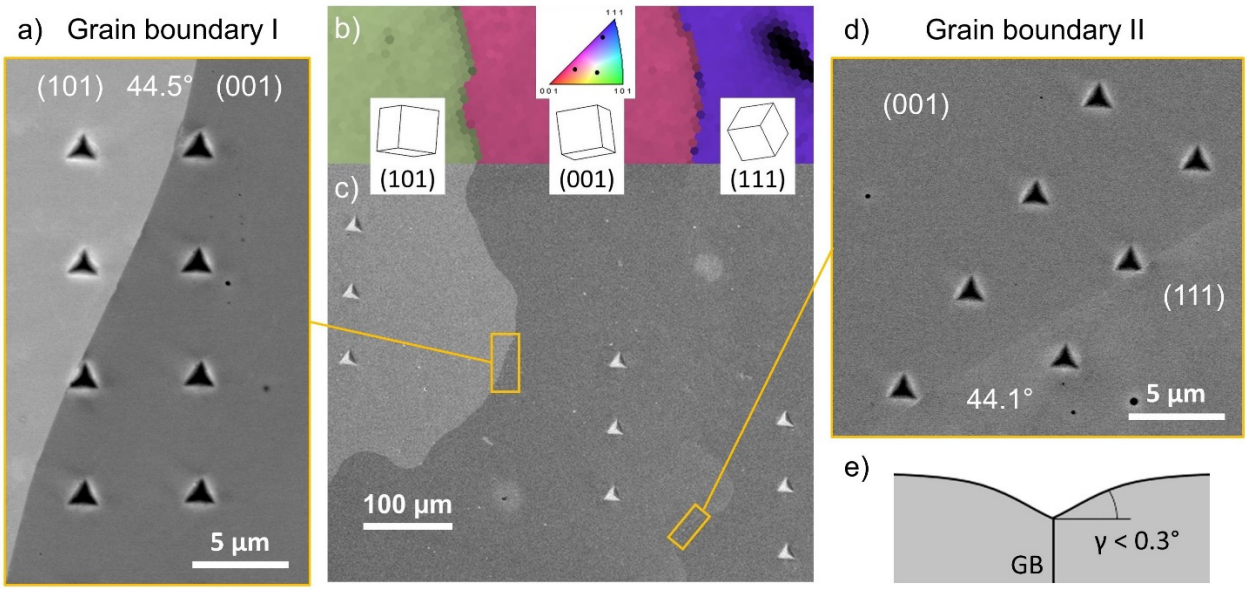

Fig. 5.3: b) Section of an IPF map near the region of interest with the orientations of the (001), (101) and (111) grains depicted as unit cells and in the IPF triangle; c) Scanning electron micrograph, taken in secondary electron mode, showing the positions of the reference indentations as well as the positions of arrays of mapping indentations (enlarged images (a) and (d)); e) shows a schematic of a GB groove in cross-section.

The topography of the electro-polished sample surface near the GBs was measured by the LSCM and shows an elevation of about 6 nm for the boundary (001)-(101). At the GB (001)-(111) a 30 nm high and 5 µm wide shoulder in the (001) grain is apparent, followed by a 5 nm groove directly at the interface. Any deviation from a horizontal sample surface in proximity of the analyzed GBs lies below an angular inclination of 0.3° (see Fig. 5.3e and Fig. 5.4).

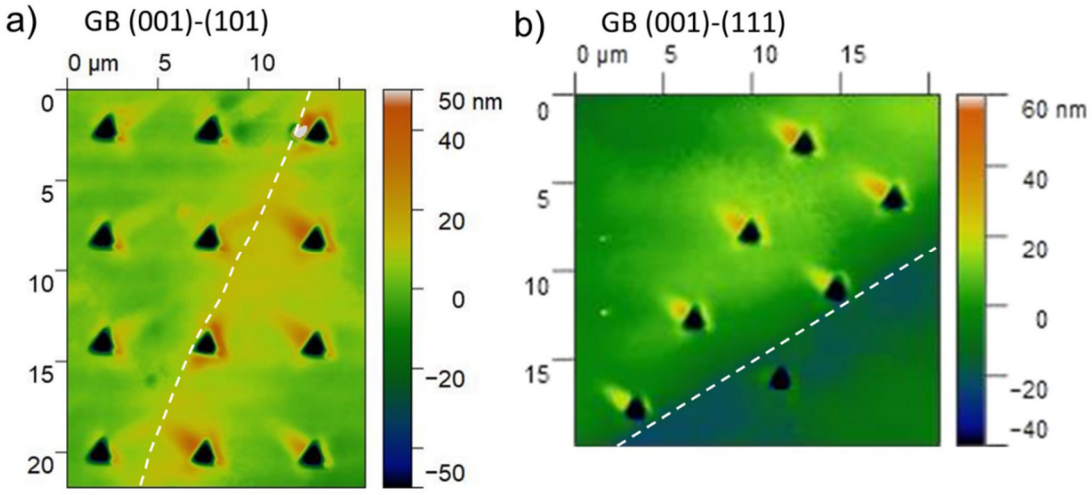

Fig. 5.4: LSCM height map of the topography of investigated GBs a) (001)-(101) and b) (001)-(111). The GBs are indicated by dashed lines.

As deformation by a three-sided pyramidal indenter tip is not homogeneously distributed underneath as well as around the impression in coarse grained metals, it is inevitable to analyze crystallographic favored deformation paths [141–145]. For instance, BSE detection can be used to reveal deformations just below the surface within one individual grain.

Figure 5.5 shows the residual impression of one of the reference indentations in the (001) grain in BSE contrast (Fig. 5.5a), the corresponding IPF map (Fig. 5.5b) as well as the orientation deviation map (Fig. 5.5c) overlaid with the EBSD image quality (IQ). The intensity of the backscattered electrons depends on the crystal orientation [146]. Similarly, the IQ of the diffraction patterns is influenced by the homogeneity of the crystal lattice. Dislocations introduced by the indentation process result in a deterioration of the IQ [147,148]. Notably, the contrast from the BSE image reflects the same features as the IQ as well as the orientation deviation map. The deviation of the grain orientation is a clear indication for the extensive

storage of dislocations in the vicinity of the indentation near the sample surface. Apparently, the most significant deformation pattern emerges at one face of the Berkovich tip, a fact that has to be considered in the further analysis.

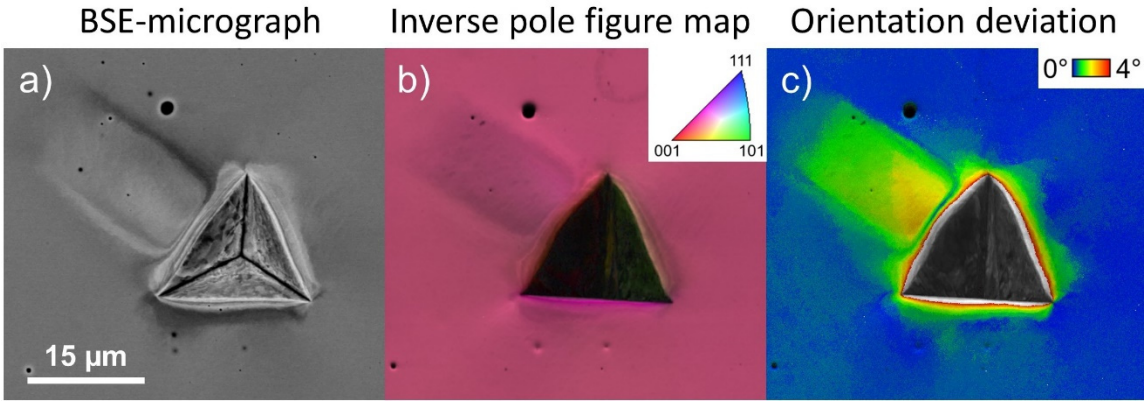

Fig. 5.5: a) SEM image, taken in BSE mode, of one residual impression of the reference indentations in the (001) grain (2500 nm indentation depth); b) IPF map and c) orientation deviation map overlaid with the IQ of the same indentation (see text).

Figure 5.6a and b show load-displacement curves of selected indentations in the (001) grain near the GBs. For metals with low dislocation densities, the first part of the experiment is governed by the elastic contact between the indenter tip and the sample surface. The appearance of initial pop-ins in our samples are also indicative for an efficient removal of the deformation layer during sample preparation via electro-polishing [75]. The modulus data show an increase for the first 25 nm of indentation, which among others could be attributed to the elastic contact between indenter tip and the sample [149]. For the elastic-plastic regime after the initial pop-in the modulus remains at a constant plateau with matching coincidence of the different indentations. Therefore, extensive influence of pile-ups or drift problems can be excluded as major error source (see Fig. 5.6c and d). After the initial pop-in, the hardness values show a decrease with increasing indentation depth (Fig. 5.6e and f). This behavior origins from the previously mentioned indentation size effect. The indentations with the largest distance to the GBs (d_{GB} = 2.9 µm and d_{GB} = 3.4 µm, respectively) are representative for the behavior of the grain interior and match the reference indentation values. Indentations closer to the GB exhibit a change in the hardness profile. For the GB (001)-(101), at a distance to the GB of 1.2 µm, the averaged hardness between 175 nm and 190 nm increases to

3.76 ± 0.01 GPa, when compared to 3.45 ± 0.01 GPa occurring in the grain interior. Hardness further increases for the closest indentation at d_{GB} = 0.6 µm with H = 4.06 ± 0.01 GPa, which is an increase of 18%. In contrast, the indentations at the GB (001)-(111) do not show any significant hardening for the closest indentations (d_{GB} = 0.6 µm). The insets in Fig. 5.6e and f illustrate the respective GBs with the orientation of the different grains depicted by the unit cells. A schematic representation of the deformation pattern around an impression in the (001) grain is shown near the GBs.

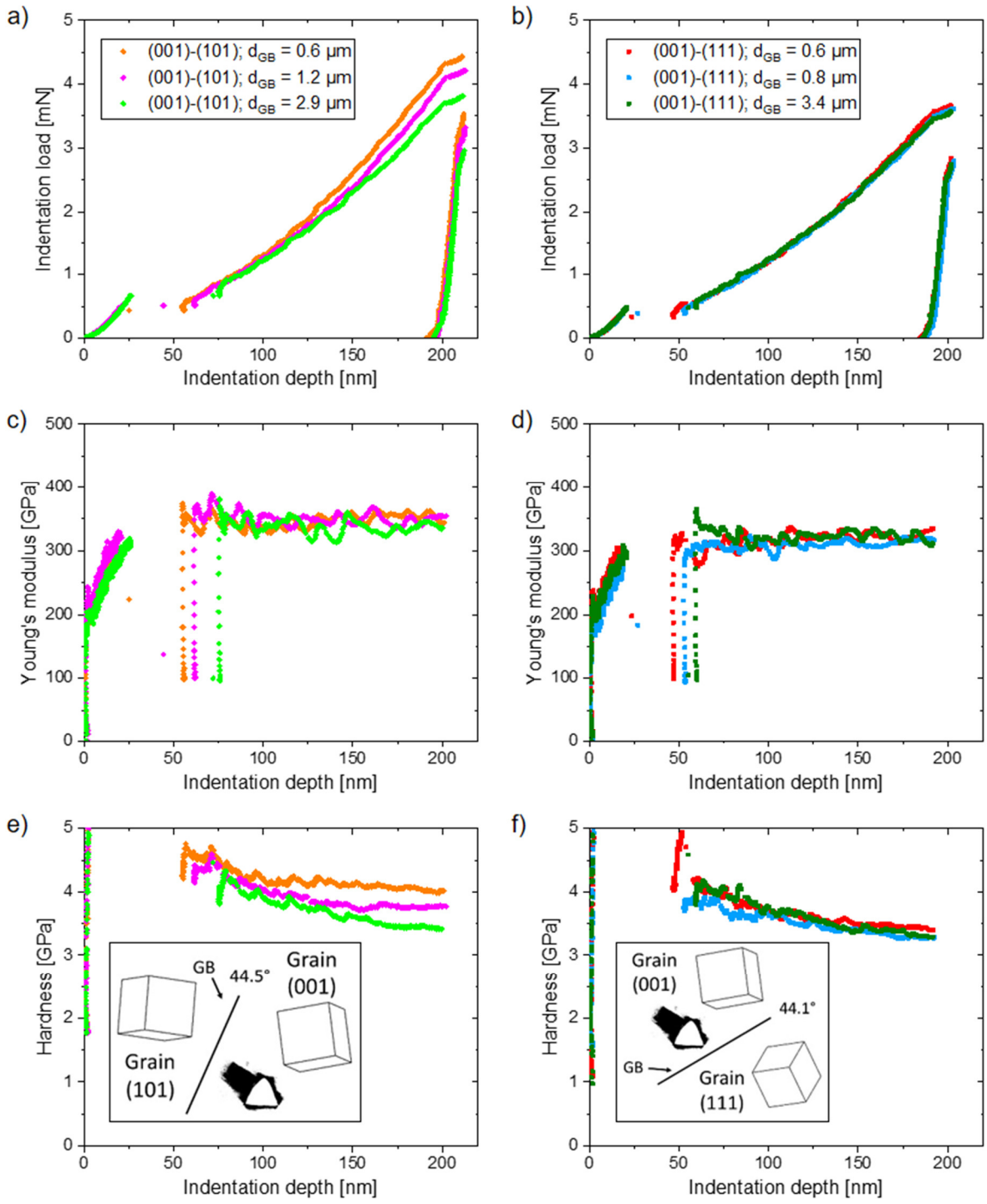

Fig. 5.6: Indentation load, Young's modulus and hardness vs. indentation depth for selected representative indentations in the vicinity of GBs (001)-(101) (a, c, e) and (001)-(111) (b, d, f). The insets in (e) and (f) show a schematic representation of the GB and the deformation induced by the indentations.

The hardness data of the indentation arrays at these two GBs was averaged between 175 and 190 nm indentation depth and is depicted as a function of distance to the interface in Fig. 5.7. The indented grains are labelled respectively and the increased hardness in vicinity of the GBs is indicated by the shaded regions. Both GBs show increased hardness towards the interface. However, the distance at which elevated hardness is measured is different. Approaching GB I from within the middle grain (001), increasing hardness can be detected already at about 3 µm distance towards the boundary. Looking at GB II, the hardness increase in the same grain starts not below 1 µm distance from the interface.

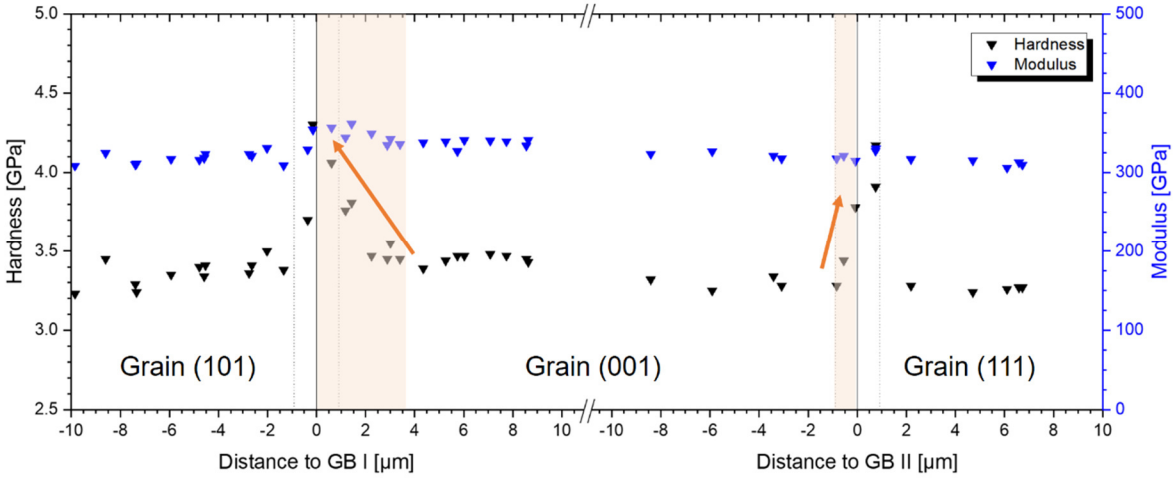

Fig. 5.7: Hardness and modulus as a function of distance to the GB for the two investigated interfaces.

5.1.2. Influence of pyramidal indenter rotation

For geometrical considerations, a relationship between the deformation pattern in the bcc Mo structure and the rotation angle around the loading axis of the three-sided pyramid with a symmetry of 120° is obvious. To assess the impact of this effect, the sample was rotated in steps of 10° until an angle of 110° was reached with respect to the origin position. At each increment, four indentations to a preset depth of 2500 nm were conducted within the same grain (referred to as Grain A), having Euler-Bunge orientation angles of $\phi1 = 67.9°$, $\Phi = 80.9°$ and $\phi2 = 146.7°$. The indentations show consistent hardness values of 2.38 ± 0.02 GPa and a Young's modulus of 306 ± 9 GPa. Apparently, the indenter orientation does not influence the

intrinsic response of the material in absence of a GB. Fig. 5.8a shows the EBSD scan of the investigated grain and its grain orientation (unit cell in Fig. 5.8b) as well as a LOM micrograph of the arrays of imprints with different rotational increment (Fig. 5.8c). Since the sample had to be rotated, a dial was drawn on the sample holder as can be seen in Fig. 5.8d.

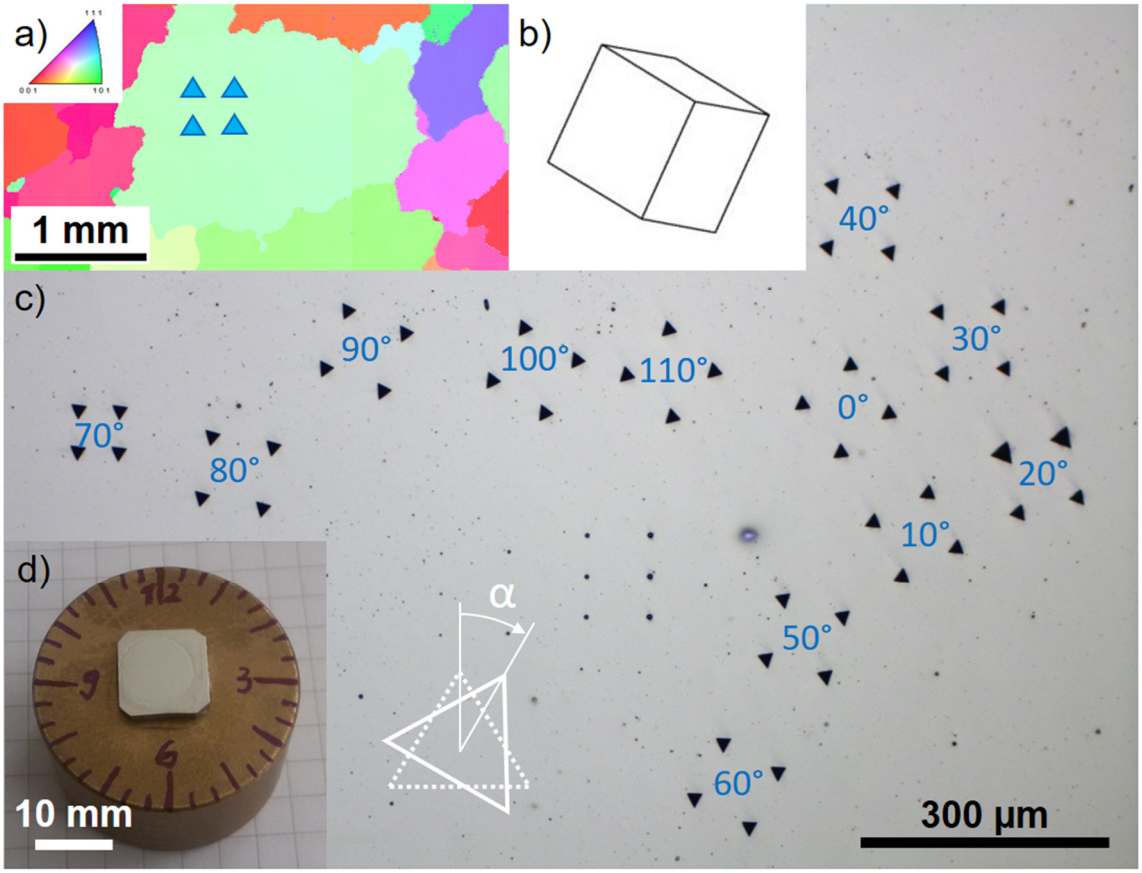

Fig. 5.8: a) IPF map of Grain A with the unit cell depicted in (b). c) Light optical micrograph of the impressions with different indenter rotation. d) Sample holder with the drawn dial for the respective rotation.

Figure 5.9 displays one of the imprints for each rotational increment in differential interference contrast (DIC) of the LOM. In this manner, especially the material pile-up around the indentations is visible. The dominant pile-up occurs towards the upper left corner of the images. It is most visible for rotational increments between 10° and 70° (Fig. 5.9b to h). In the other cases, a pile-up in this direction is visible, however, not as dominant. On the other sides of the imprint, material pile-up is not as pronounced.

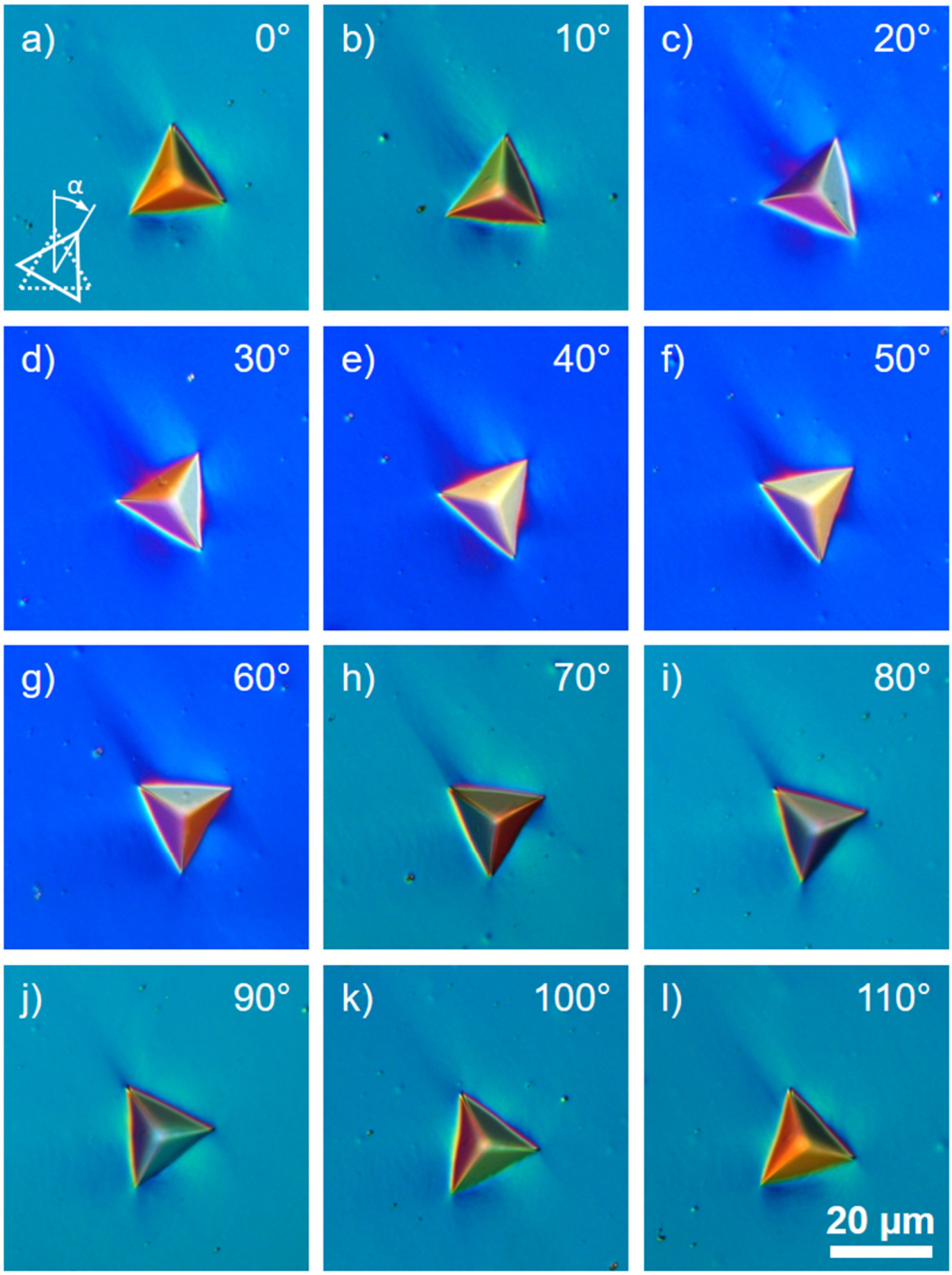

Fig. 5.9: LOM micrographs in DIC of the imprints with different rotational increments.

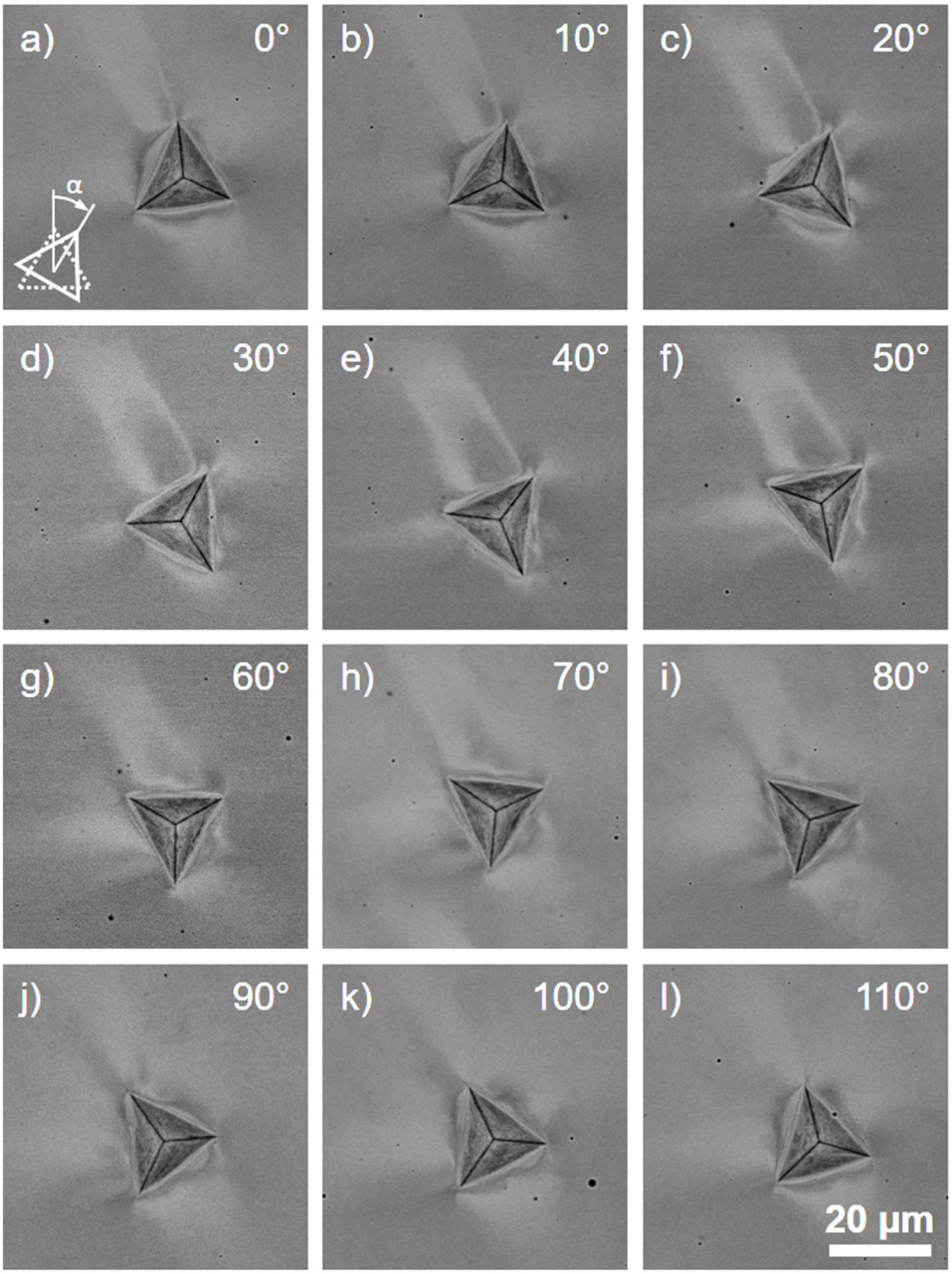

Fig. 5.10: Micrographs in BSE contrast of the imprints with different rotation angle.

Figure 5.10 shows imprints of all rotational increments in BSE contrast. Using electrons for illustration, the material pile-up is not visible, especially with BSE. However, since this imaging technique is sensitive to the crystal orientation, small rotations of the crystal are apparent in the form of lighter or darker contrast. The reason for this is the different channeling contrast. Electrons penetrate deeper into the surface if the crystal planes are aligned towards the surface or the crystal has a low dislocation density. In this case, we see the deformation introduced by the indenter tip as a contrast change compared to the rest of

the grain. Dislocations are generated to accommodate the necessary plastic deformation and the resulting crystal rotation and imperfections lead to the lighter or darker contrast in the SEM. For this particular grain, the deformation is most apparent to the upper left corner of the images for indenter rotations between 0° and 70° (Fig. 5.10a to h), as was the case for the material pile-up visible in LOM. Further minor deformation is visible on the bottom-side of the imprint. Starting at 50° rotational increment, another deformation direction becomes visible at the left-hand side of the images. It is most apparent at 90° and 100° rotational increment (Fig. 5.10j and k). Furthermore, deformation towards the lower right corner of the images can be seen for increments of 80° and more.

It seems that the directions of deformation is consistent for all rotational increments and consequently an effect of the grain orientation. The extent of deformation for a particular direction however, is different depending on the rotational increment. To further study this phenomenon, EBSD measurements of selected imprints were taken and the grain reference orientation deviation (GROD) is displayed in Fig. 5.11. Rotational increments of 30°, 60° and 90° were selected since the deformation pattern evolve from mostly towards the upper left corner in the case of 30° to deformation at the left-hand side with mostly similar extent all around for 90° rotational increment (Fig. 5.11a to c). Furthermore, spherical indentations were performed on the same grain. In contrast to the Berkovich geometry, a spherical tip represents an axially symmetric body of rotation (Fig. 5.12). Therefore, the introduced deformation pattern corresponds to the intrinsic deformation paths of the crystal structure for a certain imprinting direction of the indented grain. Hence, the rotation angle α of the indenter as one additional influencing parameter during investigations of a GB can be disregarded.

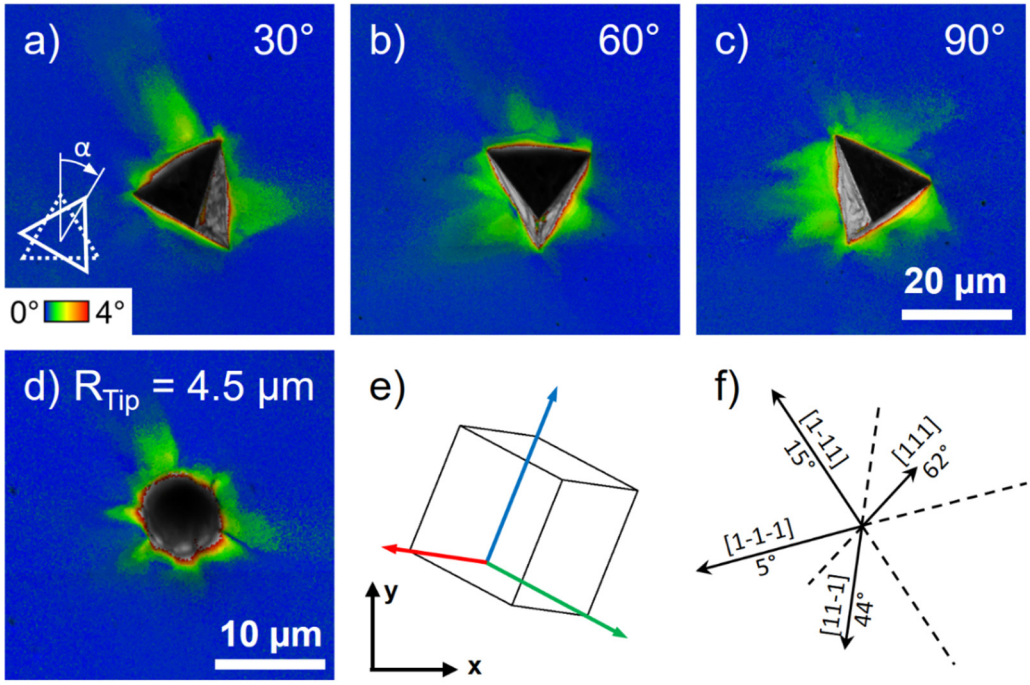

Fig. 5.11: a) through d) GROD maps of selected imprints. Note the different scale bar for spherical indentation. e) Unit cell of the indented grain. f) <111> directions of the grain. The angle between direction and sample surface is indicated next to the direction.

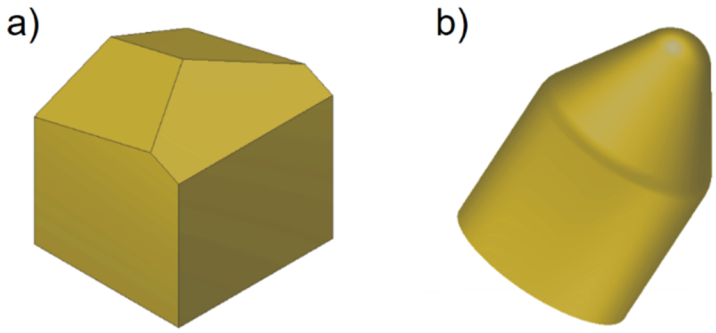

Fig. 5.12: 3-dimensional renderings of a) a Berkovich tip and b) a cone-shaped indenter with a spherical apex.

The specified radius of the spherical apex of the conical indenter was 5 µm. After calibration the apex radius was determined to be 4.5 µm. The GROD measurement of this imprint to an indentation depth of 1250 nm is displayed in Fig. 5.11d. For crystallographic reasons, the directions of deformation are similar to pyramidal indentations, but the proportions are more equally distributed. In Fig. 5.11e and f, the unit cell of the indented grain

as well as the <111> directions of the crystal orientation are shown. Next to every direction, the angle of the crystal orientation out of the sample surface is written. The imprint with 30° rotation shows extensive deformation in the [1-11] direction of the grain. The deformation pattern in this direction is gradually decreasing with increasing rotation between indenter and sample. At 90° rotational increment, deformation in [1-11] direction is almost not present near the surface. In contrast to that, increased misorientation of the original grain orientation is apparent at the left-hand side of the imprint. This indicates deformation along the [1-1-1] direction of the crystal and is most pronounced for 90° and not visible at 30° rotational increment. The deformation pattern of the spherical imprint is similar to the deformation of the 30° imprint, suggesting that [1-11] is the most favored deformation direction for this particular grain.

In order to investigate the influence of the rotation of the Berkovich indenter in the proximity of a GB, two arrays of indentations with 200 nm indentation depth were placed across a GB (Grain B orientation $\phi1 = 156.7°$, $\Phi = 98.9°$ and $\phi2 = 167.9°$) with a misorientation angle of 24.5°. In one case, $\alpha = 30°$ was selected as most of the deformation is introduced on the side of the tip facing the GB. In the other case, a 90° rotation angle was selected, where the vertex of the Berkovich tip is pointed towards the boundary. Fig. 5.13 shows Young's modulus and hardness of selected indentations of the two arrays. The modulus values coincide, since the indentations are placed within the same grain. The hardness data show an increase of 8% for the indentation in 1.3 µm distance to the boundary with 30° rotation. In contrast to that, even the closest indentation with 90° rotation, positioned at 0.7 µm distance to the interface, shows no influence of hardness. The inset further illustrates the schematic deformation patterns of the impressions regarding the GB.

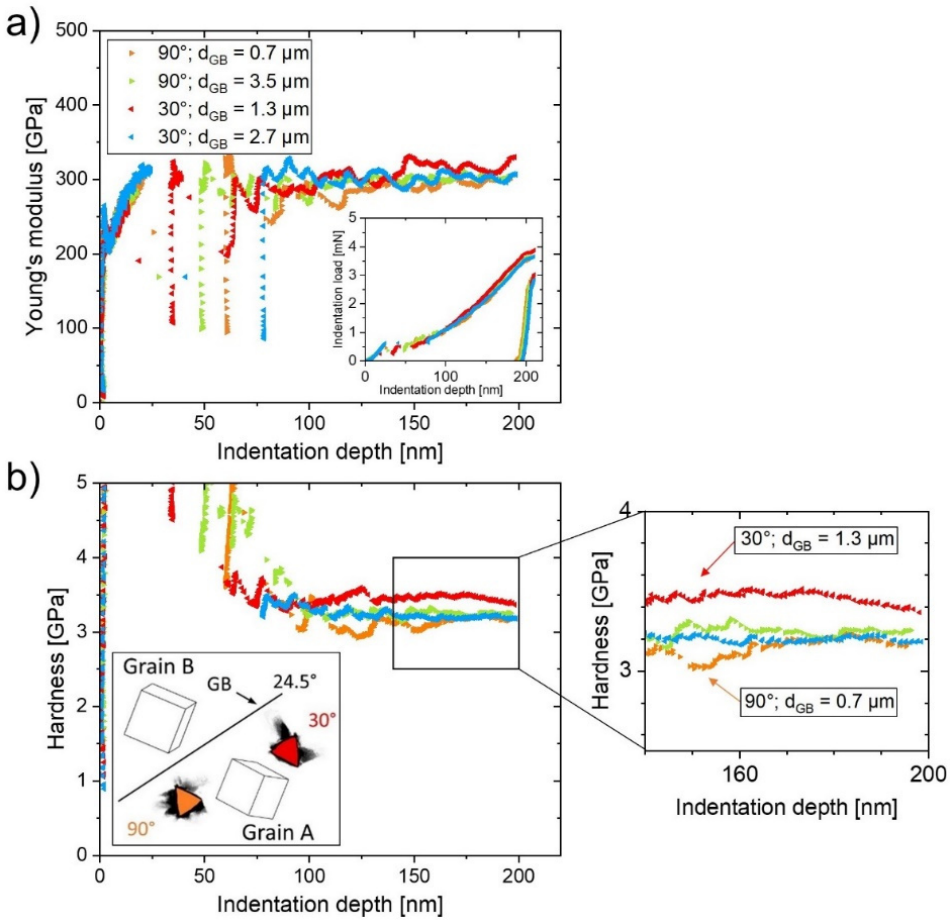

Fig. 5.13: a) Young's modulus with indentation load vs. indentation depth as inset and b) hardness measurements of selected indentations with 30° and 90° rotation of the Berkovich tip in proximity of the same GB.

An SEM micrograph of the alignment of the different arrays is depicted in Fig. 5.14a in BSE contrast. To exclude any influence of surface roughness, LCSM images of the topography were taken and are illustrated in Fig. 5.14b. The surface in Grain A is slightly raising, however, this will not influence the measured data in any significant way. At the interface, a small shoulder to the adjacent grain is visible in the surface profiles (arrows in Fig. 5.14d). From profile 1, the pile-up on the side of the imprint facing the boundary is visible by the different height on opposite sides of the imprint. Fig. 5.14c shows the cross-section at the GB fabricated via FIB-milling. The inclination of the interface within the sample amounts to 21° from a vertical plane. This means that the interface is well in the way of any deformation coming from Grain A.

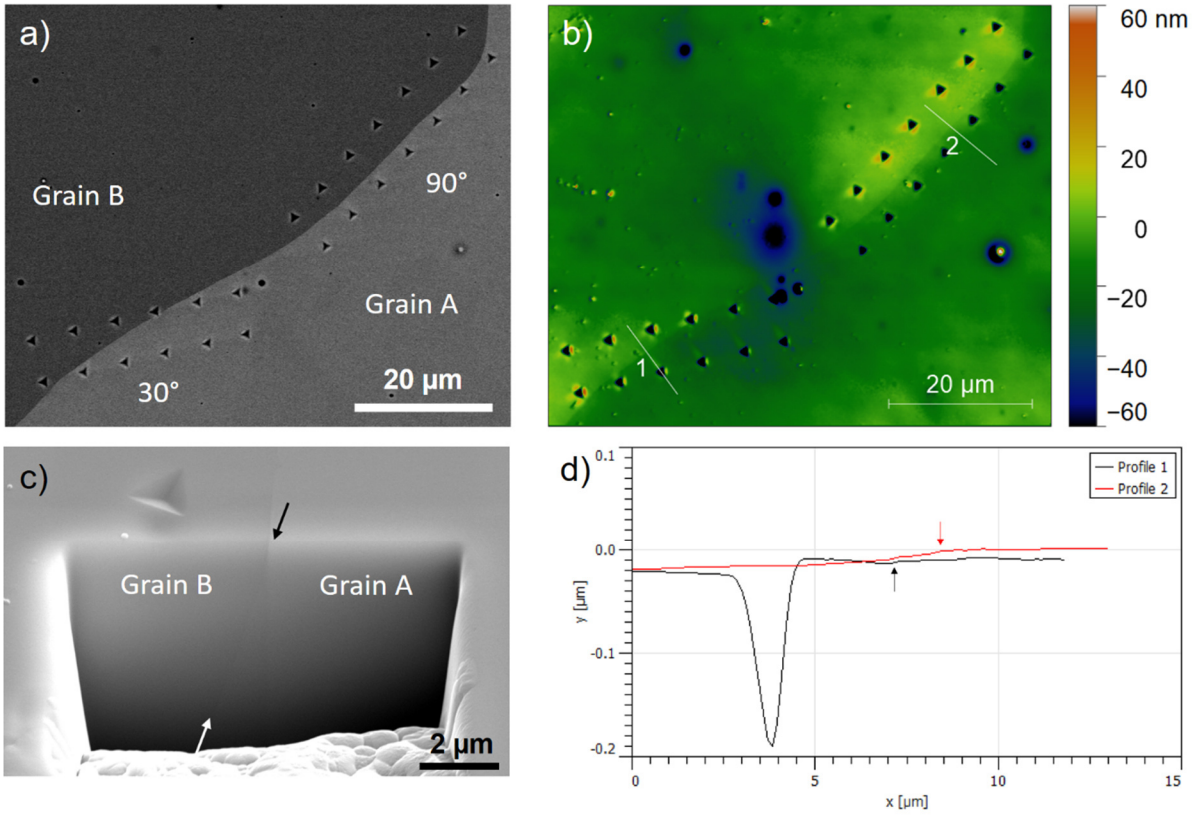

Fig. 5.14: a) SEM micrograph of indentation arrays with different rotational increments. b) Topography of the same area. c) FIB cross-section revealing 21° inclination of the boundary. d) Surface profiles corresponding to (b), the position of the boundary is indicated by arrows.

5.1.3. Investigations into the deformation paths of indentations

It was demonstrated in the previous section, that the deformation at the indents is not conform around the indent. Specific directions of pronounced deformation are apparent in light optical and electron micrographs as well as crystallographic analysis by EBSD (Fig. 5.5, Fig. 5.9 to Fig. 5.11). The indentation introduces a complex stress and strain field under the indenter tip and the crystal yields predominately in crystallographically favored directions. With the mentioned imaging techniques, only deformation near the surface can be visualized. For the analysis of the deformation within the material, destructive FIB milling to perform cross-sections would be necessary.

To get a better picture of the material response in terms of deformation patterns, several spherical indentations were performed on grains with different crystal orientation. Spherical indentation excludes a possible influence of indenter rotation since the geometry is

indifferent around the loading axis. Fig. 5.15 depicts the hardness response as a function of strain as well as DIC images of eight imprints, covering a variety of possible orientations. The modulus data shows constant values of slightly over 300 GPa, indicating proper experimental data. The hardness for the different indented crystals show one plateau for the grain near (001) orientation and two different hardness plateaus for every other orientation with varying amplitude. The highest difference between the hardness plateaus can be found for the grain near (101) orientation. These differences in hardness might stem from the activation of different slip systems with increasing indentation depth. For every indented crystal orientation, one exemplary imprint is depicted in DIC of the LOM. In this way the material pile-up, which corresponds with the deformation near the surface, can be imaged. The imprint in the grain near (123) orientation shows one distinct deformation direction and several pile-ups closer to the imprint. Every other imprint displays at least two distinct directions of extensive material pile-up, see for example the indentations close to (112), (113) and (103). The imprint in the grain with 7.7° to the (001) orientation shows almost perfect four-fold symmetry, only the extension of deformation varies.

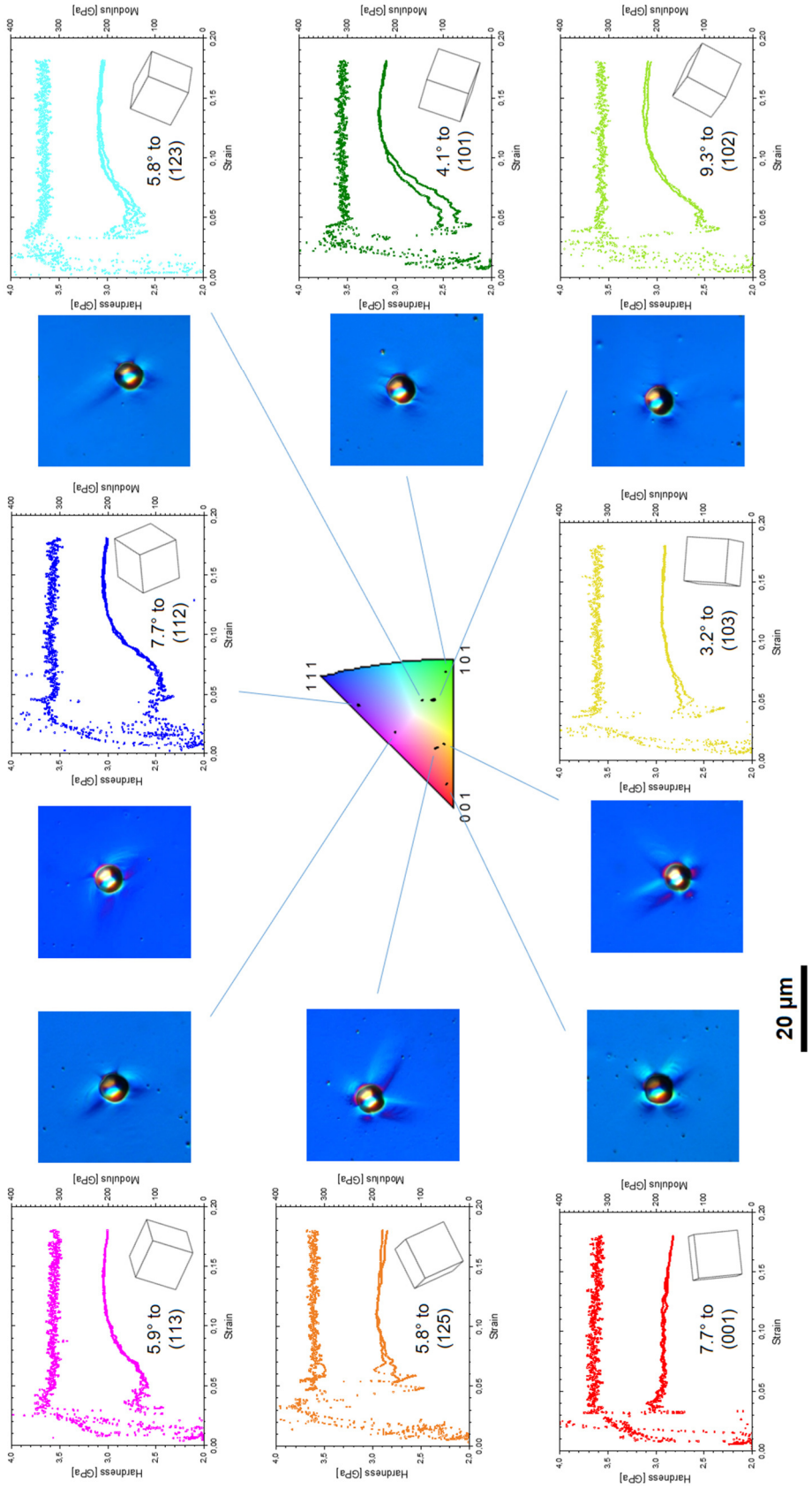

Fig. 5.15: Analysis of deformation paths and hardness response of spherical indentations into different grain orientations (details see text).

After consideration of the material pile-up at the indentations for the different orientations, it becomes clear, that the directions of deformation correspond to the <111> directions of the indented crystals. The imprint in the grain near (101) shows material pile-up in all <111> directions, since the four directions point in a similar angle out of the surface. Further study of the angle between sample surface and crystal direction reveals the deformation directions which show pronounced deformation. If the angle between <111> direction and sample surface is small, the material pile-up extends far from the imprint (e.g. imprint in grain near (125)).

5.1.4. Calculation of the shear stress at initial pop-ins

The initial pop-in at the start of an indentation experiment represents the transition from purely elastic deformation to fully elastic-plastic deformation. It is marked by a sudden dislocation burst for load-controlled nanoindentation devices [51,150]. Fig. 5.16 depicts the initial material response of sample areas with high and low dislocation density. If the material underneath the indenter tip is for instance in the as-deformed state, moveable dislocations are present from the start of the experiment and the load-displacement response is as depicted for Indent 1. If there is no dislocation source present underneath the indenter tip, the crystal is deformed elastically until a first dislocation is generated. After this dislocation runs to the surface, an avalanche of following dislocations are generated resulting in a dislocation burst visible for Indent 2. The initial elastic response of the material can be described by Hertz' contact mechanics (for details see [151]). Even the apex of pyramidal tips are worn down to a spherical shape and the radius R can be determined by fitting formula 5.1 to the experimental data (load P and displacement h) with E_r as the reduced modulus. Using this radius and the load at the dislocation burst P_{Pop-in}, the necessary shear stress τ to activate a dislocation source or generate a new dislocation in the crystal can be calculated according to formula 5.2. In the case of a homogeneous nucleation of dislocations, the maximum stress underneath the indenter tip corresponds to the theoretical shear strength of the material [73,152].

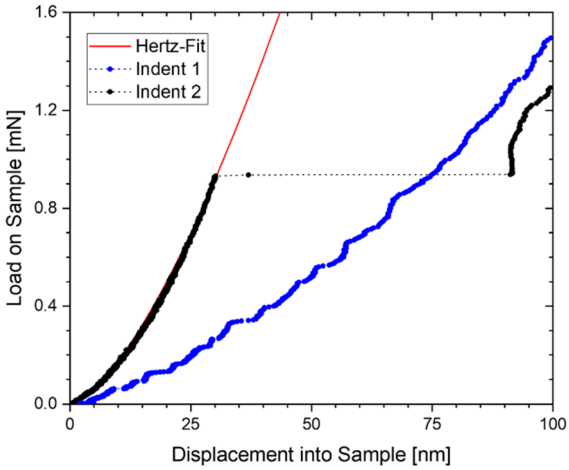

Fig. 5.16: Initial load-displacement data for materials with low (Indent 1) and high dislocation density (Indent 2).

$$P = \frac{4}{3} E_r \cdot \sqrt{R} \cdot h^{3/2} \qquad (5.1)$$

$$\tau = \frac{0.31}{\pi} \left(\frac{6 \cdot P_{Pop-in} \cdot {E_r}^2}{R^2} \right)^{1/3} \qquad (5.2)$$

The loads at which the first dislocation burst sets in were analyzed for four indentation arrays performed with the same Berkovich tip. The indentation experiments on Mo and MoB samples showed initial pop-ins at loads between 0.1 mN and 0.8 mN. The indenter tip radius was determined on a tungsten reference sample to be 200 nm (formula 5.1). Using the reduced modulus from the indentation data as well as the pop-in loads, the corresponding shear stresses were calculated and are shown in Fig. 5.17. The maximum shear stresses for the different grains are between 17.4 GPa and 19.9 GPa, fitting well with the theoretical shear strength of Mo [153–155].

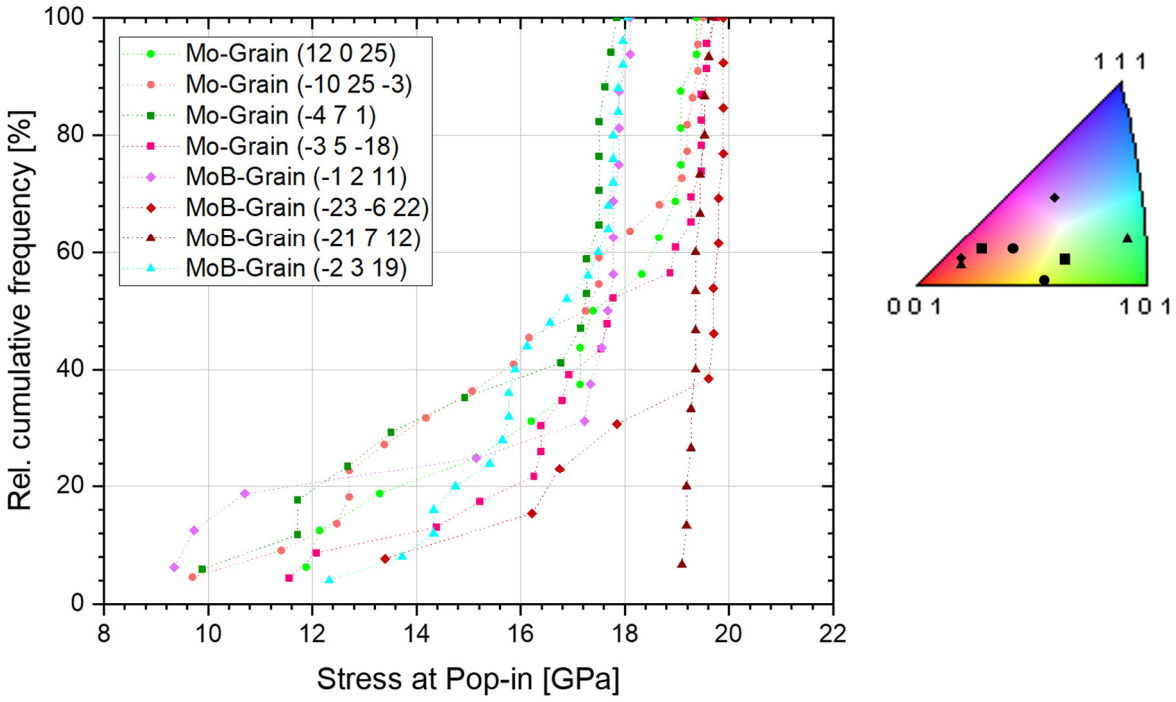

Fig. 5.17: Shear stresses at initial pop-in loads for four different indentation arrays with a Berkovich tip.

One instance demonstrates the drastic impact of ion implantation on the surface. A particular GB was not visible in the LOM due to the absence of a groove or other contrast at the interface. The FIB was used to mill markers next to the GB. Fig. 5.18 shows an EBSD scan of the mentioned sample area and an electron micrograph of the boundary with the FIB markers. In this way, the indentations could be placed in the vicinity of the interface. After exposure to the ion beam, no initial pop-ins were detected. Furthermore, the resulting hardness measurement of the mutual grain did not match previous indentation tests on the opposite side of the grain as depicted in Fig. 5.18c. The average hardness value was elevated by 0.5 GPa for the ion beam exposed GB compared to the initial measurement. Despite the increase in hardness, the modulus remained at the same level, as is also reported in literature for ion-irradiated material [85].

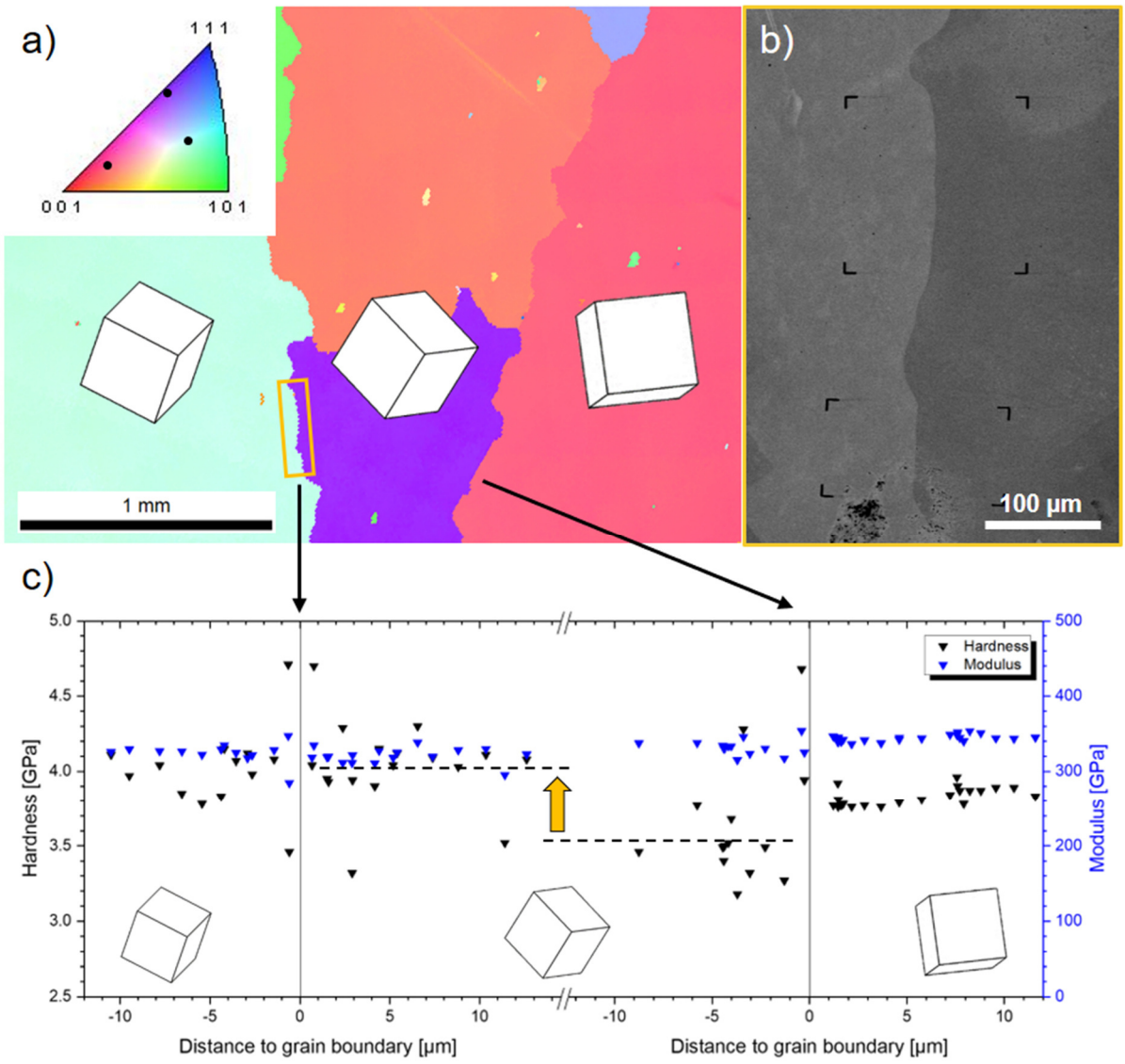

Fig. 5.18: a) IPF map of the area where the FIB was used to mill markers next to a GB, indicated by the yellow rectangle. b) SEM micrograph of the boundary with FIB markers. c) Hardness and modulus as a function of distance to the GBs showing increased hardness for the ion beam exposed boundary.

5.1.5. Extraction of characteristic values from hardness profiles

Beside Berkovich indentations, cones with a spherical apex were used for spherical indentation. In contrast to a pyramidal indenter, spherical indentation introduces a non-self-similar stress state in the material underneath the indenter tip. Fig. 5.19 shows the geometry of the spherical indenter at different displacements. It follows from the different current opening angles that the material experiences different strains dependent on the indentation

depth. The measured hardness H can be converted to representative indentation stresses σ_r with the constraint factor C^* according to formula 5.3. It has been shown, that this value is not constant, but dependent on the ratio of Young's modulus to yield strength and the opening angle during indentation [156,157]. A. Leitner et al. [57] applied a refined definition for C^* for the different deformation regimes as well as a new calibration method for the tip radius. In this way, the generated indentation stress-strain data matched micromechanical tests on pillars made out of ultrafine-grained metals. For details, see their publication.

$$\sigma_r = \frac{H}{C^*} \tag{5.3}$$

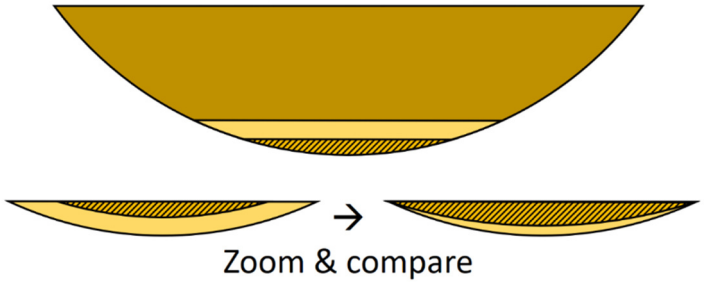

Fig. 5.19: Schematic drawing of the spherical indenter geometry in cross-section. The different shaded areas represent indentations to different depths. If the geometries are scaled to the same size at the sample surface plane, the overlaid shapes do not match. This shows the non-self-similarity of spherical indenters.

Figure 5.20 shows the stress-strain data generated with the mentioned protocols [57] from spherical indentations to 1500 nm indentation depth near a GB. One grain near (001) orientation shows one stress plateau, whereas two plateaus are present for the other grain. The reason for different stress plateaus might lie in the activation of different slip systems. The transition between these two flow curves seems to be immediate after crossing the GB and the indentation right at the interface displays additionally elevated stress. Beside these indentations, smaller imprints were performed directly at the interface similar to the Berkovich indentation arrays. The hardness value at 6 % strain from over 70 measurements is displayed in Fig. 5.21 as a function of distance to the interface. Beside the different hardness levels in the grains, a distinct peak hardness at the interface is apparent.

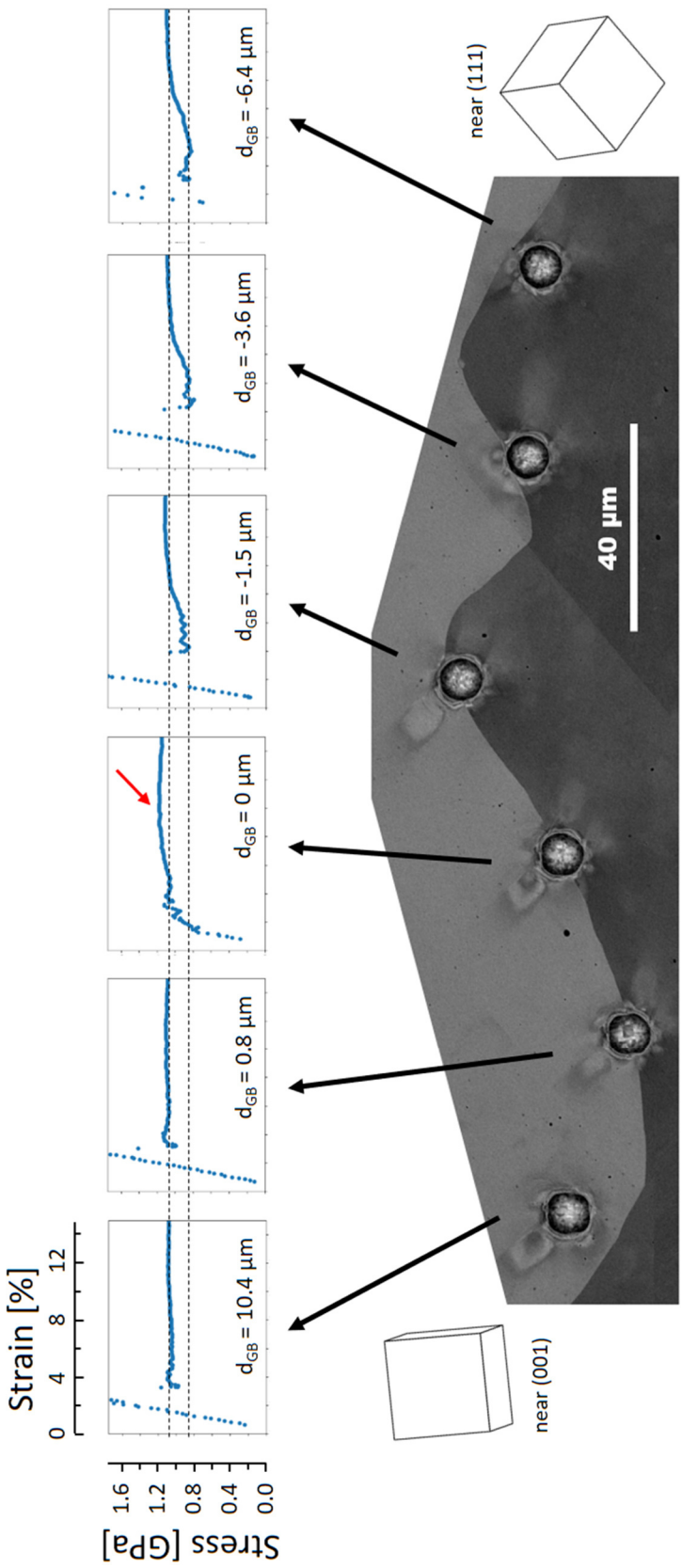

Fig. 5.20: Spherical indentations to 1500nm indentation depth near a GB. The stress-strain data shows elevated hardness for the imprint directly at the interface (red arrow).

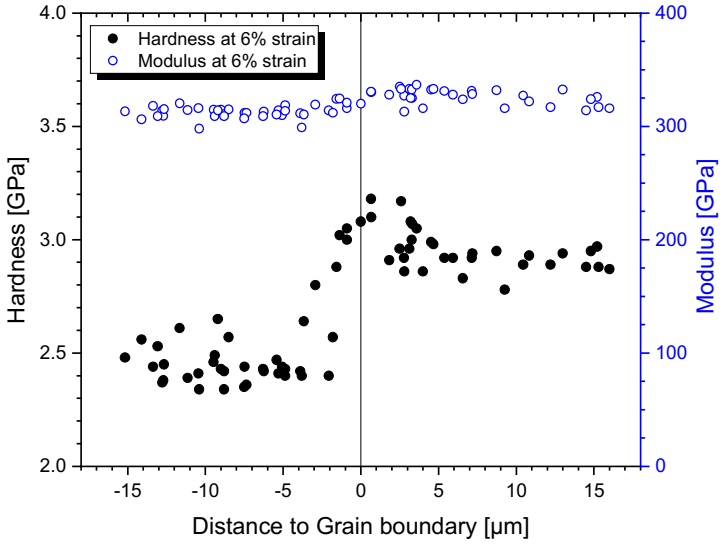

Fig. 5.21: Hardness and modulus as a function of distance to the GB for spherical indentations on a MoB sample.

The comparison of the hardness increase at GBs is not immediately possible. The hardness plateau is generally different in each grain, an increase of hardness values starts at different approximation towards the boundary and the peak hardness is predominately at a position where the hardness response stems from both grains. To compare the response of individual GBs, a methodology to deduce reproducible parameters has to be assessed. From first consideration, at least two parameters are necessary, namely the altitude of hardness increase and the distance at which the increase starts. A possible fitting of the hardness profiles has to fulfill the following criteria:

- Constant hardness value far from the interface;
- Increase towards the boundary;
- Decreasing gradient towards a maximum value; This value is expected at a distance of 0 µm.
- Same criteria for the other grain with different parameters;

The data processing software ORIGIN offers different fitting tools. One possible group of fit functions fulfilling the mentioned criteria is an asymmetric peak-function. However, the bi-Gaussian fit did not converge for most hardness profiles. To circumvent this shortfall, the

data of hardness profiles were split and every grain was mirrored at 0 µm distance to the interface. Now one can use the symmetric Gauss-fit according to formula 5.4 to simulate the hardness towards the interface, represented by y.

$$y = y_0 + \frac{A}{w \cdot \sqrt{\frac{\pi}{2}}} \cdot e^{\left\{-2 \cdot \left(\frac{x}{w}\right)^2\right\}} \qquad (5.4)$$

The fit offers several parameters to consider. y_0 corresponds to the hardness in the grain interior, w is a length scaling parameter and matches the start of hardness increase and A is scaling factor for the hardness elevation. From the fitted function the hardness at every distance can be calculated. At close distances to the interface the measured hardness is representative of both grains. Therefore, the hardness was evaluated at a distance where the residual imprint would lie only in one grain. This happens when the distance to the interface is equivalent to the contact radius a_c. For spherical indentation with 4.5 µm apex radius and 200 nm indentation depth, this value is at 1.4 µm distance. The hardness increase ΔH_{a_c} can be presented in a relative manner at this distance to the interface, see formula 5.5.

$$\Delta H_{a_c} = \frac{y(x=1.4\ \mu m)}{y_0} \qquad (5.5)$$

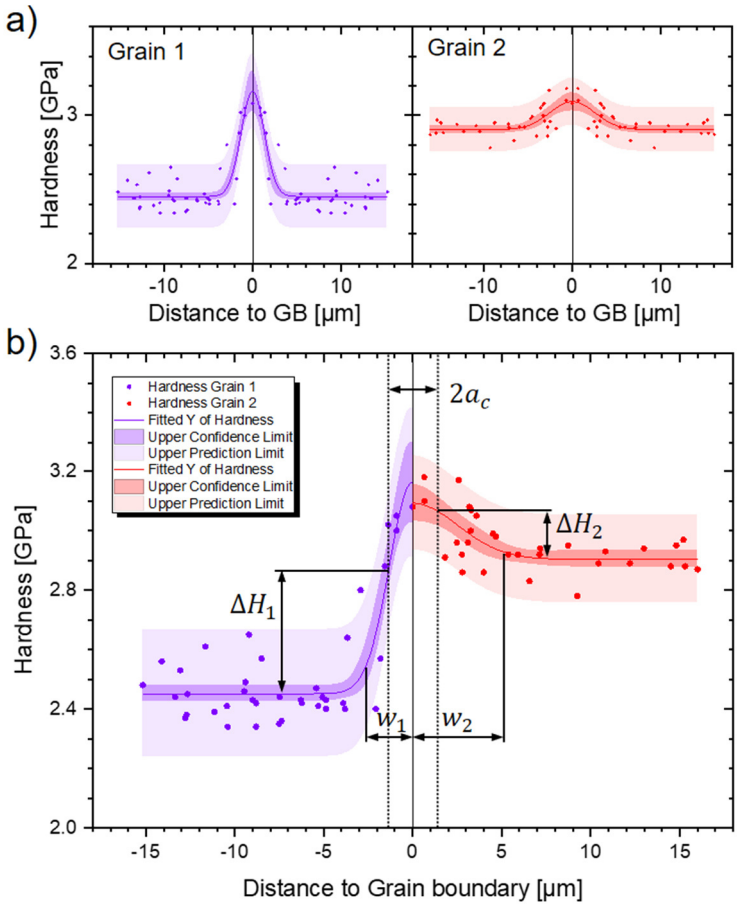

Fig. 5.22: a) Application of the peak fitting to the mirrored data. b) Extraction of parameters from the fitting functions.

Applying the described method to the hardness profile in Fig. 5.21, the two individual fits for each grain are presented in Fig. 5.22a and the resulting hardness parameters are depicted in Fig. 5.22b and Table 5. The fitted hardness of the grains are 2.45 GPa and 2.9 GPa, respectively with increasing hardness starting at 2.6 µm and 5.1 µm, respectively. From the fitting function the hardness can be calculated at 1.4 µm distance and the relative hardness increases are 16.4% in Grain 1 and 5.6% in Grain 2.

Table 5: Results of the fitting method applied to the data in Fig. 5.21.

	y_0 [GPa]	w [µm]	A [µm]	$\Delta H_{1.4\mu m}$
Grain 1	2.45 +/-0.01	2.61 +/-0.27	2.33 +/-0.19	16.4%
Grain 2	2.90 +/-0.01	5.07 +/-0.89	1.20 +/-0.23	5.6%

5.1.6. Influence of the neighboring grain and misorientation

It has already been established that a hardness increase is observed if enough deformation is pushed towards the GB. In this chapter, the influence of the adjacent grain on the hardness increase will be discussed.

On a sample with mm-sized grains of pure Mo was an area where one grain near (001) orientation was flanked by similar crystals with near (103) orientation. Fig. 5.23 depicts SEM micrographs of the indentation arrays at the investigated interfaces, deformation patterns around spherical indentation to 1250 nm, IPF maps and the crystal lattices of the involved grains. The <111> direction lines in the IPF maps are consistent with the deformation pattern in the BSE micrographs.

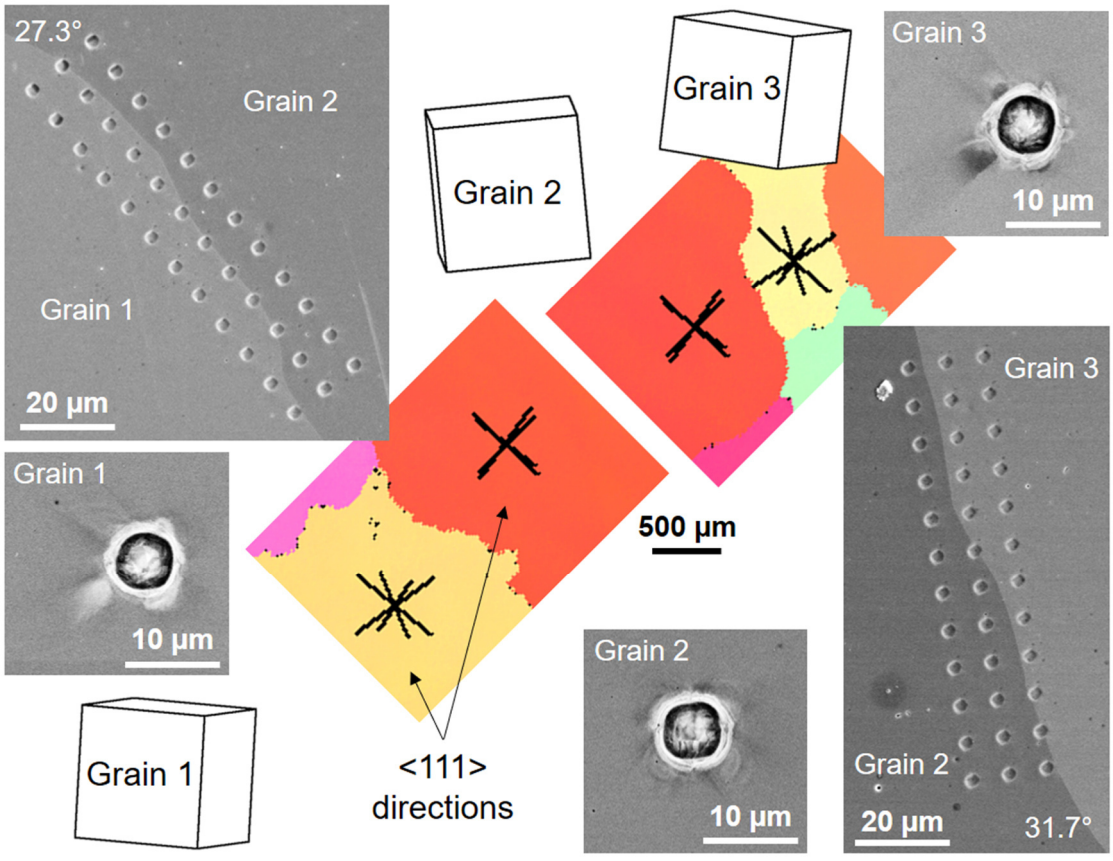

Fig. 5.23: IPF map as well as BSE micrographs of the indentation arrays and reference indentations at the area with different deformation predispositions (see text).

The almost symmetrical deformation paths in the middle Grain 2 and the similar deformation pattern in the adjacent Grains 1 and 3 results in two distinct predispositions.

Case (i): Deformation near the sample surface is predominately pushed towards the interface from one grain and pushed away in the adjacent grain (GB 1-2).

Case (ii): Deformation is pushed towards the interface from both grains (GB 2-3).

Figure 5.24 shows the hardness and modulus profiles of both interfaces. The first boundary represents case (i) where the deformation is pushed away from the interface in Grain 1 (near (103) orientation). The hardness fit in this grain shows almost no increase towards the interface. Only directly at the boundary, an increased hardness is detected. The second interface, mentioned as case (ii), receives deformation from both grains. The hardness increase in Grain 3 shows a hardness increase of 10% at 1.4 µm from the interface. The hardness in the middle, near (100) orientation, Grain 2 shows similar hardness increase for both interfaces.

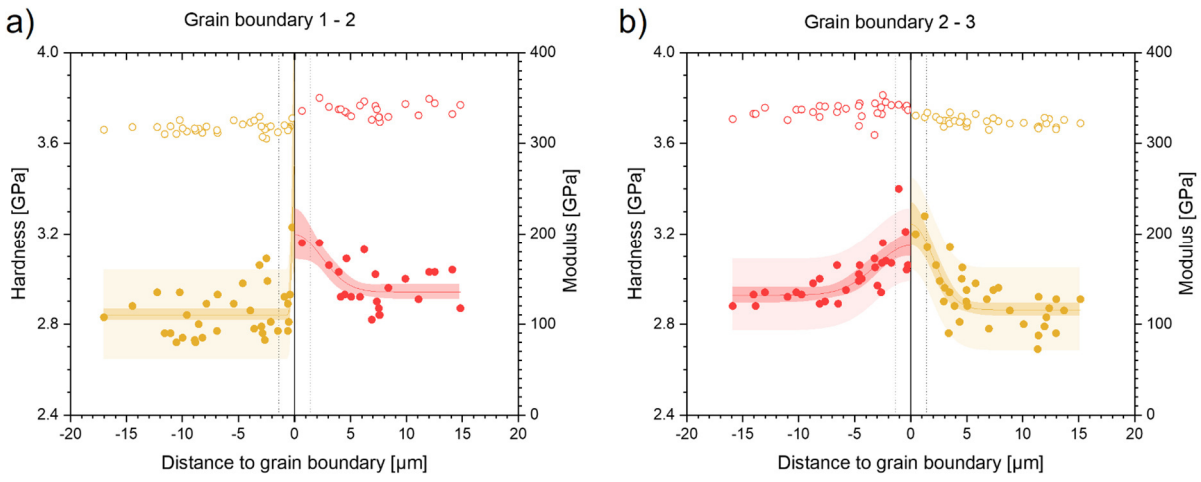

Fig. 5.24: Hardness (solid symbols) and modulus (open symbols) data with fitting functions for a) GB 1-2, representing case (i), where the interface experiences deformation predominately from only one grain and b) GB 2-3, where the indentations in both grains introduce deformation towards the GB (see text).

Table 6: Fitted parameters for the hardness in approximation of the GBs 1-2 and 2-3 as well as the angle of attack of the deformation.

	y_0 [GPa]	w [µm]	A [µm]	$\Delta H_{1.4\mu m}$	Angle of attack
Grain 1, case (i)	2.84	0.36	0.30	0.0%	-90°
Grain 2, case (i)	2.94	4.79	1.54	7.4%	70°
Grain 2, case (ii)	2.93	6.07	1.68	6.8%	64°
Grain 3, case (ii)	2.86	3.94	1.88	10.3%	78°

Beside the hardness increase and start of hardness elevation, the angle of attack is depicted in Table 6. This value represents the angle in the plane of the sample surface between the main deformation direction and the GB. The inclination of the GB is not available from investigation at the surface. To evaluate the angle of attack within the sample, cross-sectioning using the FIB is necessary. For these two GBs cross-sections were performed and are depicted in Fig. 5.25. Incidentally, in both cases the interface is inclined about 13° towards the middle Grain 2. Therefore, in both cases the approaching deformation in the middle Grain 2 encounters a similar geometrical impediment from the GB plane.

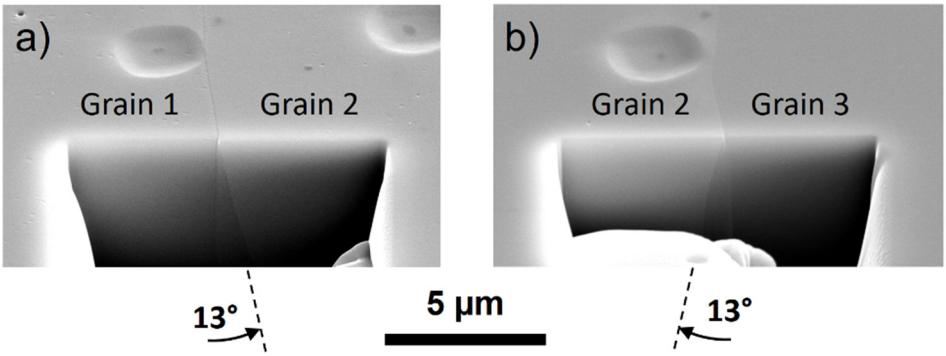

Fig. 5.25: FIB cross-section of a) GB 1-2 and b) GB 2-3 revealing in both cases 13° inclination towards the middle Grain 2.

To evaluate the hardness increase as a function of misorientation, several grains with (101) orientation were selected. The GBs between these grains have per selection tilt character with different misorientation. Six GBs with similar predisposition of deformation were selected for detailed comparison. In all cases at least one main deformation direction leads towards the interface. Arrays of spherical indentations were placed at these boundaries and the resulting hardness profiles were determined. Fig. 5.26 shows a BSE micrograph of a large indent in the grain interior, the unit cell of the indented grain as well as the hardness in approximation of the interface for each GB. The images and lattice depictions were rotated so that every GB lies at the right-hand side of the micrograph. The misorientation angle is written in one corner of the micrograph, respectively. The deviation of a (101) orientation, misorientation and rotation axis as well as the angle of attack of one of the main deformation direction towards the GB are depicted in Table 7. The parameters w and $\Delta H_{1.4\mu m}$, deduced from the fitting as described in the previous section are presented as well. All six GBs display distinct hardness increases between 13% and 21% in the hardness profiles. The hardness increase starts between 5.2 µm and 13.7 µm.

Table 7: Geometrical considerations as well as the fitted hardness parameters for the six analyzed GBs, depicted in Fig. 5.26.

GB	Misorientation		Orientation deviation from (101)	Angle of attack	w [µm]	$\Delta H_{1.4\mu m}$
	Angle	Axis				
a)	13.2°	(-14 -1 -11)	7.2°	78°	8.4	20%
b)	27.2°	(-10 -11 3)	8.7°	63° (& 46°)	7.6	13%
c)	36.7°	(3 1 5)	8.7°	65° (& 45°)	7.1	15%
d)	40.8°	(-6 -9 7)	16.1°	81°	6.1	14%
e)	49.1°	(7 9 2)	7.2°	80°	13.7	21%
f)	57.7°	(8 -9 -4)	17.5°	88°	5.2	13%

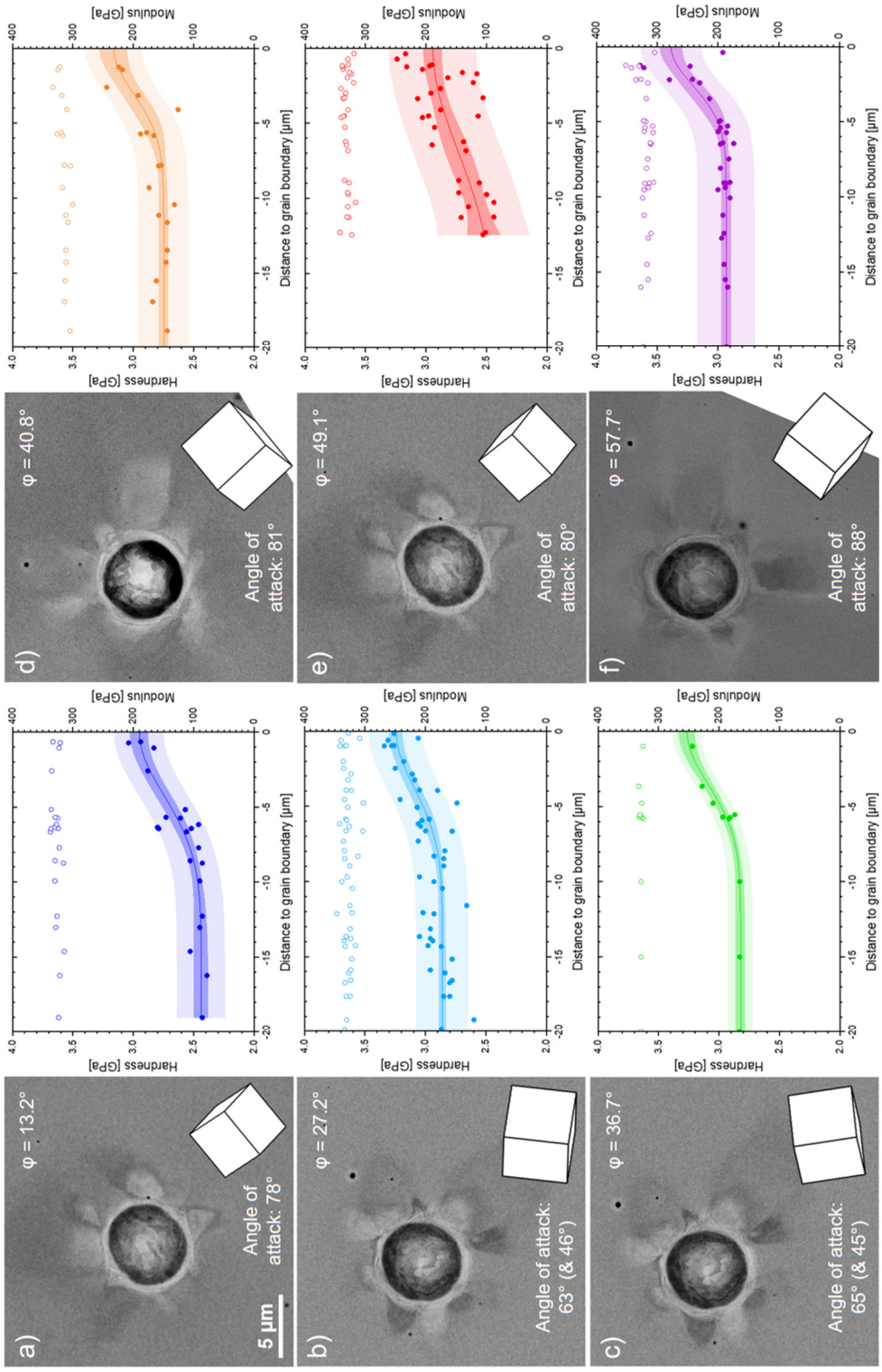

Fig. 5.26: BSE micrographs of imprints in the grain interior as well as unit cells of the selected grains, which are rotated so that every GB lies at the right-hand side of the micrograph. The misorientations of the GBs as well as angles of attack of the main deformation direction are indicated. Hardness (solid symbols) and modulus (open symbols) as a function of distance to the boundary as well as the hardness fit of the spherical indentation arrays are depicted next to the micrographs.

5.1.7. On the influences during indentation experiments

Since nanoindentation is a surface sensitive technique, we start with considering the role of surface condition on the resulting data. The final preparation step of the samples is electro-polishing to remove any deformed surface layer. However, this preparation might result in grooves at the GBs, as exemplarily illustrated in Fig. 5.3e in section 5.1.1. An uneven surface could lead to inaccuracies during surface detection of the indentation experiment and therefore lead to faulty data. In case of an inclination of the surface, the contact area may be overestimated. If the indentation is positioned directly at the groove, the detection of the surface could be delayed. During the experiment, the indenter would then experience a larger contact area $A_{real}=f(h+hs)$ than the seeming contact depth suggests ($A_{apparent}=f(h)$). Consequently, the current load is higher than expected for the apparent contact area and therefore hardness as well as modulus are overestimated. With increasing indentation depth this error drops in significance. As the contact area also enters Sneddon's equation to calculate the Young's modulus, this property can open up the possibility to correct the measurement if a reference value, e.g. the bulk value, is given [158]. Mo has an elastic anisotropy and the elastic moduli values are E_{001} = 345 GPa, E_{101} = 323 GPa and E_{111} = 317 GPa, respectively [159]. Since the stress field under the indenter tip is complex and reaches in all three dimensions, the measured modulus is a mixture of the uniaxial moduli. The experimentally observed values are consistent with the materials anisotropy. The actual contact area A_{true} can be calculated by using a reference modulus E_{ref} with the stiffness S and the geometry factor β as shown in formula 5.6. With this true contact area the true hardness can be evaluated. The Young's modulus as a function of indentation depth for the experiments shows good consistency as can be seen for example in Fig. 5.6c and d. Furthermore, the modulus data for spherical indentations, for instance in Fig. 5.15 in section 5.1.3, depict constant modulus values at about 320 GPa. Therefore, we can exclude for this study that the surface topography at the GBs significantly influences the mechanical properties.

$$A_{true} = \frac{1}{\beta^2}\frac{\pi}{4}\frac{S^2}{{E_{ref}}^2} \qquad (5.6)$$

Any influence of more than one GB can be ruled out since the grain size is significantly larger than the deformed volume underneath the impressions. Machining into the surface

with the use of an FIB after the experiments revealed the inclinations of the boundaries (see Fig. 5.14 in section 5.1.2 and Fig. 5.25 in section 5.1.6). Additionally, the presence of another GB underneath the indented area could be excluded. Consequently, the observed hardness increase can only be caused by the interaction of the introduced dislocations with the GB.

To further analyze the interaction of dislocations with the GBs, it is important to introduce plastic deformation towards the boundary. Nanoindentation has been established as a characterization method for GBs in several studies in the past [64–71,76]. However, most studies focus on the apparent hardening exactly at the GB. For different bcc metals the reported values for the hardness increase directly at the GB vary between 14% and 35% [67,68,76]. In these studies as well as our investigation, the deformation is introduced by the imprint of the indenter tip. Another approach to investigate the interaction of plastic deformation, i.e. dislocations, with GBs is the indentation of recrystallized and slightly compressed samples, where a hardened zone with thicknesses between 10 µm and 40 µm in proximity of the GB was reported for bcc [70,71] and fcc metals [69]. The development of a hardened layer in the vicinity of GBs for deformed samples indicates an impeded deformation at the interface. This must be differentiated from the hardness increase of the studies mentioned earlier, as well as this study, where a hardening was measured only within the first micrometers of the GB in undeformed samples. However, the reason for the impediment is in both cases the interaction of dislocations with the GB.

The development of deformation patterns is inevitable since plastic deformation is carried out by discrete dislocations in defined slip directions on the corresponding slip planes. In case of a bcc metal, deformation is realized by slip in the <111> directions and on {101}, {112} or {123} planes of the crystal [160]. Since these planes are equivalent and are simultaneously active during the deformation, they cannot be distinguished. For geometrical considerations, the face angle of the indenter tip plays a role for the Schmid-factor of the different slip systems. Another important influence is the rotation angle α of a pyramidal tip around the loading axis, as illustrated in Fig. 5.11 in section 5.1.2. For the case of 30° rotation, two faces of the Berkovich tip are perpendicular to the [1-11] and [-111] direction and introduce significant deformation along these axes (Fig. 5.11a). The [1-1-1] as well as [-111] directions are expected to exhibit similar material pile-up since the inclination is almost horizontal. Notably in the [1-1-1] direction, no major deformation is apparent which can be explained by the vertex of the Berkovich tip facing in this direction and impeding the

deformation. At 90° rotation angle, where vertices and faces are interchanged compared to α = 30°, significant deformation can be observed in the [1-1-1] direction and no deformation along the opposite [-111] direction (Fig. 5.11c). Spherical indentation has not the confinement of the different faces like a pyramidal tip. Therefore, the deformation is distributed more evenly between the different <111> directions of the crystal (Fig. 5.11d). Both the Berkovich and spherical imprints introduce extensive deformation in the [1-11] direction as can be seen in Fig. 5.11a and d.

To elucidate the intrinsic deformation behavior, several spherical indentations were performed in grains near particular crystal orientations as can be seen in Fig. 5.15. The consistent modulus data of at least two indentations per crystal orientation suggest valid experimentation. The hardness as a function of indentation depth depicts different hardness plateaus, which stem from the activation of several slip systems. In contrast to a Berkovich tip, spherical indentation experiences different opening angles of the indenter geometry and thus strains during the experiment. From the DIC micrographs distinct pile-up directions around the imprint are present and can be attributed to the <111> directions of the crystal lattice. From the experiments, a major material pile-up around the impression is expected when a slip direction has almost horizontal inclination or is facing slightly out of the sample surface. These empiric observations are in accordance with investigations by Yu et al. [161]. They performed nanoindentation on bcc W and correlated the pile-up with crystallographic directions. Increased pile-up is connected to an out-of-plane Burgers vector and in the case of Burgers vector lying near parallel to the sample surface, long streaks of deformation are observed. Xia et al. performed similar experiments on austenitic stainless steel [162]. They discriminate between sideway and forward flow of deformation near spherical indentations. As the names suggest, the material flow is directed either away from the imprint or to the side depending on the inclination of the corresponding slip plane. They identify a transition angle of 55° to 58° between slip plane and sample surface which determine the dominate mode of deformation flow. Xia and co-workers performed their study on fcc austenitic steel, however, the principle concept of crystallographically favored directions of deformation should be analogous for bcc Mo.

Nanoindentation tests a small sample volume, especially at the start of the experiment. As a result, the load-displacement data shows initial pop-ins for materials with a low dislocation density. The analysis of pop-in loads in section 5.1.4 demonstrate the absence

of crystal defects in the recrystallized samples. The necessary stresses for the onset of plasticity correspond to the theoretical strength of Mo. An initial pop-in was still observed close to the boundary. Only directly at the interface, the pop-in was absent. From the experiments, it is not clear if the boundary acts as a strong dislocation source, as was similarly described in literature [68].

The plastic zone underneath the indenter tip expands with increasing indentation depth. The most emphasized hypothesis regarding the hardness increase at GBs is the blocking of the dislocations at the interface [68,79]. For an expedient characterization of GBs it is essential to abstain from the assumption of a spherical plastic zone underneath the indentation. Fig. 5.5 and Fig. 5.11 clearly show distinct deformation patterns depending on the indented crystal orientation. In case of an impermeable GB, i.e. a GB with high slip transfer resistance, the dislocations underneath the indentation, which are driven towards the boundary, are confined between the GB and the massively deformed center of the plastic zone. A reduced spacing of the indentation center in regard to the interface consequently leads to a more pronounced dislocation pile-up, eventually resulting in a higher local hardness and reduced indentation size effect. From this perspective, it is clear that only for the case, where the deformation is mainly pushed towards the GB a dislocation pile-up is decisive for the obtained hardness, as demonstrated in Fig. 5.6e and f for the (001)-(101) GB. In contrast, only minimal deformation is observed on the opposite side of the indentations in the (001) grain. Therefore, at the boundary (001)-(111) only a minimal interaction is expected, which manifested itself by a negligible hardness increase for the closest indentation at the GB. On one hand, the experiments have shown that for GBs with comparable misorientations the mechanical response exhibits a distinct difference depending on the crystallography of the indented grain. On the other hand, this opens up the possibility to select specific grain orientations and boundaries for mechanical characterization via nanoindentation.

To the best of the authors' knowledge, the rotation of the indenter with regard to the characterization of GBs has not been taken into account so far. To exclude uncertainties Soer et al. [67] as well as Eliash et al. [68] placed the indenter with one side of the pyramidal Berkovich tip being parallel to the GB and performed a line profile of indentations with a small inclination with respect to the boundary. This study demonstrates not only the formation of distinct deformation patterns around the indenter tip, but also confirm that the direction of deformation is dependent on the crystal orientation of the grain, as was also described in

literature [163,164]. The extent of the deformation is, however, additionally depending on the rotation angle α of the indenter as demonstrated in section 5.1.2. The indentations in the vicinity of the boundary with two different rotation angles, namely 30° and 90°, demonstrate the strong influence of the indenter shape and rotation angle α on the deformation pattern under the imprint as depicted in Fig. 5.13. Particularly in the case of 30° rotation, where a large proportion of plastic deformation is introduced in front of one face of the indenter towards the GB, an increase of the local hardness is observed. The second array of indentations was conducted with α = 90°, where the vertex between two faces of the indenter tip is pointed towards the same boundary. Here, no hardness increase was noted, even at a smaller distance to the GB than for the 30° rotation angle. These findings confirm our hypothesis that an increase in hardness can only be observed if a large proportion of dislocations is introduced in the direction of the GB. Additionally, the appearance of a second dislocation burst, a so-called GB Pop-in [77,79], might be equally dependent on the indenter rotation as reported in [67].

To compare the hardness response of individual GBs, certain conditions have to be met. First, deformation has to be pushed towards the interface. Only then the hardness data as a function of distance to the boundary shows a distinct increase, which can be fitted by a peak-function. The extraction of the two parameters w and $\Delta H_{1.4\mu m}$, as described in section 5.1.5, allow the comparison of tangible values. Second, to compare different boundaries the deformation should happen in a similar manner. With this groundwork laid, the influence of the neighboring grain in regard to deformation pattern and misorientation was evaluated in section 5.1.6. The hardness response of the near (001) oriented middle Grain 2 showed no significant deviations, despite the opposite extension of deformation in the neighboring Grains 1 and 3 with near (103) orientation. These grains however clearly demonstrate the importance of the deformation direction on the hardness increase again. Since the indentation in Grain 1 pushes deformation away from the boundary, hardness is elevated only directly at the interface. In contrast, Grain 3 experiences raised hardness values already at about 4 µm away from the interface. Furthermore, the influence of misorientation was tried to ascertain. Six boundaries next to grains near (101) orientation were investigated. Due to this orientation, distinct deformation along at least two directions lying near the sample surface plane is expected. All selected interfaces experience deformation from similar angles of attack. The experiments reveal no correlation between the hardness increase and the misorientation of the boundary. Seemingly, the position and inclination of the interface in

regard to the introduced deformation is a stronger influence than the atomic arrangement of the boundary itself.

In conclusion, GBs can be characterized by means of nanoindentation. The use of a pyramidal indenter geometry, like a Berkovich tip, introduces one additional loading parameter in form of the rotation angle α around the loading axis. Nevertheless, the impact of the indenter geometry could likewise be used as a feature to enhance deformation along a specific crystallographic direction. In contrast, spherical nanoindentation uses a rotationally indifferent tip geometry, where the rotation along the loading axis has no influence on the imprint. In the latter case, the deformation pattern corresponds only to the intrinsic deformation paths of the indented crystal. The same conclusions can be drawn for fcc and hexagonal close packed materials, since the impression of the indenter tip has to be geometrically fulfilled by dislocations in their respective directions. By applying a peak fit function to mirrored hardness data, tangible parameters for comparison can be extracted. The most important factors influencing the amplitude of hardness increase near a GB are the deformation disposition in the indented grain as well as the boundary inclination concerning these crystallographically favored directions.

The potential for the mechanical characterization of GBs will be discussed in comparison to the other micromechanical testing methods in section 5.4.

5.2. Micropillar compression

In contrast to nanoindentation, where the penetrating indenter geometry induces a complex three-dimensional stress field, pillar compression allows for micromechanical materials testing with a defined, uniaxial stress field. Since the pillars are cut free from the surrounding material, only compressive stress is applied on the probed sample volume.

5.2.1. General aspects and slip traces analysis at grain boundaries

Through nanoindentation experiments, information about the materials hardness and modulus can be obtained. However, due to the complex stress field, little to no information of the activated slip systems is available. During pillar compression, the freestanding sample volume and the defined stress state enable the study of activated slip planes. The intersection of slip planes with the surface of the pillars are visible as slip lines. Excessive shearing on any particular slip plane results in the shearing of the top part of the pillar. By comparing the occurring slip lines between the different grains on a bi-crystalline pillar, two general cases at the GB can be studied:

Case (i): The activated slip system of one grain within the pillar impedes on the GB and dislocation motion continues on a favorable aligned slip system in the adjacent grain. This phenomenon is known as slip transfer or transmission. Fig. 5.27 depicts two pillars of the first series of samples in pure Mo plate material. The stress-strain data is displayed after calculating the load-displacement data with the pillar geometry (Fig. 5.27c) as well as an EBSD micrograph (Fig. 5.27d). In contrast to nanoindentation, where the increasing deformation volume and the geometrically necessary dislocations lead to the so-called indentation size effect, the freestanding geometry during micropillar compression allows to assess the stress during deformation along specific slip planes throughout the experiment. Pillar 1 was fabricated in the grain interior and shows shearing along the same group of slip planes, which were identified as {112} with the slip direction <-1-11>. The stress-strain data in Fig. 5.27c indicate the rather rapid deformation of the pillar by the distance of the individual data points. This is expected, since the advance of the flat-punch indenter is inherently load-controlled and only quasi displacement-controlled by a feedback loop. After reaching the critical shear stress, the

dislocation sources release a cascade of dislocations leading to the shearing of the whole pillar. Pillar 2 was fabricated at a GB with 38° misorientation and the interface's inclination is rather vertical, as can be seen in the electron micrograph (Fig. 5.27b). The same set of slip planes is activated in the right-hand half of the pillar as in the grain interior. Apparently, the deformation happened in compliance between the two grains, which is visible by the connecting slip lines on the pillar surface at the GB. After evaluation of possible slip systems, the {011} plane was identified as the active slip plane in the adjacent grain. The depicted slip transfer represents a special case, since the combination of both <1-11> and <-1-11> slip directions align almost perfect with the slip direction in the initial grain. In contrast to Pillar 1, the stress-strain data for Pillar 2 shows no deformation burst but rather uniform deformation during the experiment at similar stress level.

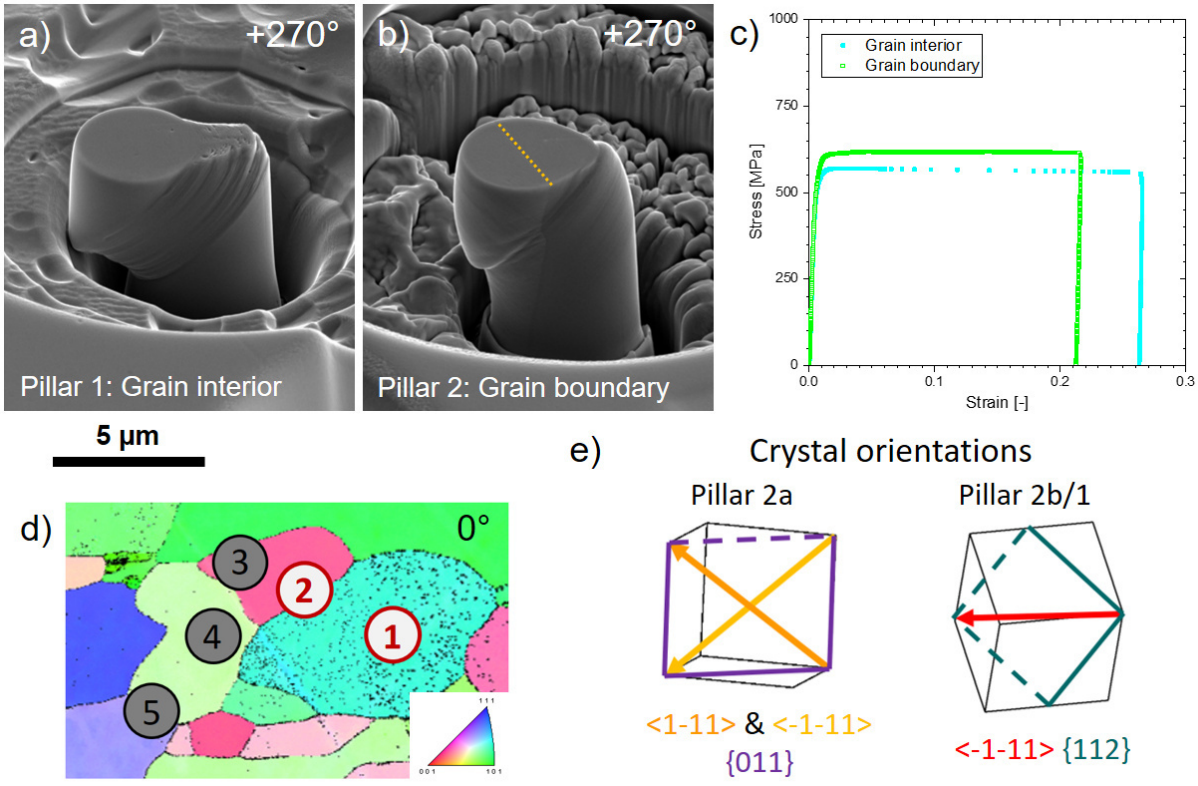

Fig. 5.27: Deformation of pillars a) in the grain interior (Pillar 1) and b) at a GB (Pillar 2) with 38° misorientation. c) Diagram of the stress-strain data. d) IPF map of the position of shown pillars. e) Involved slip systems in the single- and bi-crystalline pillar.

Case (ii): The activated slip systems of each pillar-'half' are aligned in a way that dislocation slip is blocked at the interface. Fig. 5.28 shows an example for this case, where apparently no continuous slip lines reach across the GB. The GB has a similar misorientation of 34° as the interface presented above. The pillar is depicted from different sides in electron micrographs (Fig. 5.28a to d). The corresponding position within the IPF map can be seen in Fig. 5.28e. From the stress-strain data (Fig. 5.28f) the activation of different slip systems is indicated by the different stress plateaus. Only at a strain of about 16%, the step-like stress-strain curve is superseded by a continuous increase of stress. This is representative of forest hardening caused by the dislocation interactions.

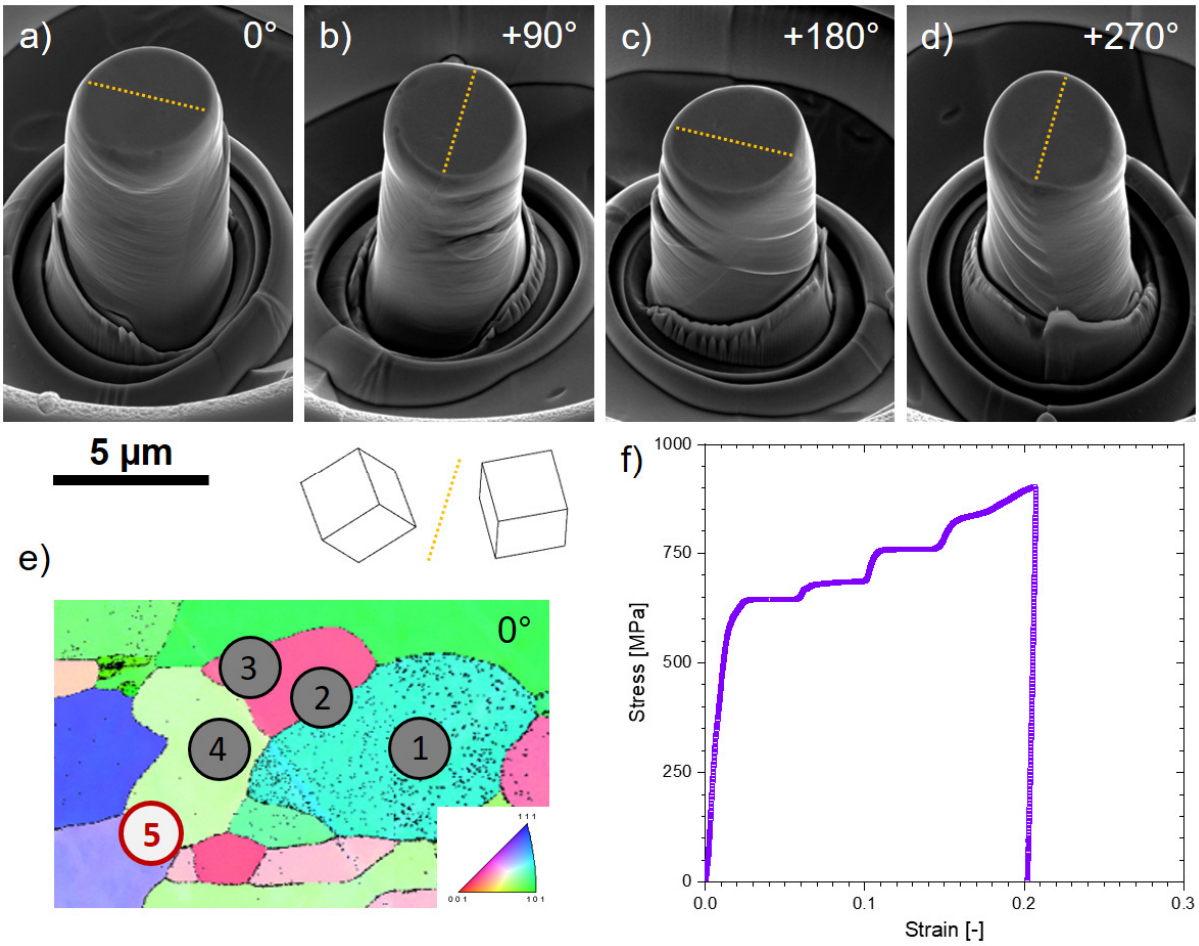

Fig. 5.28: a) to d) Electron micrographs of the deformed Pillar 5 from different viewing angles. e) IPF map of the position of the pillar. f) Stress-strain data showing increasing stresses.

The slip lines at the surface of the pillars give a more or less obvious indication of slip transfer. Beside the alignment of slip planes and directions, the critical resolved shear stress leading to the activation of specific slip planes is another important influence. A simple criteria for the prediction of slip transfer is shown in formula 5.7. The introduced parameter STr combines the Schmid-factors m_{in} and m_{out} with the geometrical alignment, expressed by $m' = \cos(\psi)\cos(\kappa)$, by simple multiplication.

$$STr = m_{in} \cdot m_{out} \cdot \cos(\psi)\cos(\kappa) \quad (5.7)$$

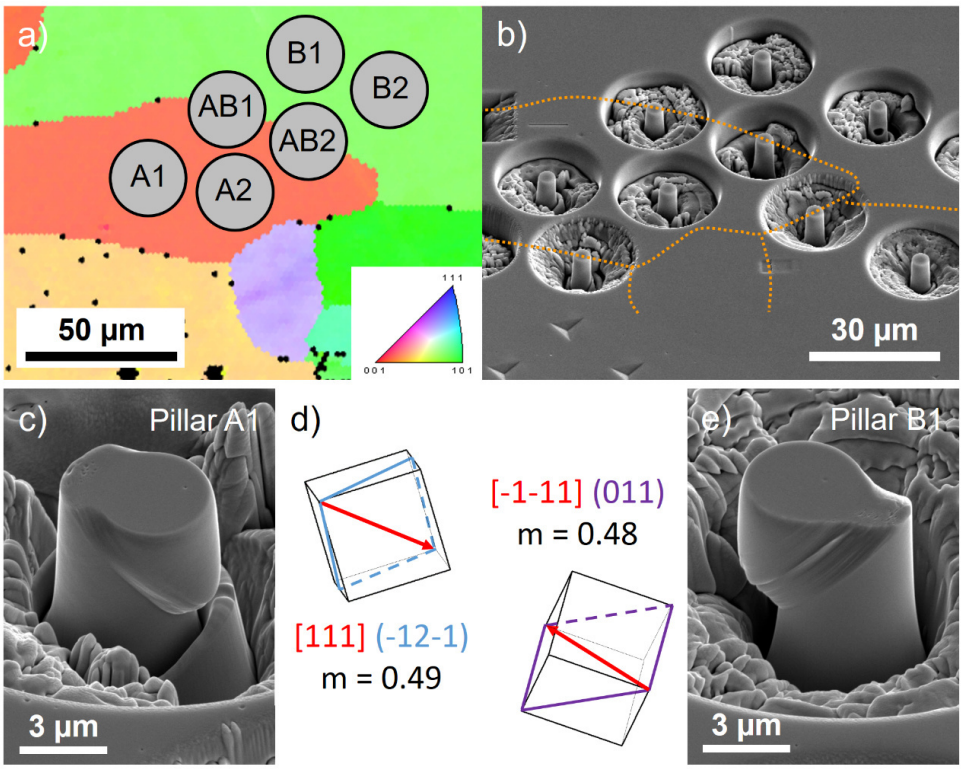

Fig. 5.29: a) IPF map and b) electron micrograph of pillars in Mo plate material. c) and e) depict one deformed pillar in each grain interior. d) Slip systems with highest Schmid-factor in the grains.

Another series of pillars in Mo plate material is fabricated in the grains and at the GB, as can be seen in Fig. 5.29a and b. The activated slip systems in the grain interior have high Schmid-factors and glide in opposite directions. At the GB (Pillars AB1 and AB2) slip transfer occurs. The involved slip systems were analyzed and compared to the prediction by the parameter STr. For the highest STr, slip transfer seems to be favorable, however, the actual

slip transmission is activated by the same Burgers vectors but on different slip planes (Fig. 5.30).

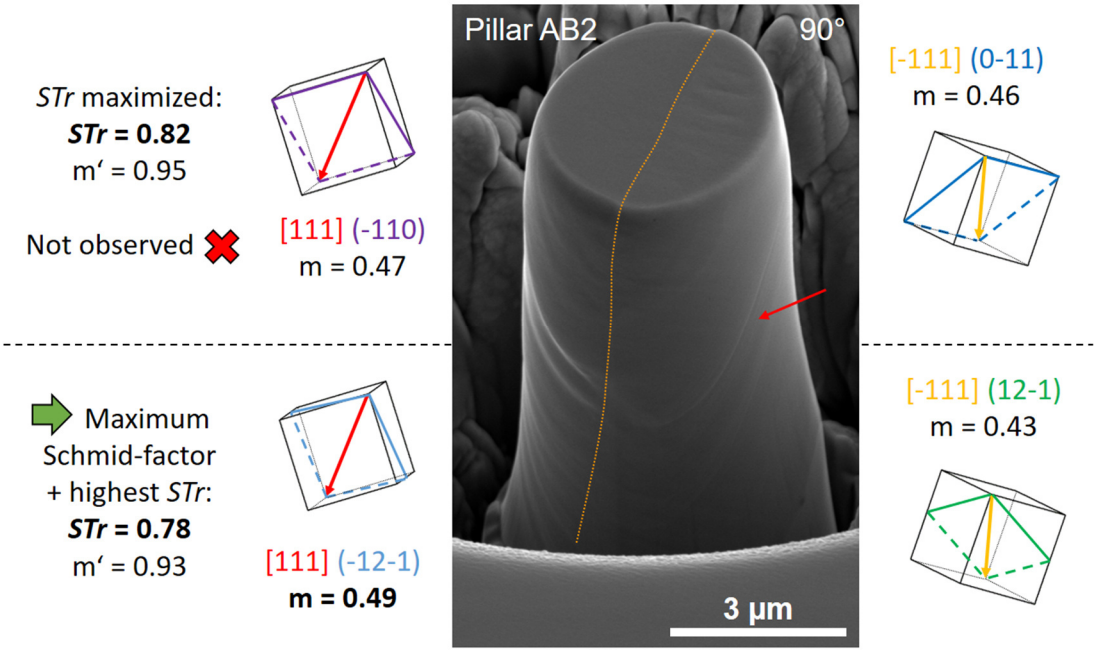

Fig. 5.30: Calculated, possible slip systems for slip transfer in Pillars AB1 and AB2. The slip system pair with the highest STr parameter was not observed in post-mortem *images. Instead, the slip system with the highest Schmid-factor in combination with best geometrical alignment could be seen after deformation.*

In another instance, the highest STr parameter concluded that two slip system pairs were favored for slip transfer in the bi-crystalline pillar. On one hand, a high geometrical alignment with m'=0.89 was calculated in combination with relatively low Schmid-factors of 0.38 and 0.35. On the other hand, the second slip system pair with the same STr value comprised of m'=0.68 and high Schmid-factors of 0.45 and 0.40. *Post-mortem* observations of the deformed pillar confirm the occurrence of the first slip transmission. This indicates that the geometrical alignment might be a precondition for slip transfer.

5.2.2. Deformation of similar pillars in Mo and MoB

Information on the GBs in the different materials might be assessed by testing of GBs with similar slip system alignments to elucidate differences in slip transfer disposition. To test GBs with comparable conditions, the following criteria should be true:

- Grain orientation pairs are almost identical for both material variants.
- The crystals are facing in the same direction in relation to each other. In other words, the rotation between the adjacent grains is the same.
- Alignment of the GB towards the grain orientations is the same, both in the plane of the sample surface as well as the inclination into the sample material.

The fulfillment of the aforementioned criteria is like the proverbial needle in the haystack. However, in this case it would be the search for two identical straws in the bale. A MATLAB script was used to support the search of suitable GB pairs. From approximately 160 000 GBs, 2000 candidates were filtered and manually scanned for proper alignment of the GB line at the sample surface. This was the case for eight candidates and these GBs were chosen for FIB milling. After first coarse milling, the inclination of the boundary was visible. Five more candidates had to be excluded and from the remaining three GB pairs only one pairing had vertical interfaces in both material variants. Fig. 5.31 shows the IPF maps as well as unit cells of the grains and the orientation deviation from the corresponding zone axes. The deviations are all under 6.7° and the misorientation of the GB in the pure Mo material amount to 57.6°, whereas in MoB the misorientation is 51.5°. The orientation of the lattice is slightly different for the near (111) grains. This shows the unavoidable imperfections when comparing GBs in random microstructures.

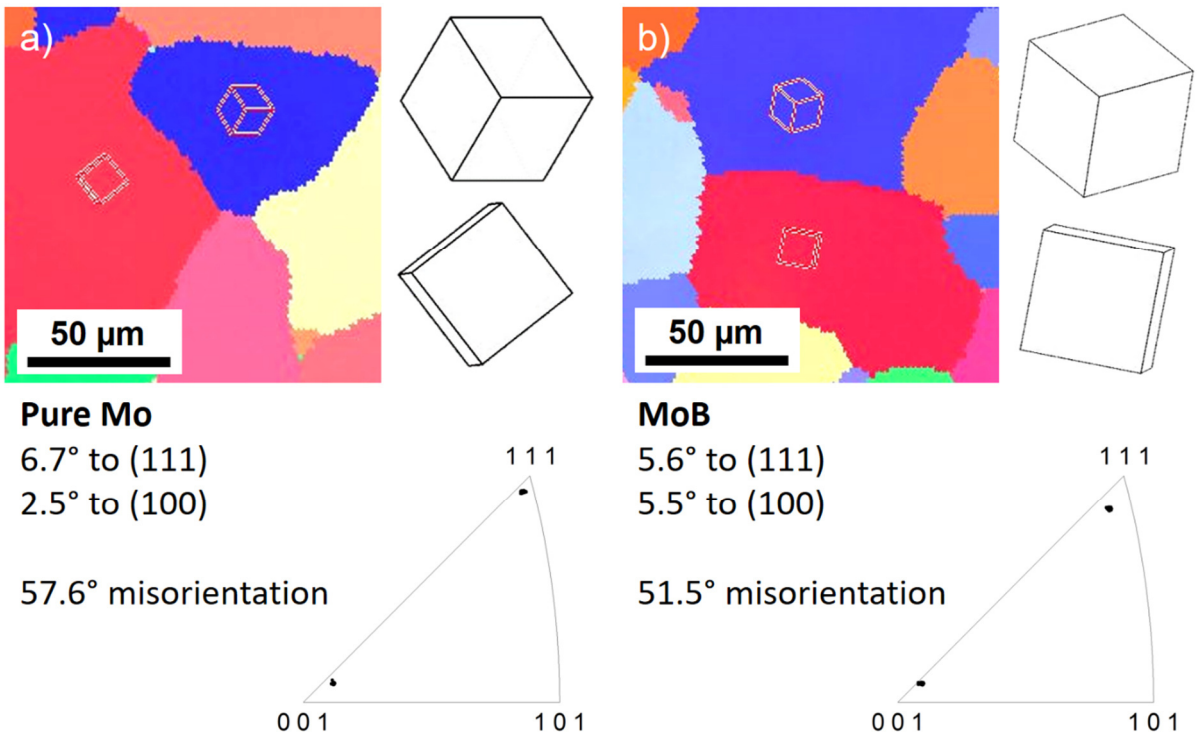

Fig. 5.31: The two 'identical straws'. From 160 000 GBs the depicted interfaces in a) pure Mo plate and b) MoB plate material have the best conformity.

The *post-mortem* electron micrographs of the tested pillars within the grains and at the GBs are depicted in Fig. 5.32. The pillar in the (100) grain for pure Mo shows clearly two active slip systems (Fig. 5.32a). The pillar in the near (111) grain (Fig. 5.32d) shows more distributed slip and only one slip system more pronounced than the rest. The pillar at the GB shows several instances of slip transfer. Unfortunately, the flat-punch indenter had a position offset leading to an eccentric touchdown for the MoB sample. This resulted in the shoulders on the top surface for the pillars as can be seen in Fig. 5.32e to h. In principle, the activated slip systems are similar to the observed slip in pure Mo. The offset of the indenter may have led to less distinct slip activation. This is especially true for the pillar in the (111) grain. The pillar seems to be pushed towards one side with one pronounced slip direction in the opposite way. The pillar at the GB displays slip transmission as was similarly observed in pure Mo.

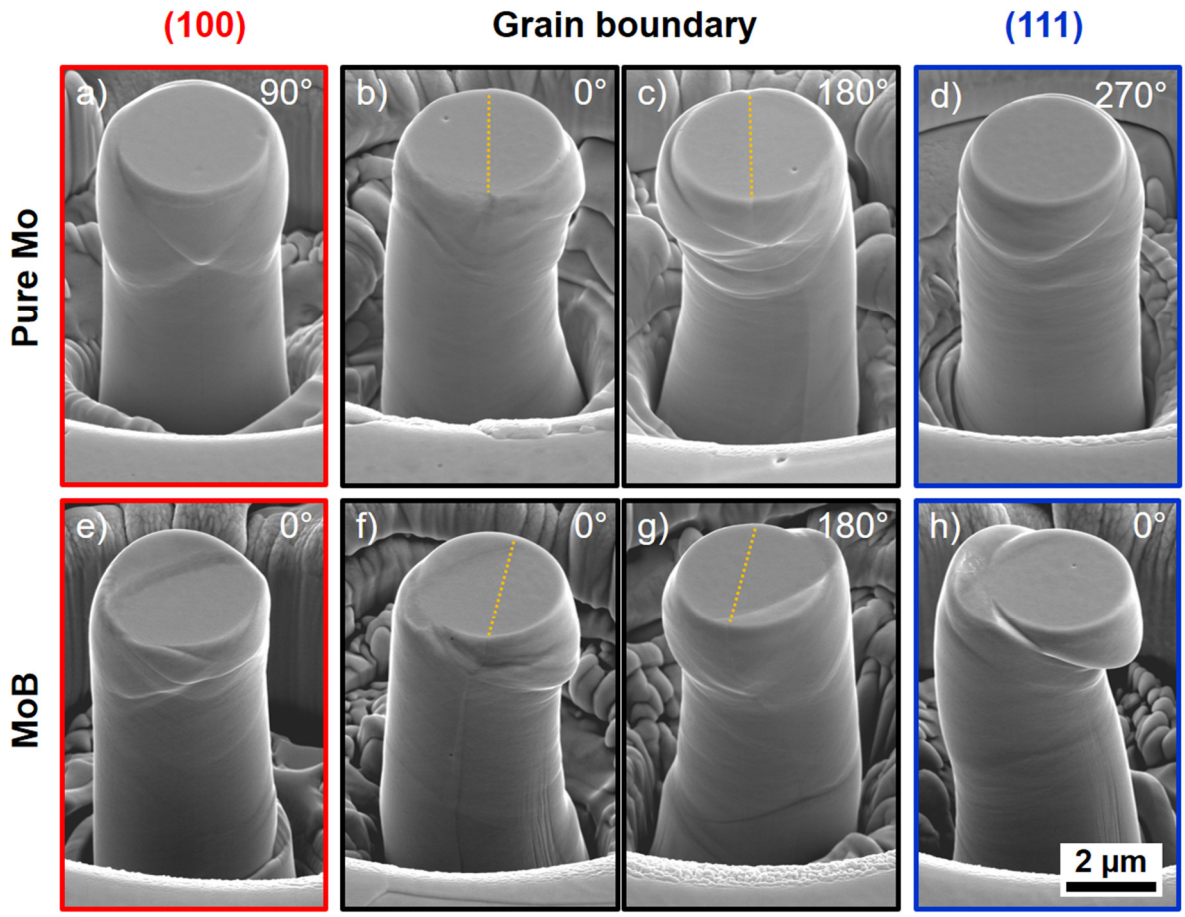

Fig. 5.32: Post-mortem *electron images of the deformed pillars in Mo (a-d) and MoB (e-h) at the GBs and the adjacent grain interior. A shoulder on the top surface of MoB pillars is present due to an offset of the flat-punch indenter.*

The stress-strain data depicted in Fig. 5.33 suggest the activation of only a few slip systems. The stress value of the GB is a par with the pillar in the (111) grain for pure Mo and slightly under the (111) grain for MoB. The (100) pillar in Mo deformed at a lower stress-plateau than the other pillars. In MoB this pillar experiences several increases of the stress value. This might be explained by the offset of the indenter, as it is also the most probable reason for the deviation of a step-like stress-strain curve for the other B-doped pillars. The stresses for the pillars at the GB are not exceeding the single grain pillars. This is somehow expected since slip transfer is observed. The stress values of the pillars compare well between the different materials assuming similar dislocation densities in the recrystallized samples.

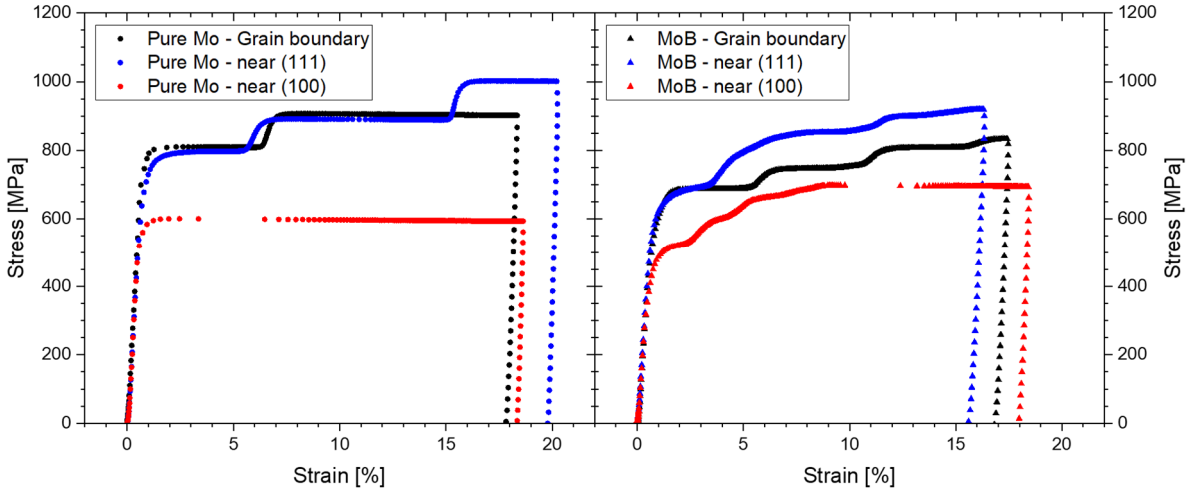

Fig. 5.33: Stress-strain data of the tested pillars at matching grain orientations in pure Mo and MoB plate material.

5.2.3. On the applicability of pillar compression tests on grain boundaries

As already mentioned, the yield stress of the indented pillars underlies a stochastic behavior. The more dislocation sources, the earlier yield occurs. This makes the testing especially sensitive to the sample preparation. A deformation layer introduced by grinding or polishing would offset the measured stresses to lower levels. Therefore, it is necessary to perform electro-polishing as the final preparation step. The FIB milling introduces ion implantation, which is also unwanted, however, unavoidable [84].

As Uchic et al. showed, pillar compression can only ascertain concise stress-strain data if a goniometer is used to align the sample with the flat-punch indenter [80]. To align the indenter parallel to the sample surface, it was pushed multiple times into the material and the goniometer was adjusted until the outline of the indenter was visible as a whole. Another aspect to consider is that during fabrication of the pillars, the sample is positioned in the FIB with the bottom surface aligned to the ion beam, as is schematically depicted in Fig. 5.34a. This could lead to cutting the pillars into a tilted sample top surface. In consequence, the pillars are not loaded along their axis and different slip systems are activated while the pillar is pressed towards one side (Fig. 5.34b) [81]. To avoid this problem, the samples were glued to a special sample holder instead of embedded like classical sample preparation for metallography. In this way, the top and bottom surface of the sample should be parallel.

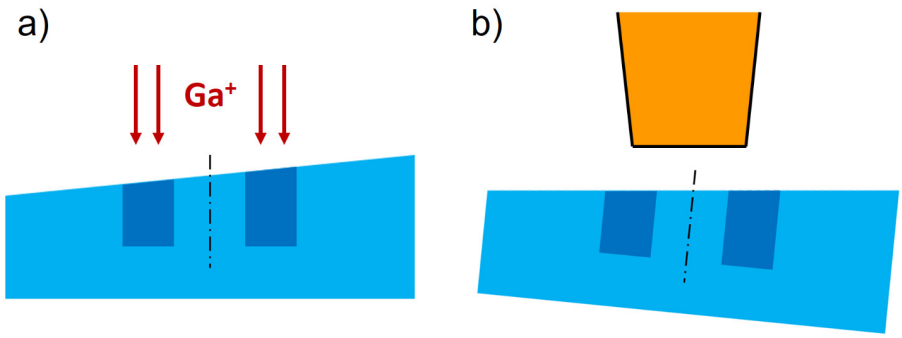

Fig. 5.34: Schematic representation of possible alignment error caused by non-parallel top and bottom surface of the sample (blue color) during a) FIB preparation and b) testing with the flat-punch indenter (orange color).

If care is taken to ensure that no deformation layer is still present as well as alignment of the sample is maintained, load and displacement data can be generated. With the initial recording of sample dimensions from electron micrographs, stress and strain can be calculated. Fig. 5.35 shows the stress-strain data for both plate materials. Note the stochastic behavior of yield stress. The slightly lower yield stresses for the technically pure Mo material might stem from insufficient electro-polishing since the yield values increased on another sample. The data extracted from pillars at a GB are highlighted in color. These yield stresses are in the same range as single-crystalline pillars, indicating no significant influence of the interface. For a direct comparison of the different material variants, interfaces with the same geometrical alignment were searched. From 160 000 GBs only one pair was sufficiently similar to fabricate pillars. The resulting data could not reveal distinct differences between the two material variants.

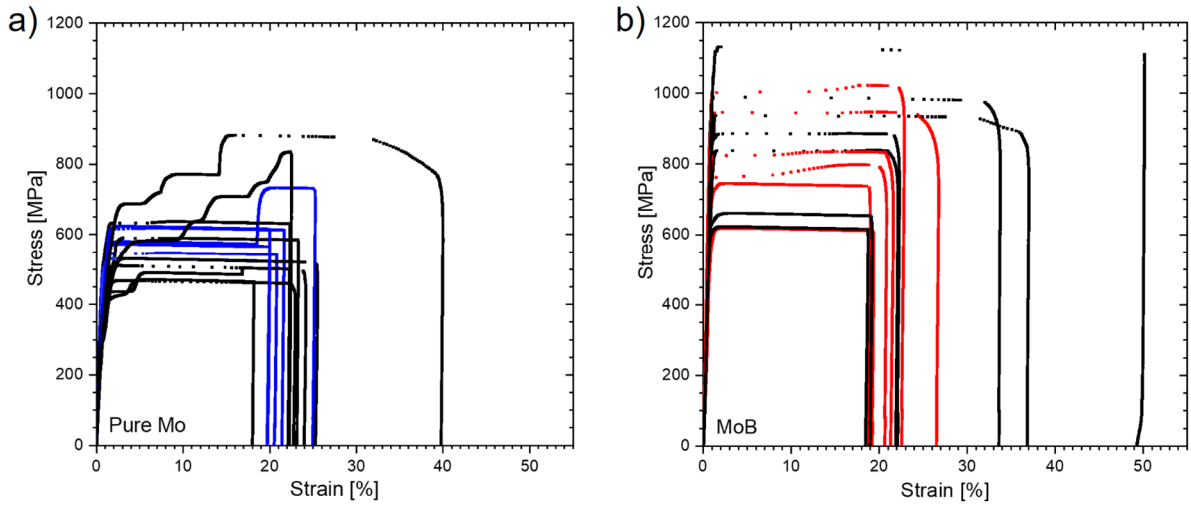

Fig. 5.35: Stress-strain data of one series of pillars for each material variant from plate format. A total of 27 pillars are displayed. 4 pillars at GBs are indicated by blue color for pure Mo and 6 pillars with a GB in MoB are shown in red color.

It was reported in literature that the influence of a GB increases with decreasing size of the pillars [92]. Recent simulations by Xu et al. [165] suggest that the increase in stresses is not only caused by the decreased length scale but in part by the structure of the interface. In case of an impenetrable boundary, the flow stress of the simulated pillar increases during continuous deformation. In contrast, if the interface can release dislocations depending on the GB energy the strain hardening levels off at a higher stress than a single-crystalline pillar-half would suggest. Smaller pillars with 1.4 µm diameter were tested. However, to analyze statistically significant findings, a series of experiments on the same boundary with similar inclination would be required. Since every pillar has to be cut free for the flat-punch indenter in a 25 µm diameter, the microstructure is limiting the number of pillar experiments on the same boundary.

As a proof of concept, the generation of mechanical and chemical data from the same GB was demonstrated by the author in [166]. A thorough comparison of micromechanical testing methods and their limitations and advantages are discussed in section 5.4.

5.3. Micro-sized bending beams

Bending beams serve as another micromechanical sample geometry. Freestanding cantilevers are cut with a FIB workstation and deformed by means of the G200 nanoindenter platform. The loading introduces tensile stress at the top surface and compression at the bottom part of the cantilever. In the following section, the main findings during the experimentation with micro-scale bending beams are discussed.

5.3.1. Notched cantilevers

Pentagon-shaped beams were fabricated by cutting away material from the top and at an angle underneath the cantilevers, as is illustrated in Fig. 2.10 in section 2.3.3. One end of the beam is cut free to get a freestanding specimen. In the last step, a thin notch is introduced from the top as a starting point for crack propagation near the base of the beam. Fabricating the notch is a delicate processing step since it is vital for validating fracture toughness results [167].

Figure 5.36 shows one bending beam at a GB with small length-to-width ratio. In Fig. 5.36a the fabricated notch as well as the position of loading is indicated. The fracture surface is enlarged in Fig. 5.36b and shows rough surface except for one section. This section seems to be the partially separated GB. Apparently, crack propagation was more favorable directly from the notch through the grain than at the GB. Fig. 5.36c shows the recorded load-displacement data as well as the contact stiffness measured with CSM from the nanoindenter platform. The increasing load and displacement shows a rather large proportion of plastic deformation within the sample. The stiffness data reveal no major stable crack propagation, which would reduce the stiffness value. At about 2500 µm displacement the stress concentration at the notch causes instable crack growth and failure of the sample. This is visible by the displacement burst in the nanoindenter data.

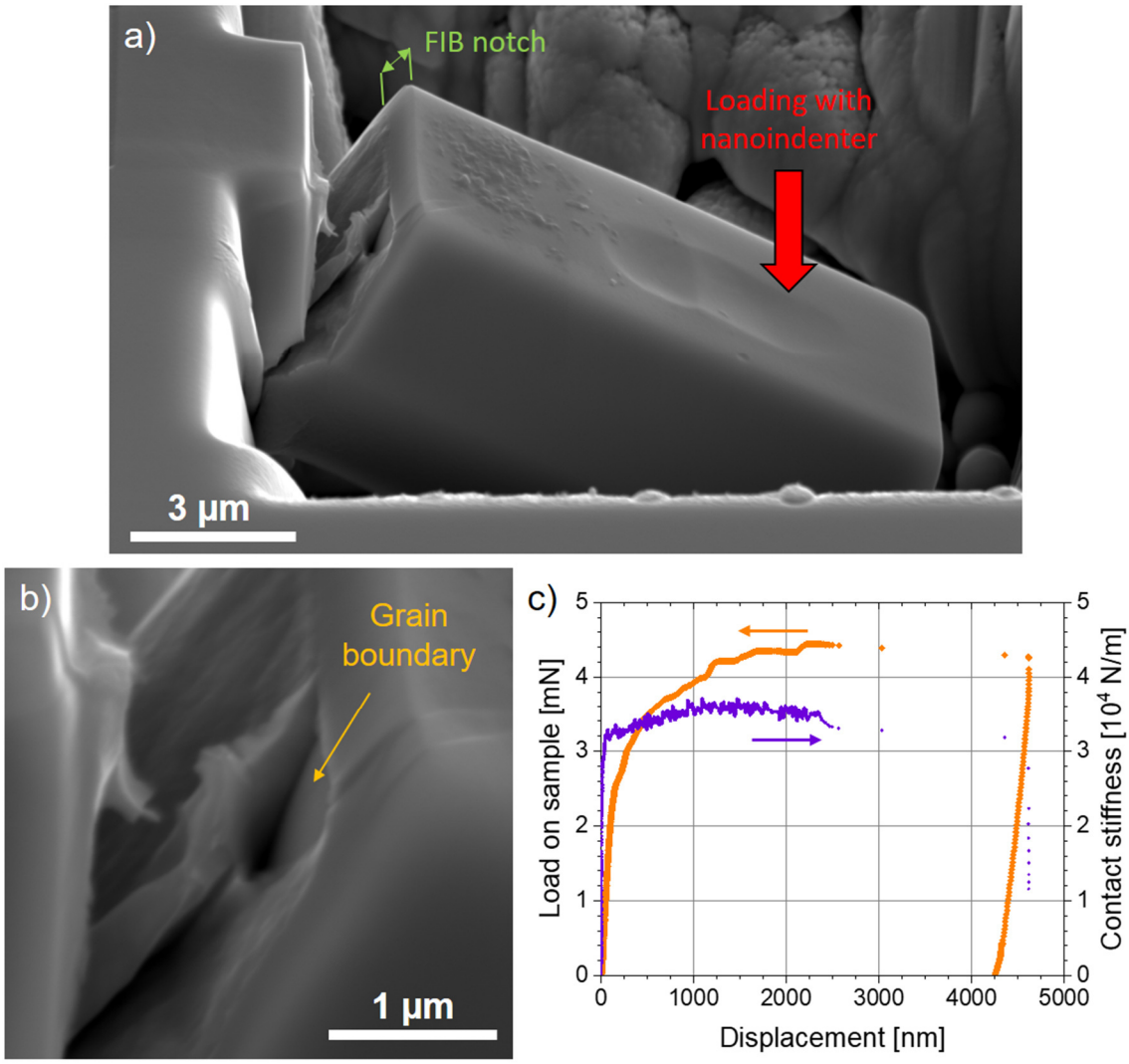

Fig. 5.36: Example of a pentagon-shaped bending beam at a GB. a) The fabricated notch and the position of loading are indicated in the post-mortem *electron image. b) The enlarged image of the fracture surface reveals a partly separated GB and otherwise fracture through the grain. c) Load and stiffness data reveals no significant stable crack growth during the experiment.*

More bending beams, also with larger length-to-width ratio, were fabricated at GBs and in the adjacent grains. The quality of the notch was integral for the fracture of the samples. However, in all cases large proportions of plastic deformation were recorded before fracture of the sample. As a consequence, linear-elastic fracture mechanics were not applicable. Furthermore, the J-integral could not be used for the extraction of fracture parameters, since no stable crack growth was observed.

5.3.2. Unnotched bending beams

To avoid imperfections during notch preparation, another set of bending beams were prepared and tested without a notch. To ensure that the sample would break at the GB or at least at the base of the cantilever, the beam was cut down to a narrow bridge as can be seen in Fig. 2.10b and Fig. 5.37. This was done by cutting away material from the top to introduce a defined breaking point ideally at the GB. Bending beams I and II (Fig. 5.37a) were cut at the GB and beams IIIb and IVb (Fig. 5.37b) in the interior of one of the adjacent grains. The *post-mortem* electron micrographs as well as the load-displacement data show that only at the GB fracture of the cantilevers occurred. Even with the presence of the interface, significant plastic deformation can be observed. The beam with the bridge fractured earlier, interestingly at higher loads than the straight beam. The beams within the grain did not fracture and slip steps are apparent after deformation to 3000 µm displacement. The bridge cut beam showed lower load than the straight one as is expected due to the smaller cross-section. Fig. 5.37c shows a detailed image of the fracture surface of the bridge cut beam at the GB. Assuming that fracture starts at the highest loaded extreme fiber, which is the top surface of the beam, the interface is the weak point of the specimen. However, within a few hundred nanometers, the crack plane seems to divert from the GB and lead through the grain. The fracture surface is smooth in contrast to the fracture surfaces of samples with a notch.

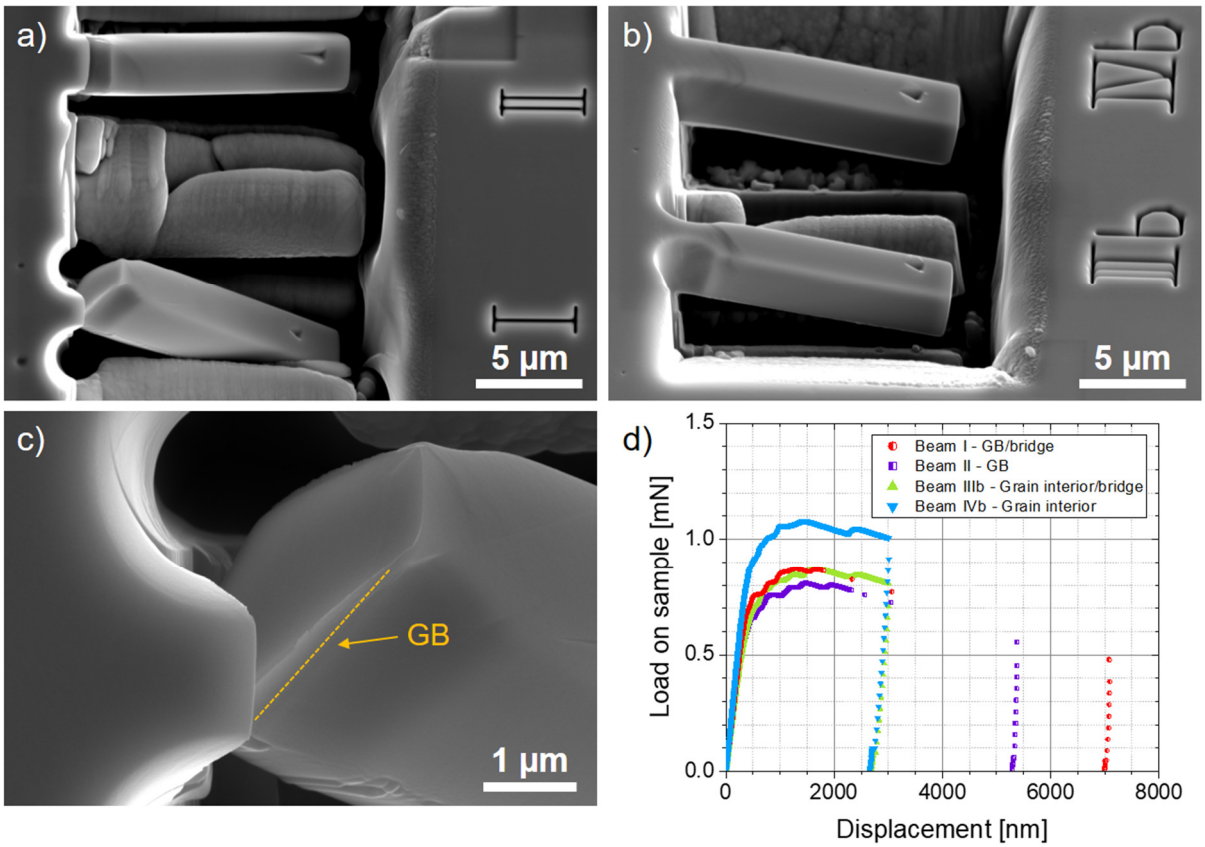

Fig. 5.37: a) Post-mortem *electron micrograph of un-notched bending beams. The beam in the bottom half of the image has a bridge cut to ensure fracture near or at the GB. b) Bending beams with the same geometry as depicted in (a) but in the grain interior. Fracture was not observed in this case. c) Detailed image of the fracture surface of the bridge cut beam at the GB. The GB was the starting point of fracture, however crack propagation seemingly diverted into the grain. d) Load as a function of displacement of the depicted beams.*

5.3.3. Potential of bending beams for grain boundary testing

Notched cantilevers are a standard sample geometry to extract fracture toughness values at the micro-scale. However, thorough validation of sample dimensions and deformation behavior is necessary. Since the samples are micro-sized, size effects and material constraints are also important factors to consider. During macroscopic testing Mo shows rather brittle behavior. However, extensive plastic deformation is observed during experiments on the micro-scale. Bending beams within the grains would not fracture without the introduction of a notch. Even the presence of a notch could not introduce stable crack propagation, which would lessen the stiffness of the cantilevers. To avoid preparation

artefacts, the introduction of a notch was omitted and several beams were fabricated with a bridge cut to ensure fracture at the GB. Bending beams with the same geometry were also fabricated in the grain interior. However, these beams did not fracture at all. The beams at GBs conversely showed fracture starting at the interface. The further crack propagation deviated into the grain interior. Considering this, the starting point of fracture could serve as an indication of the strength of the GB's cohesion. It is reasonable that differences in GB strength could be measured in this manner on the different material variants. However, influences of sample preparation by FIB milling and geometry might still be present.

5.4. Comparison of the different micromechanical testing methods

In the previous sections, the results of the different micromechanical testing methods were presented. All techniques have advantages and disadvantages and therefore their unique features and limitations.

Nanoindentation has the advantages of simple sample preparation and fast experimentation. The sample material has to be electro-polished after grinding to remove any possible deformation layer. After that, indentation arrays can be positioned with the LOM of the indenter platform. A slight grooving from electro-polishing helps to identify the position of GBs and does not interfere with the indentation data. The formation of deformation patterns is dependent on the crystal orientation and the indenter shape. The use of spherical nanoindentation circumvents the influence of the rotational position of a pyramidal indenter tip, such as a Berkovich indenter. Generally, a lot of imprints can be positioned at a GB. After measurement of the lengths between imprints and the GB, hardness as a function of distance to the interface can be plotted. Fitting the data with a Gauss peak function enables the extraction of parameters for the comparison between different boundaries. So far, the main influence on the hardness increase seems to be the extent of deformation pushed towards the interface. To compare the different material variants, grains with similar orientation and boundaries in the direction of the distinct deformation pattern should be selected. The inclination of these boundaries should ensure that the introduced deformation interacts with the interface and must not be varying between material variants. Beside the increase of hardness in proximity to the boundary, the release of piled-up dislocations in form of a GB pop-in might depend on the GB character [67]. The presence of doping elements could potentially influence the manifestation of this phenomenon and therefore it could be used to assess differences between technically pure and doped material. The use of indenters penetrating the sample surface leads to a complex stress and strain field underneath the indenter tip. Different slip systems are activated and cannot be distinguished from the top.

Micropillar experiments require the use of a FIB workstation to mill the desired geometry into electro-polished samples. The removal of the deformation layer is again important since the yield stress of the tested pillars depends on the presence or absence of dislocation sources. Additionally, the alignment between sample surfaces during fabrication

and testing of micropillars is important. The stochastic behavior of the mechanical response calls for testing of a batch of pillars with the same dimensions. This is space consuming since the surrounding material of each pillar must be removed to allow the loading with a flat-punch indenter. The main advantages of pillar experiments are the uniaxial loading condition and the study of slip phenomenon and slip transfer at GBs. Since the pillars are a freestanding sample volume, visualization from all directions is possible. However, the separation of the interface is not expected since no tension is enforced on the vertical boundary. The loading of the sample geometry is only possible in compression and is accommodated by slip activation. Since the yield stress is dependent on the presence of a dislocation source and the slip plane alignment, the comparison of slip transfer between pure and B-doped material requires ideally the same crystal orientations and inclination of slip planes towards the GB. However, due to the stochastic behavior the influence of impediment during slip transfer through a GB might be impossible to measure during pillar compression with reasonable numbers of pillars.

The fabrication of freestanding cantilevers entails even more effort during FIB preparation than pillar experiments. The sample volume has to be cut free underneath to allow the deformation of the beam. The fabrication of a sharp notch within 20 nm of the GB is essential for successful experiments. During the bending experiment, the top surface of the sample geometry experiences tension. The stress concentration at the FIB-notch leads to instable fracture directly at the notch after extensive plastic deformation of the beams. The desired separation of the GB was only reliably observed for un-notched samples since in this case the interface was the weak point of the specimen. The testing of cantilevers without a notch seems to be a possible testing method for GBs. The extensive plastic deformation is detrimental to calculate fracture toughness either way. Nevertheless, the amount of deformation until fracture might give a quantitative value of the interface's resistance against separation. The activation of slip systems on the top and bottom surface of the bending beams was observed. Depending on the alignment of slip planes in regard to the loading as well as the GB, dislocations may move towards the free surface, the neutral fiber or the GB. Dislocations leaving the sample at the free surface leave a crystal rotation in its wake, whereas the dislocations at the neutral fiber are the cause for the modified size-effect during micro-sized bending tests [100,101]. Only the dislocations impeded at the GB lead to a pile-up and an increased stress acting on the interface. Therefore, the crystallography might also play a non-negligible effect during this characterization technique. Regarding the comparison of

different material variants, the recording of deformation until fracture of bending beams seems to be a viable method, assuming the activation of slip systems is similar for the tested specimens.

6. Meso-scale bending of Mo grain boundaries

The results presented in the following sections have been partly published by the author in [129]. The numbering of figures as well as references was changed to fit the thesis.

6.1. Sample characterization and meso-scale bending experiments

The two material variants underwent the same thermo-mechanical procedure. The microstructures were analyzed by EBSD and are presented in Fig. 6.1. Even after recrystallization, the grains are elongated along the transverse and rolling direction, respectively, with aspect ratios between 0.43 and 0.54. The emerging grain sizes are displayed as equivalent diameters and were significantly smaller for the B-doped material (Fig. 6.1b and d) than for the pure samples (Fig. 6.1a and c). Pure Mo sheet and MoB plate samples show similar grain size and their texture is depicted as pole figure plots in their respective loading directions in Fig. 6.2.

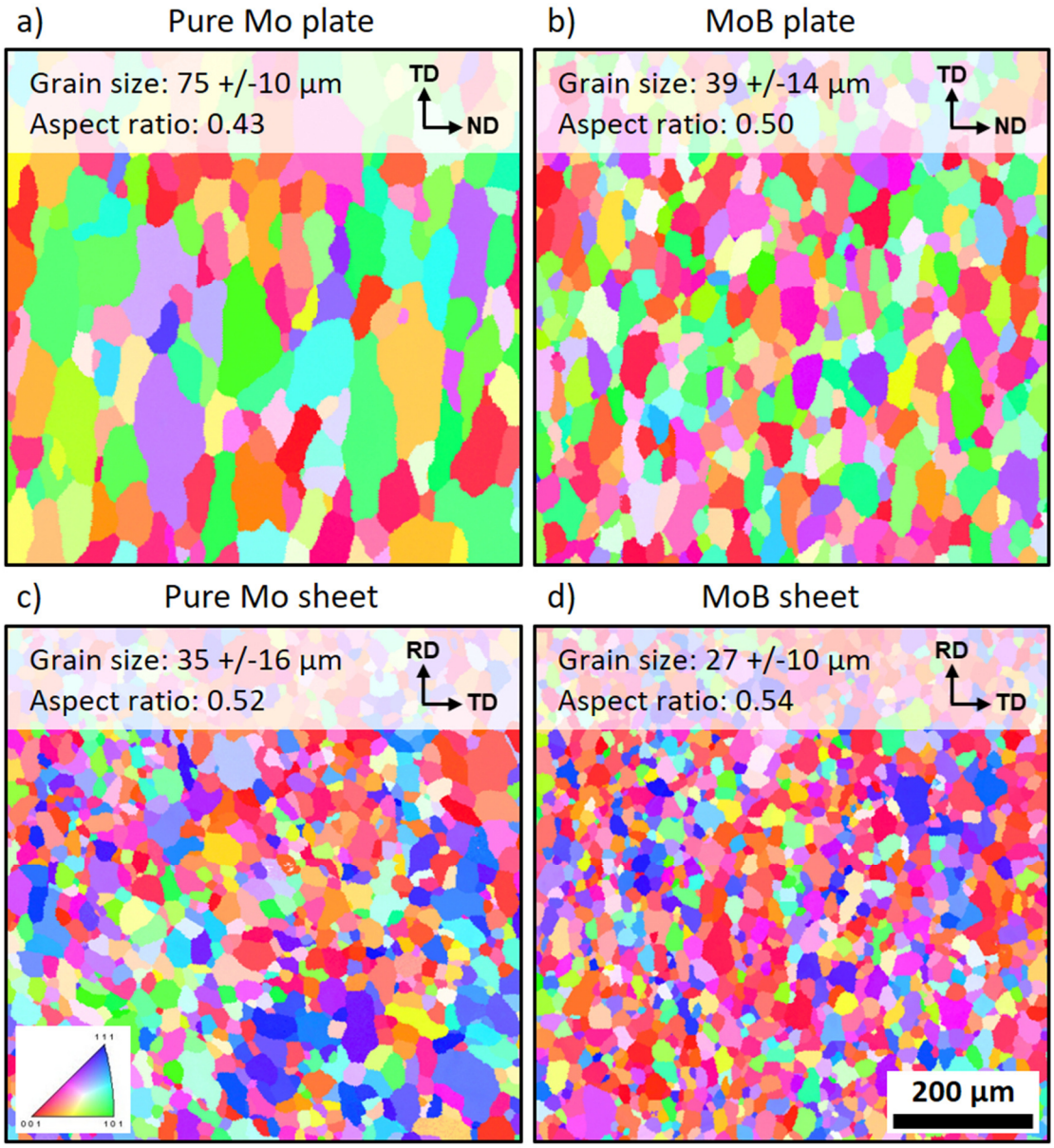

Fig. 6.1: Microstructures of the samples after rolling and recrystallization, depicted as IPF maps. The indicated grain sizes are calculated as equivalent diameters and the aspect ratios are displayed in the insets as well. The tensile loading direction on the extreme fiber during bending experiments is in the horizontal direction. RD…rolling direction, TD…transverse direction and ND…normal direction.

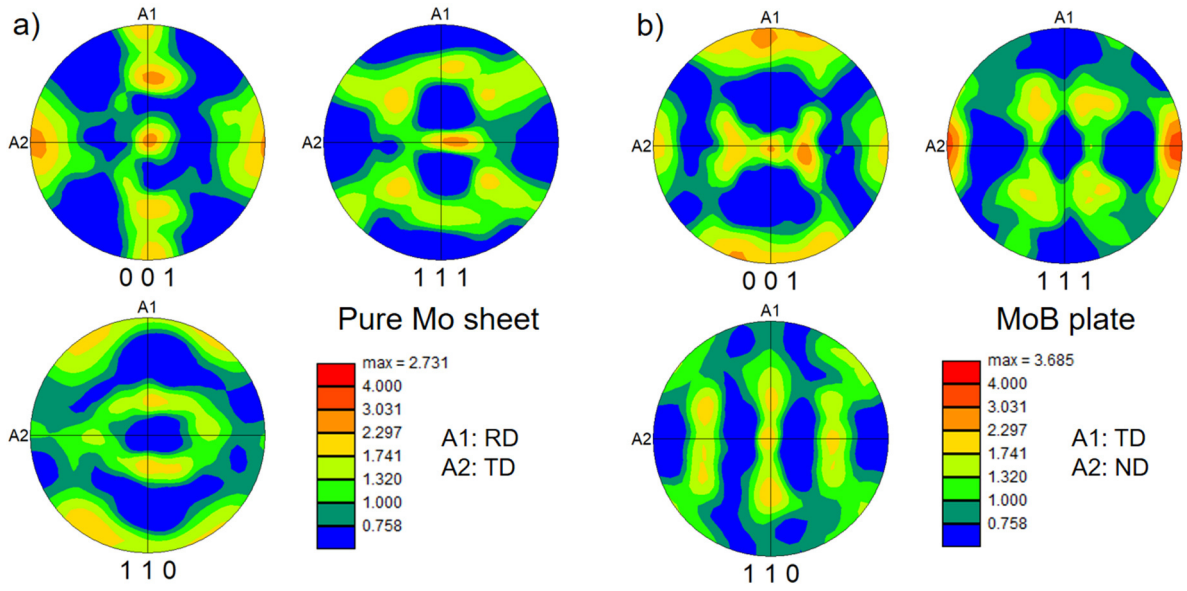

Fig. 6.2: Pole figure texture plots of the recrystallized microstructures of a) pure Mo sheet and b) MoB plate with the loading directions along A2. RD…rolling direction, TD…transverse direction and ND…normal direction.

Figure 6.3 displays the displacement of each specimen until failure during three-point-bending as a function of test temperature. Samples taken from the pure Mo plate have the largest grain size and show the lowest deformation until failure of the tested samples. At -20 °C fully brittle failure is observed. Samples made from MoB plate did not fracture during RT bending. At temperatures between 0 °C and -28 °C the failure mode varied between almost brittle fracture and no failure until the maximum bending displacement was reached. Even at -28 °C the MoB plate specimens do not indicate fully brittle fracture. For the pure Mo sheet the BDT can be clearly seen. Similar to MoB plate no samples fractured at RT. In contrast to that, brittle failure could be observed during bending at temperatures below -20 °C. Samples fabricated from MoB sheet, which have the smallest grain size, were deformed to the maximum displacement and did not break even at the lowest temperature of -28 °C. Therefore, these samples are not displayed in Fig. 6.3.

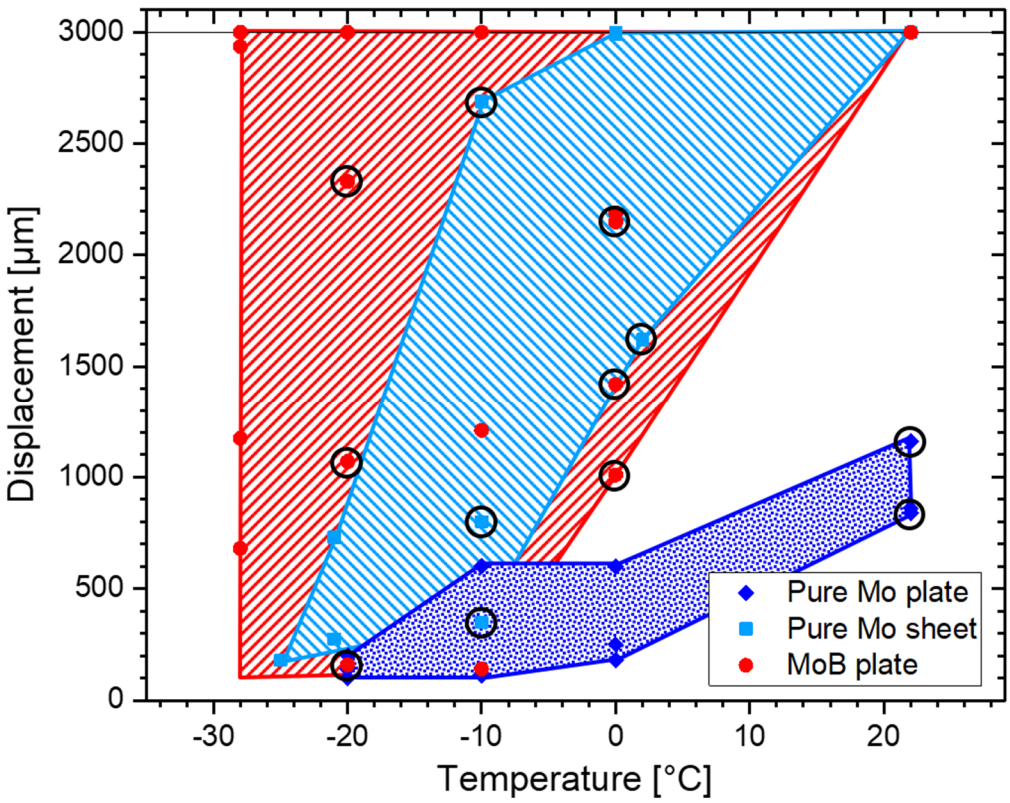

Fig. 6.3: Displacement until catastrophic failure during three-point-bending tests as a function of the test temperature for the different material variants. The shaded areas illustrate the scatter between different samples of the same material. Circular markings indicate samples used for further SEM analysis in section 6.3. Note that a displacement of 3000 µm corresponds to a bending angle of approximately 90°.

6.2. Crack tip opening angle

The separation of GBs can be envisioned similar to tearing adhesive tape from a flat surface, for instance a table. On one hand, if the tape has little cohesion the point of separation runs far from the pulled end and the angle between tape and table is small. On the other hand, if the tape is sticking firmly to the table, there is little separation and the enclosing angle is large. The hypothesis for GBs in Mo is that the average crack tip opening angle (CTOA) should reveal a tendency to higher angles for the doped material, since B enhances interface cohesion.

Table 8: Overview of samples for CTOA analysis.

Sample	Test temperature [°C]	Displacement till fracture [µm]	Analyzed area [mm²]
MoB-1	0	990	0.33
MoB-2	-20	1068	0.65
Mo-1	RT	836	0.70
Mo-2	RT	1145	0.44

Four samples, two of each plate material variant, with similar displacement until fracture were selected for CTOA analysis. The experimental details are shown in Table 8. To ensure reproducible results, a methodology for the evaluation was formalized and the application is exemplary shown in Fig. 6.4:

- The angle is measured between the crack tip and two points on the crack flanks.
- These points are defined at a distance of 1 µm from the crack tip.
- Separations shorter than 1 µm are therefore not included in the evaluation of CTOAs.
- Very small CTOAs are registered as ‘2°’ due to the resolution of the electron micrographs.
- The analysis is not applicable to grain separations ending at a triple point.

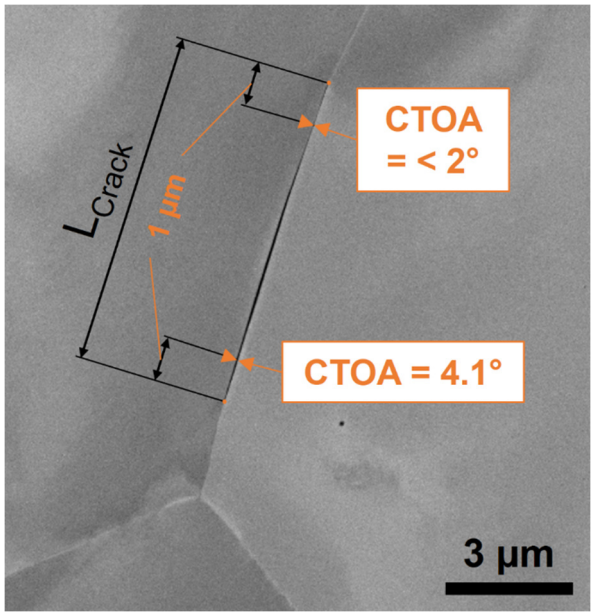

Fig. 6.4: Schematic representation of the measurement of CTOAs and crack length.

To study the subjective influence on the evaluation, two individual examiners analyzed the CTOAs of these four samples. Examiner 1 was the author of this thesis; examiner 2 was Thomas Weissenböck, at the time candidate for his Bachelor's degree.

Figure 6.5 depicts the relative cumulative frequency of CTOAs for the mentioned samples. The farther the data lies in the upper left corner, the smaller are the angles of grain separations. As mentioned above, the minimum angle is 2°, which is visible as the starting point for the data curves.

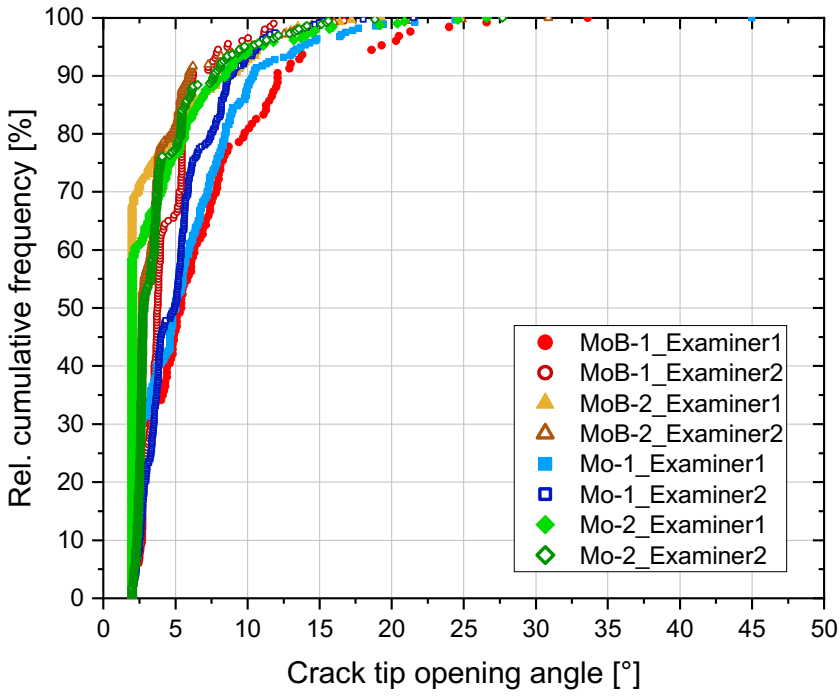

Fig. 6.5: Relative cumulative frequency of CTOAs of two samples each of pure Mo and MoB plate specimens. Each sample was investigated by two examiners.

To compare the results of the CTOA analysis, a bar diagram with the median angle for each sample and examiner is depicted in Fig 6.6. In addition, the error bars represent the crack tip angles at 30% and 70% cumulative frequency. The largest CTOAs are measured for sample MoB-1, followed by Mo-2. MoB-2 and Mo-1 reveal smaller CTOAs. There is a deviation between the analyses of the same electron micrographs by the different examiners. Especially for the two MoB samples, the results are not within the depicted error bars. Furthermore, the expected trend for larger CTOAs in the doped material could not be assessed within the presented study.

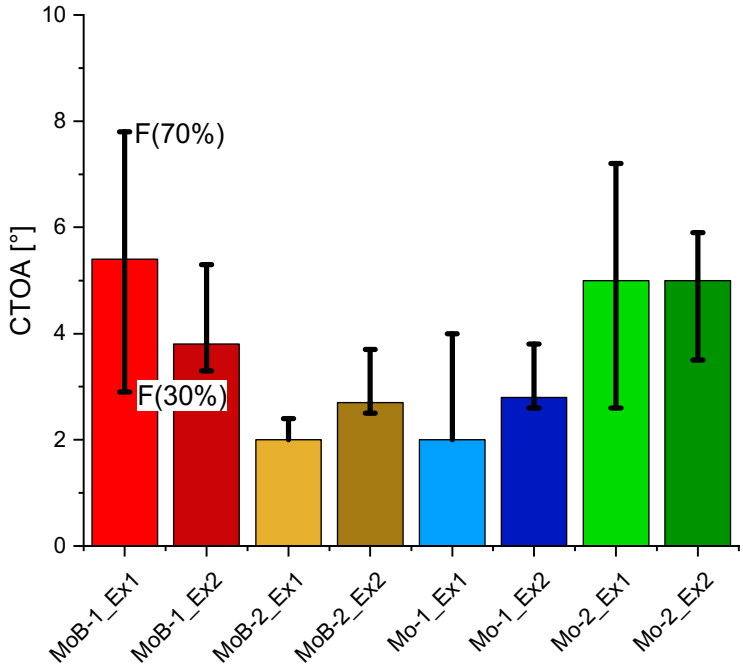

Fig. 6.6: Bar diagram of the median CTOA measured for each sample and examiner. The error bars represent the CTOA at 30% and 70% cumulative frequency.

6.3. Relative length of open grain boundaries

The marked samples in Fig. 6.3 were chosen for *post-mortem* investigation with SEM micrographs since they cover a wide range of maximum deformation at the same test temperature. An area of the tension-loaded top surface near the final fracture plane was imaged in backscattered electron contrast. Using the implemented panorama function of the SEM a relatively large area between 0.33 and 1.2 mm² for the different samples was investigated. On the single micrographs, the length of the occurring GB cracks was measured with the image processing software ImageJ. In order to put the length of separated GBs into perspective with the microstructure, EBSD measurements were used to capture and determine the total GB length. After calculation of the specific GB length per sample area for the different material states, the total length of interfaces on the SEM imaged area could be extrapolated and compared to the occurring crack length. Subsequently, the relative proportions of separated GBs for the 12 investigated samples were calculated and are depicted in Fig. 6.7 as a function of displacement during bending. As expected, the general

trend for all material conditions is a higher proportion of separated GBs for samples, which endured more deformation before final fracture. The two samples of pure Mo plate, deformed at RT, display 9.6% and 11.9% open GB length after 836 µm and 1145 µm displacement, respectively. The investigated samples from pure Mo sheet display an increasing proportion of separated GBs up to 15.4% for the sample failing after 2687 µm displacement during bending. The MoB plate specimens display the same trend in increased proportion of separated interfaces with higher deformation up to a maximum of 5.1% of open GBs. The two samples with highest displacement until failure of this material variant were unloaded after a significant load drop in the test record, indicating significant crack propagation in the microstructure. All other bending tests ended by a catastrophic failure of the samples.

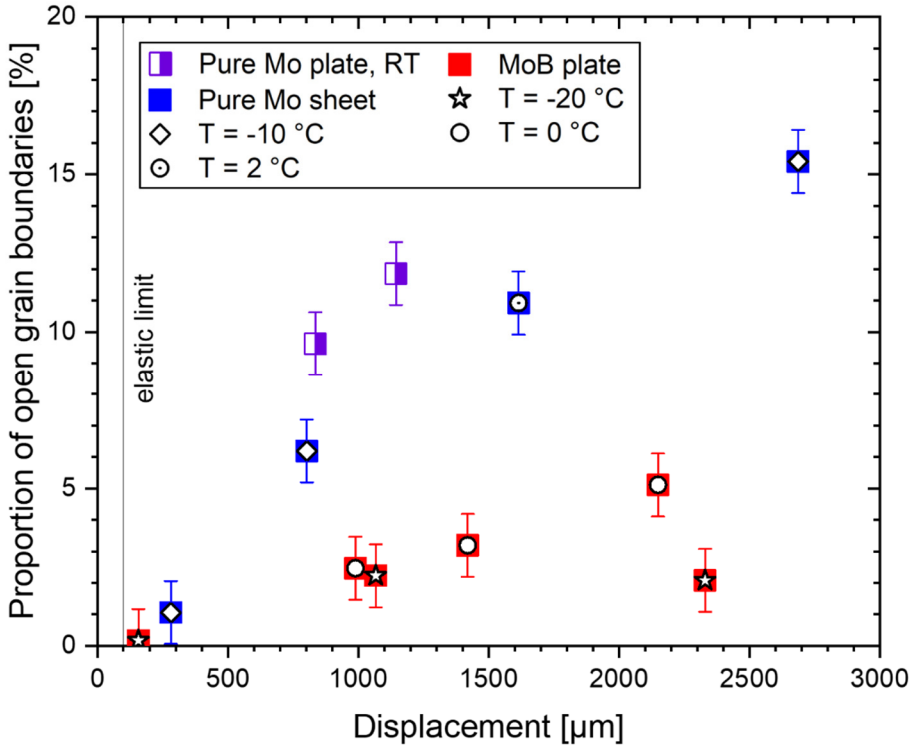

Fig. 6.7: Proportion of separated GBs in regard to the extrapolated total GB length of the investigated sample area as a function of displacement during bending. The MoB samples show a decreased proportion of GB crack length (see text).

Beside intercrystalline separations, the length of transcrystalline fracture was recorded. The crack length was again related to the specific GB length as described above and is depicted in Fig. 6.8. The bars are grouped by material variant and labelled according to their

displacement until fracture. The samples of MoB plate material show higher proportion of transcrystalline separations compared to pure Mo specimens. The two samples with high deformation till fracture, cross-hatched in Fig. 6.8, experienced a significant load drop and were unloaded subsequently. These two samples depict significantly less proportion of transcrystalline cracks. The occurrence of large amounts of transcrystalline separation is apparently linked to the catastrophic failure of the samples. The test temperature has also an influence, since samples tested at -20°C depict on average 1.6% transcrystalline crack length, whereas the samples tested at 0°C only display half as much relative crack length on average.

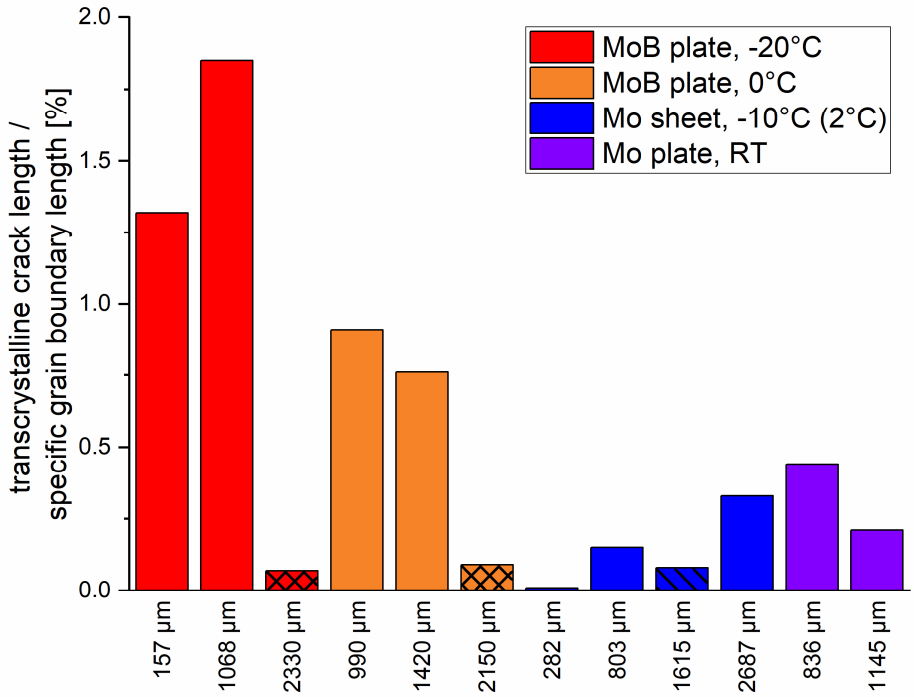

Fig. 6.8: Bar diagram of transcrystalline crack lengths in relation to the specific GB length per sample area. The cross-hatched bars indicate samples showing significant load drop and were subsequently unloaded. The simple hatched bar for Mo sheet material was tested at 2°C as opposed to -10°C for the rest of the Mo sheet specimens.

6.4. Number of available slip system pairs

To examine the propensity of GBs to damage initiation, one sample of the least ductile variant was selected for in-depth investigation. Prior to the bending experiment an EBSD scan

was performed on the pure Mo plate sample with 836 µm displacement until fracture (see Fig. 6.9a). Additionally, Fig. 6.9b displays one SEM panorama *post-mortem* image. After bending, the occurring GB cracks (exemplary indicated in Fig. 6.9c) were correlated with the orientations of the adjacent grains. In this way, a dataset with grain orientations of 70 separated interfaces and 540 intact GBs was deduced.

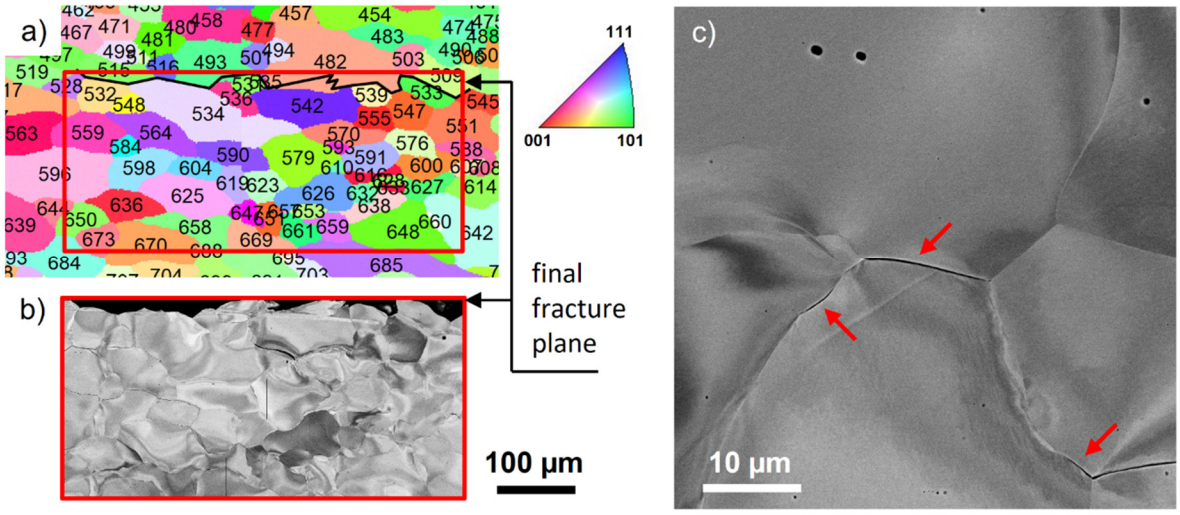

Fig. 6.9: Pure Mo plate - exemplarily: a) Selected section of the EBSD scan of a sample prior to bending. The final fracture plane and the frame of the SEM panorama is indicated. b) Corresponding SEM panorama image consisting of 50 single micrographs. c) Example of a single SEM image with 50 nm/pixel resolution. Occurring GB cracks are indicated by arrows.

This dataset with intact and open GBs was used to analyze the impact of grain orientations on occurring separations. The distribution of GB misorientations is close to a random distribution. This is expected since during recrystallization the deformation texture is significantly weakened. Fig. 6.10 displays the relative number of appearing cracks in regard to the sum of all GBs for the different misorientation classes. The absolute number of cracks is specified above the respective bars. This diagram reveals two distinct plateaus. Up to a misorientation of 30° only a small relative number of GBs separated. However, GBs with a misorientation of 30° or more display a significant higher occurrence of cracks. Considering the absolute number of cracks, over 90 % of the occurring separations fall under the latter condition.

Using MATLAB and the MTEX Toolbox, a script was written to analyze the potential of slip transfer at the GBs. It is known that only at interfaces with favorable aligned slip systems transmission of dislocations and subsequently a co-deformation of the two adjacent grains is possible. One simple parameter to investigate potential slip transmission is $m' = cos(\psi)cos(\kappa)$, introduced by Luster and Morris [119]. The angles ψ and κ correspond to the angles between slip directions and slip plane normals, respectively. Slip transfer is believed to be possible for m' values larger than about 0.85 as reported by micropillar experiments as well as matching slip lines in adjacent grains in macro-scale samples [94,95,127,168]. The MTEX Toolbox uses the <111>{1-10} and <111>{11-2} slip systems for bcc crystals. Therefore, every grain orientation has 24 possible slip systems counting one Burgers vector direction only. Considering this, a maximum of 576 slip system pairs between two grain orientations exist. The MATLAB script compares every slip system of one grain to the slip systems of the adjacent grain and calculates the m' parameter. A requirement of $m' > 0.85$ was set and the number of slip system pairs fulfilling this requirement was counted. Fig. 6.10 depicts these numbers of potential slip transmission pairs as a function of misorientation. The GB with the lowest misorientation of 5.9° has 58 slip system pairs which fulfill the condition $m' > 0.85$. With increasing misorientation the number of potential slip system pairs decrease to a maximum of 17 for misorientation of 30° or higher. This observation coincides well with the observed GB cracks.

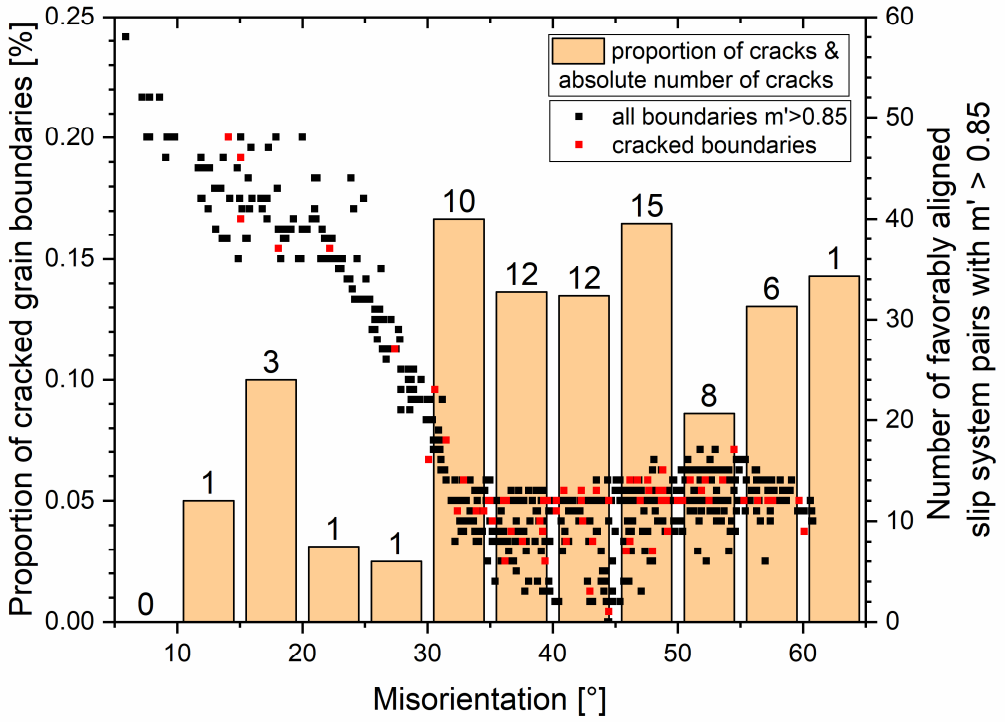

Fig. 6.10: Relative number of GB cracks in proportion to the sum of GBs for the different misorientation classes and number of favorable aligned slip system pairs as a function of misorientation for one sample of the pure Mo plate. The absolute number of cracks for a given misorientation class is indicated above the respective bar. The criterion for potential slip transmission is m‘ *> 0.85 (see text).*

6.5. On the influences during meso-scale bending

During the conducted bending experiment, the sample deforms elastically before the onset of plasticity is taking place. Upon reaching the local critical resolved shear stress, dislocation sources within the grains or at the GBs are activated. Either way, the first dislocations are emitted as a cascade of evenly aligned dislocations into the grain. The dislocations are impeded at the GBs, causing a rotation of the grain and a back-stress on the following dislocations. To compensate the local geometry change, further slip systems are activated by the dislocation pile-up at the interface [169]. If the GB is per chance aligned in a way to favor slip transmission, transfer of dislocations into the neighboring grain is possible

and the local stress at the boundary should not rise. This strongly depends on the grain orientations as well as the inclination of the GB and the direction of the locally applied load [122,170]. Another possibility is the activation of a dislocation source near the boundary in the adjacent grain [171]. With slip transmission or deformation in the adjacent grain, the strain impeding on the GB can be relaxed and compatibility of both grains is realized [77,172]. In contrast to that, a GB can be resistant to slip transfer. This is arguably the more prominent case for GBs and for the investigated material states in this study. With increasing deformation during the bending experiment, more and more dislocations are pushed towards the GBs. If the resulting stress of the accumulated dislocations exceeds the cohesive strength of the GB before additional slip systems are activated, the boundary separates resulting in a GB crack [173–175].

How many GB open up before the critical size is reached should give a quantitative value for the interfaces' cohesive strength. This comparison is only valid as long as similar microstructures are investigated. The extent of dislocation pile-up depends on the grain size. Furthermore, the grain size influences the crack growth since the boundaries can lead to geometrical shielding effects of the crack tip by crack deflection or arrest at triple points. For a more detailed analysis of the interplay between grain size and fracture toughness, see [176]. A study on the refractory metal W reports the influence of grain size on the BDTT [177]. Similarly, the samples of the different mill product formats in this study display different BDTTs. The pure Mo plate material has the largest mean grain size, as shown in Fig. 6.1, and fails with only little deformation at RT. In contrast to that, the samples made from MoB sheet have the smallest grain size and did not fracture even at -28 °C. However, the difference of mean grain size between pure Mo sheet (35 +/-16 µm) and MoB plate (39 +/-14 µm) is negligible. Another influence might be the texture after thermo-mechanical processing. Fig. 6.2 shows the texture plots in the respective loading directions. Especially the (111) and (110) pole figure plots are different between plate and sheet format. However, texture should only be a minor influence, since the samples are in the recrystallized state for the bending experiments. Furthermore, only the intercrystalline separations are of interest in this study and the misorientation distribution is in both cases similar to a random distribution.

The test temperature might also play an important role for the appearance of cracks. The two compared material variants used for analysis of relative open GB length showed predominant ductile behavior at RT. The bending series of the pure Mo sheet material reached

brittle fracture at -20 °C, whereas for MoB plate all samples exhibited a larger variance even at -28 °C and did not reach fully brittle fracture for the investigated temperature range. The amount of cracked boundaries was investigated for different maximum displacements. The results for pure Mo sheet show a congruent trend of increased separations even though one experiment was carried out at 2 °C, compared to -10 °C for the other three analyses. The two experiments on MoB plate with the highest deformation were unloaded after a significant load drop as opposed to instable crack growth. This means that the amount of open boundaries might be underestimated. In contrast to these two samples, the other specimens made from MoB plate show a considerable amount of transcrystalline cracks, suggesting that the majority of transcrystalline fracture happens during catastrophic failure of the sample. The samples tested at 0 °C showed about half as much crack length inside the grains, when compared to the specimens tested at -20 °C, which can be attributed to the reduced dislocation mobility at lower temperatures.

The GB strength depends inherently on the atomic bonds and therefore on the chemical composition and atomic arrangement of the interface. Closely packed boundaries, which are equivalent with a low misorientation, have a higher bonding strength [6,178]. The display of relative number of cracks on available GBs for a given misorientation class (Fig. 6.10) gives the propensity of GB character for separation. The distinct differentiation at 30° misorientation incidents with the available slip systems for potential dislocation transfer [126,179]. Note, that for this calculation only the grain orientations available via EBSD were used. This means that a quick analysis of the microstructure can already give information about the propensity towards GB cracks without tedious analysis of GB inclination or local stress state. GBs with high misorientation have generally an atomic arrangement with higher spatial distances at the interface, i.e. the atoms are more loosely positioned. The geometrical considerations of slip transfer as a function of misorientation are not only valid for pure Mo plate, as exemplarily displayed in Fig. 6.10, but are broader applicable. The MATLAB script was also used on an EBSD dataset of pure Mo sheet material and the resulting number of favorable aligned slip systems follows the presented dependence on misorientation in a rather narrow corridor. The number of available slip system pairs would be similarly distributed for the MoB material since the misorientation distribution is equivalent. However, the number of occurring GB cracks would be reduced in accordance with the measured GB crack length displayed in Fig. 6.7.

Looking at the chemical composition at the interface, impurities diffuse to the GB since the atomic spacing allows for less overall displacement and energy expense. The specification of technically pure Mo still includes impurities in the range of µg/g. Typical elements are O, N and P [32,166]. Especially O has a detrimental effect on the cohesion of the GBs. P is also reported to have a detrimental effect, whereas N is described as somewhat inert or slightly detrimental. Other elements like B and C are identified as beneficial for the GB cohesion. The strong segregation tendency of B is already shown in literature via simulations and APT [9,30,180]. One GB of pure Mo sheet with 43° misorientation as well as one boundary with 36° misorientation of B-doped plate material were prepared for APT measurement employing the lift-out technique. It seems, that the segregation content in recrystallized samples is influenced by the overall chemical composition and the available GB area as well as the prevailing atomic arrangement [32]. The analyzed GBs should represent typical GBs in the materials since coincidence lattice site boundaries were avoided. One representative measurement of the GB of MoB plate is presented in Fig. 6.11. The atomic reconstruction in Fig. 6.11a shows the decoration of the GB with B atoms. From the concentration profiles (Fig. 6.11b and c) the IFE values are calculated and the quantified amounts of GB segregations are depicted in Table 9. The values are averaged between three successful measurements in case of the MoB sample. In the case of the pure Mo specimen, only one APT measurement could be conducted with a GB in the analyzed volume. The experimental results obtained in this study are compared to IFE values in literature, see Table 9. Not surprisingly, B was not found in pure Mo samples. Only when added to the material, IFE values larger than zero can be detected. The presence of C in pure Mo is significantly lower, however, both materials display amounts comparable to IFE values reported in literature for recrystallized Mo. Larger amounts of C are present at Σ-boundaries [32] or if C is added to the material [9]. The excess amounts of O and N are similar in pure and B-doped material. In the case of O, the IFE values are even less than reported in literature, whereas N is within reported ranges. P is more prominent in the pure sample compared to MoB, with both values lying near the lower end of expected ranges. The amount of the derived IFE also depend on the available GB area as reported in [32]. The grain size in this work is smaller than that reported for recrystallized samples [32] and only slightly higher compared to that present in sintered materials [9].

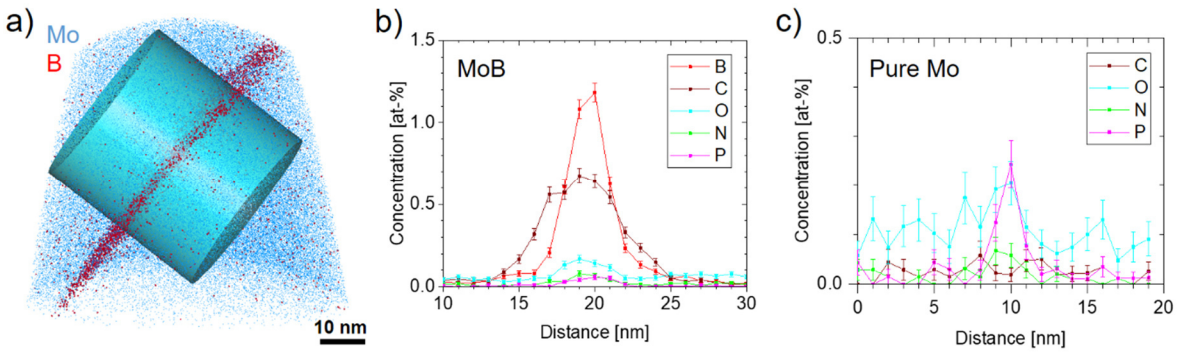

Fig. 6.11: a) APT reconstruction of a tip containing a GB with 36° misorientation in B-doped plate material. The red dots represent B atoms. b) Concentration profiles of accompanying elements along the cylindrical region of interest, depicted in (a). c) Concentration profiles of impurity elements in the measured GB of pure Mo sheet material. Note the different scale of the concentration axes.

Table 9: IFE values of accompanying elements at GBs of pure Mo sheet and MoB plate material as well as experimental values from literature.

Element	**Interfacial excess [atoms/nm²]**				
	Pure Mo, this study	**MoB, this study**	**Recrystallized Mo (no Σ-GBs)** [32,166]	**Sintered MoC** [9]	**Sintered MoB** [9]
B	0	2.5	0	0	10.42
C	0.05	2.3	0.01 – 2.2	6.54	0.91
O	0.18	0.20	0.35 – 2.0	0.49	0
N	0.11	0.12	0.03 – 3.0		
P	0.35	0.13	0.15 – 1.5		

The final fracture surfaces of the bending samples show intercrystalline fracture for pure Mo and transgranular fracture for MoB material. This qualitative improvement of the GB cohesion was already reported in literature [9,10,34]. However, the crack initiation is not apparent on the final fracture surface. To gain insight on this damage nucleation, the bending

samples were imaged *post-mortem* on the tension-loaded top surface near the fracture plane. The occurrence of GB cracks on both material variants, with and without B additions, is evidence that cracks first appear at GBs. Further, these initial cracks do not extend to the critical defect size for instable crack growth. Therefore, more GBs separate at positions with unfavorable strain accumulation and existing cracks increase in length. When the first crack reaches the critical size, instable crack growth in either inter- or transgranular manner lead to the observed catastrophic fracture of the sample.

From this work, it is clear that the segregations introduced by means of B-doping of technically pure Mo lead to enhanced cohesion of the GBs. The beneficial effect is evident in the proportion of separated GB length on samples with similar microstructure, as can be seen in Fig. 6.7. The relative amount of open GB length at similar displacement during bending is reduced to one third on samples from MoB plate when compared to pure Mo sheet. This drastic impact is apparent without any significant microstructural differences, such as different grain size or pronounced texture, between these two material variants.

6.6. Up-scaling of the meso-scale analysis method

The relative length of cracks on the tension-loaded surface revealed to be an effective method to distinguish between the cohesion-enhanced material variant MoB and technically pure Mo. So far, the bending experiments were performed on a K&W bending apparatus with rather slow deformation speed. To investigate the application of this analysis method in industrial-scale quality control, bending samples with dimensions of 36 x 10 x 1.5 mm^3 were prepared in the TD from sheet material and electro-polished on one side following the manner of experiments described above. The specimens were deformed at the industrial partner with 10 mm/min deformation speed. This corresponds to 167 µm/s compared to 5 µm/s for the lab-scale experiments. The experiments were conducted on a bending device with 20 mm bearing distance at temperatures between -40°C and 0°C. Two samples from each material variant with different bending angle at fracture were selected for the study of open GBs. Note that the samples have different grain size (Mo sheet has 35 µm and MoB sheet 27 µm equivalent diameter). Therefore, the specific GB length per sample area is different, namely $8.54 \cdot 10^4$ µm/mm² for Mo compared to $1.54 \cdot 10^5$ µm/mm² for MoB sheet material. The

examined samples were deformed at test temperatures between -30°C and -10°C and an area of 0.46 to 0.5 mm² each were investigated for GB delaminations.

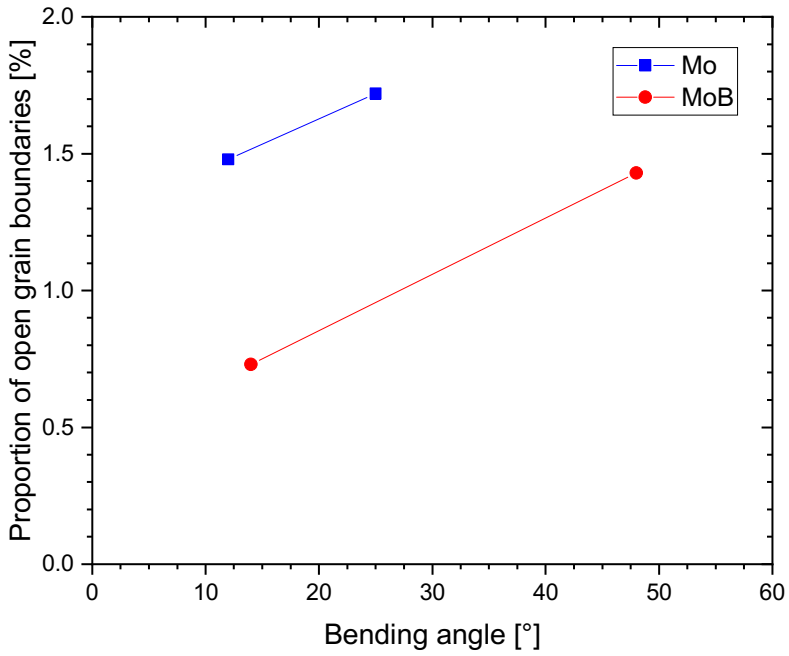

Fig. 6.12: Proportions of delaminated GBs during industrial-scale quality control.

Figure 6.12 depicts the relative proportion of delaminated GBs as a function of bending angle. For both material variants, a trend to more separated GBs with increased deformation is apparent. The MoB samples experienced less separations as was expected from lab-scale experiments. The amount of open GBs is significantly lower than previous investigations as illustrated in Fig. 6.7, namely by a factor between 3 and 5 at similar bending angles. The reason for this might be the higher deformation speed, since dislocation movement is reduced and fracture more favored. Another important impact is the microstructure. The texture is in this case similar since both samples were prepared from sheet material. However, the grain size in the MoB sample is smaller than for the Mo sample and therefore the specific grain boundary length per area is different. Looking at the crack lengths in relation to the examined area, a smaller discrepancy between technically pure and micro-doped Mo is observed. This illustrates the need to assess the similarity of the investigated microstructures.

7. Conclusion & Outlook

Within this thesis, different micromechanical testing methods were performed at or near GBs to elucidate the mechanical response of these interfaces. Furthermore, the crack initiation on the tensile extreme fiber of mm-sized bending samples was examined and the GBs propensity to decohesion was investigated. Additionally, the chemistry of GBs during recrystallization was investigated by APT experiments on semi-recrystallized samples and diffusion considerations.

Arrays of indentations with pyramidal and spherical indenter geometry were placed across different GBs with a nanoindenter using CSM to continuously record hardness and modulus data. The hardness deviation was examined and related to the crystallographic disposition of the indented grain and the indenter geometry as well as its alignment. It became clear that the grain orientation in combination with the rotation angle of a pyramidal indenter, like a Berkovich tip, has a decisive influence on the measured hardness increase near the GBs. The faces of the indenter can enhance deformation along [111] directions, which lie almost parallel to the sample surface and vice-versa the vertices can impede excessive deformation. During the indentation with spherical indenters, the rotation of the tip can be omitted as an influencing parameter. Generally, only if deformation is pushed towards the boundary, dislocations can interact with the boundary and result in a deviating hardness measurement. This hardness increase is within measurement uncertainty independent from the orientation of the neighboring grain or the misorientation of the interface.

Pillar compression experiments are useful to investigate the activation of slip systems and the transfer of slip across GBs. The combination of high Schmid-factor and close geometrical alignment is necessary for the transmission of slip deformation. The favorable alignment of slip planes and directions seems to be a precondition for slip transfer. The yield behavior of pillar specimens follows the stochastic behavior for micro-sized samples. The comparison of pillars on the different material variants could therefore not be assessed with reasonable number of samples. The search for virtually ident orientation pairs in both material variant is cumbersome and does not reveal distinct differences. The deformation behavior of pillars is predominantly dependent on the individual grain orientations and the loading does not lead to decohesion of the GB in bi-crystalline samples.

Micro-sized bending beams offer the possibility of tensile loading of at least parts of the GB. The material Mo is rather brittle during macroscopic testing. However, in the size regime of micrometers, extensive plastic deformation is observed. Bending beams with a fabricated notch are a common geometry for micro-sized measurement of the fracture toughness. Experiments proved that the position of the notch is the starting point of fracture and only if the GB is within 10 to 20 nm, fracture of the interface is expected. To avoid problems during notch preparation and interpretational errors due to the plastic deformation, bending beams without such a predetermined weak spot were fabricated. The GBs served as starting point for the failure of the beams in straight and bridge-shaped specimens. The characterization of the endured deformation before fracture seems to be a possible analysis method for the cohesion of GBs. The appearance of slip lines indicate that the predisposition of grain orientations might still have a non-negligible influence on the fracture behavior.

Besides the micromechanical testing of individual GBs, mm-sized bending samples were deformed. The sample surface of the tensile loaded extreme fiber was imaged *post-mortem* by electron microscopy. The appearance of delaminated GBs on both material variants is evidence that crack initiation occurs at the boundaries. Literature revealed fractographs to be a qualitative indication for better GB cohesion in B-doped Mo samples. In the new approach, discussed in this thesis, the length of open GBs on the tensile-loaded sample surface is related to the specific GB length per sample area. In this manner, the cohesion enhancing impact of B at the GBs could be demonstrated in a quantitative fashion. The proportion of delaminated GBs in MoB plate material is reduced to one third compared to technically pure Mo sheet. Both samples have similar microstructure and therefore the reduction in delaminated interfaces can be attributed to the segregation of B and C at the GBs, as measured by APT.

Additionally, the propensity of GBs for separation was investigated by the tendency to allow slip transfer. The slip systems of adjacent grains with matching alignment, identified by an *m'*-parameter > 0.85, were counted and plotted as a function of misorientation. The occurrence of cracks matches the reduced number of favorable aligned slip system pairs for GBs with a misorientation of 30° or higher. This evaluation method uses only the grain orientations as input and can therefore be performed on any EBSD scan in a simple manner.

The new meso-scale testing uses only methods that are broadly available and therefore easily applicable. Furthermore, the described method offers further promising

potential for automation, since panorama image capture and greyscale crack detection are already applied or feasible during examination.

In conclusion, this work could show possible applications and their limitations of micromechanical testing geometries employed on Mo samples from industrial production. The newly described method of meso-scale bending experiments offers a viable way to quantitatively measure the impact of B micro-doping in technically pure Mo. Therefore, the methodology allows the assessment of different segregation engineering concepts for further optimization.

References

[1] W. Martienssen, H. Warlimont, eds., Springer Handbook of Condensed Matter and Materials Data, Springer Berlin Heidelberg, 2005.

[2] J.A. Shields, ed., Applications of Molybdenum Metal and its Alloys, Second edi, International Molybdenum Association (IMOA), London, UK, 2013.

[3] E. Pink, R. Eck, Refractory metals and their alloys, in: R.W. Cahn, P. Haasen, E.J. Kramer (Eds.), Mater. Sci. Technol., Wiley-VCH Verlag GmbH & Co. KGaA, Weinheim, Germany, 2006. https://doi.org/10.1002/9783527603978.mst0088.

[4] B. V. Cockeram, The role of stress state on the fracture toughness and toughening mechanisms of wrought molybdenum and molybdenum alloys, Mater. Sci. Eng. A. 528 (2010) 288–308. doi:10.1016/j.msea.2010.09.009.

[5] K. Babinsky, S. Primig, W. Knabl, A. Lorich, R. Stickler, H. Clemens, Fracture Behavior and Delamination Toughening of Molybdenum in Charpy Impact Tests, J. Miner. Met. Mater. Socienty. 68 (2016) 2854–2863. doi:10.1007/s11837-016-2075-y.

[6] D. Scheiber, R. Pippan, P. Puschnig, L. Romaner, Ab initio calculations of grain boundaries in bcc metals, Model. Simul. Mater. Sci. Eng. 24 (2016) 35013. doi:10.1088/0965-0393/24/3/035013.

[7] J.B. Brosse, R. Fillit, M. Biscondi, Intrinsic intergranular brittleness of molybdenum, Scr. Metall. 15 (1981) 619–623. doi:10.1016/0036-9748(81)90038-7.

[8] A. Kumar, B.L. Eyre, Grain Boundary Segregation and Intergranular Fracture in Molybdenum, Proc. R. Soc. A. 370 (1980) 431–458. doi:10.1098/rspa.1980.0043.

[9] K. Leitner (née Babinsky), D. Lutz, W. Knabl, M. Eidenberger-Schober, K. Huber, A. Lorich, H. Clemens, V. Maier-Kiener, Grain boundary segregation engineering in as-sintered molybdenum for improved ductility, Scr. Mater. 156 (2018) 60–63. doi:10.1016/j.scriptamat.2018.07.008.

[10] K. Leitner, D. Scheiber, S. Jakob, S. Primig, H. Clemens, E. Povoden-Karadeniz, L. Romaner, How grain boundary chemistry controls the fracture mode of molybdenum, Mater. Des. 142 (2018) 36–43. doi:10.1016/j.matdes.2018.01.012.

[11] S. Primig, H. Leitner, H. Clemens, A. Lorich, W. Knabl, R. Stickler, On the recrystallization

behavior of technically pure molybdenum, Int. J. Refract. Met. Hard Mater. 28 (2010) 703–708. doi:10.1016/j.ijrmhm.2010.03.006.

[12] H. Kimura, Overview, Intergranular Fracture in BBC metals, Trans. Japan Inst. Met. 29 (1988) 521–539. http://www.jim.or.jp/journal/e/pdf3/29/07/521.pdf.

[13] B. V. Cockeram, E.K. Ohriner, T.S. Byun, M.K. Miller, L.L. Snead, Weldable ductile molybdenum alloy development, J. Nucl. Mater. 382 (2008) 229–241. doi:10.1016/j.jnucmat.2008.08.021.

[14] R. Eck, The State-of-the-Art of Molybdenum Fabrication, Ceram. Eng. Sci. Proc. 6 (1985).

[15] Plansee SE, (n.d.). https://www.plansee.com (accessed June 21, 2021).

[16] B. V. Cockeram, The mechanical properties and fracture mechanisms of wrought low carbon arc cast (LCAC), molybdenum-0.5pct titanium-0.1pct zirconium (TZM), and oxide dispersion strengthened (ODS) molybdenum flat products, Mater. Sci. Eng. A. 418 (2006) 120–136. doi:10.1016/j.msea.2005.11.030.

[17] B. V. Cockeram, K.S. Chan, In-situ fracture studies and modeling of the toughening mechanism present in wrought low-carbon arc-cast molybdenum, titanium-zirconium-molybdenum, and oxide-dispersion-strengthened molybdenum flat products, Metall. Mater. Trans. A Phys. Metall. Mater. Sci. 39 (2008) 2045–2067. doi:10.1007/s11661-008-9561-y.

[18] H. Kurishita, A. Ôishi, H. Kubo, H. Yoshinaga, Grain Boundary Fracture in Molybdenum Bicrystals with Various <110> Symmetric Tilt Boundaries, Trans. Japan Inst. Met. 26 (1985) 341–352. doi:10.2320/matertrans1960.26.341.

[19] S. Tsurekawa, T. Tanaka, H. Yoshinaga, Grain boundary structure, energy and strength in molybdenum, Mater. Sci. Eng. A. 176 (1994) 341–348. doi:10.1016/0921-5093(94)90997-0.

[20] S. Tsurekawa, S. Kokubun, T. Watanabe, Effect of grain boundary microstructures of brittle fracture in polycrystalline molybdenum, Mater. Sci. Forum. 304–306 (1999) 687–692. doi:10.4028/www.scientific.net/msf.304-306.687.

[21] T. Watanabe, S. Tsurekawa, Control of brittleness and development of desirable mechanical properties in polycrystalline systems by grain boundary engineering, Acta Mater. 47 (1999) 4171–4185. doi:10.1016/S1359-6454(99)00275-X.

[22] L.C. Lim, T. Watanabe, Fracture toughness and brittle-ductile transition controlled by grain boundary character distribution (GBCD) in polycrystals, Acta Metall. Mater. 38 (1990) 2507–2516. doi:10.1016/0956-7151(90)90262-F.

[23] T. Watanabe, Grain boundary engineering: Historical perspective and future prospects, J. Mater. Sci. 46 (2011) 4095–4115. doi:10.1007/s10853-011-5393-z.

[24] D. Raabe, M. Herbig, S. Sandlöbes, Y. Li, D. Tytko, M. Kuzmina, D. Ponge, P.P. Choi, Grain boundary segregation engineering in metallic alloys: A pathway to the design of interfaces, Curr. Opin. Solid State Mater. Sci. 18 (2014) 253–261. doi:10.1016/j.cossms.2014.06.002.

[25] A. Fraczkiewicz, K. Wolski, Intergranular Segregation and Crystalline Material Fracture, in: L. Priester (Ed.), Grain Boundaries Crytalline Plast., John Wiley & Sons, Inc, Hoboken, NJ, USA, 2011: pp. 281–321.

[26] P. Lejček, M. Šob, V. Paidar, Interfacial segregation and grain boundary embrittlement: An overview and critical assessment of experimental data and calculated results, Prog. Mater. Sci. 87 (2017) 83–139. doi:10.1016/j.pmatsci.2016.11.001.

[27] A.V. Krajnikov, A.S. Drachinskiy, V.N. Slyunyaev, Grain boundary segregation in recrystallized molybdenum alloys and its effect on brittle intergranular fracture, Int. J. Refract. Met. Hard Mater. 11 (1992) 175–180.

[28] P. Lejček, Grain boundary segregation in metals, Springer Berlin Heidelberg, 2010.

[29] M. Tuominen, S.P. Clough, Grain Boundary Segregation of Sulfur and Nitrogen in Sintered Molybdenum, Metall. Trans. A. 10A (1979) 127–129.

[30] D. Scheiber, R. Pippan, P. Puschnig, L. Romaner, Ab initio search for cohesion-enhancing impurity elements at grain boundaries in molybdenum and tungsten, Model. Simul. Mater. Sci. Eng. 24 (2016). doi:10.1088/0965-0393/24/8/085009.

[31] T. Watanabe, T. Murakami, S. Karashima, Misorientation dependence of grain boundary segregation, Scr. Metall. 12 (1978) 361–365. doi:10.1016/0036-9748(78)90300-9.

[32] K. Leitner (née Babinsky), P.J. Felfer, D. Holec, J. Cairney, W. Knabl, A. Lorich, H. Clemens, S. Primig, On grain boundary segregation in molybdenum materials, Mater. Des. 135 (2017) 204–212. doi:10.1016/j.matdes.2017.09.019.

[33] J.P. Hanson, A. Bagri, J. Lind, P. Kenesei, R.M. Suter, S. Gradečak, M.J. Demkowicz, Crystallographic character of grain boundaries resistant to hydrogen-assisted fracture in Ni-base alloy 725, Nat. Commun. 9 (2018) 1–11. doi:10.1038/s41467-018-05549-y.

[34] M.K. Miller, E.A. Kenik, M.S. Mousa, K.F. Russell, A.J. Bryhan, Improvement in the ductility of molybdenum alloys due to grain boundary segregation, Scr. Mater. 46 (2002) 299–303. doi:10.1016/S1359-6462(01)01242-8.

[35] A. V. Krajnikov, F. Morito, V.N. Slyunyaev, Impurity-induced embrittlement of heat-affected zone in welded mo-based alloys, Int. J. Refract. Met. Hard Mater. 15 (1997) 325–339. doi:10.1016/S0263-4368(97)87507-5.

[36] T. Kadokura, Y. Hiraoka, Y. Yamamoto, K. Okamoto, Change of Mechanical Property and Fracture Mode of Molybdenum by Carbon Addition, Mater. Trans. 51 (2010) 1296–1301. doi:10.2320/matertrans.M2009377.

[37] Y. Hiraoka, Significant Effect of Carbon Content in the Low-Temperature Fracture Behavior of Molybdenum, Mater. Trans. JIM. 31 (1990) 861–864.

[38] K. Tsuya, N. Aritomi, On the Effects of Vacuum Annealing and Carburizing on the Ductility of Coarse-Grained Molybdenum, J. Less-Common Met. 15 (1968) 245–257.

[39] A. Milner, T.R. Bergstrom, Ductility of sintered unworked molybdenum-carbon alloys, J. Less-Common Met. 12 (1967) 253–257.

[40] H. Lutz, F. Benesovsky, R. Kieffer, Versuche zur Desoxidation von Sintermolybdän mit Kohlenstoff, Bor und Silizium, J. Less-Common Met. Less-Common Met. 16 (1968) 249–264.

[41] B.A. Klypin, N.N. Morgunova, R.R. Lastochkin, Effect of small Boron additions on the properties of Mo-0.2Zr, Met. Sci. Heat Treat. 15 (1973) 773–776.

[42] Y. Hiraoka, M. Okada, H. Irie, Alloying to improve the properties of welded molybdenum, J. Nucl. Mater. 155–157 (1988) 381–385.

[43] M.K. Miller, H. Kurishita, APFIM characterization of grain boundary segregation in titanium carbide-doped molybdenum, J. Phys. IV Colloq. 6 (1996). doi:10.1051/jp4:1996543.

[44] R. Janish, T. Ochs, A. Merkle, C. Elsässer, Structure and Stability of Grain Boundaries in

Molybdenum with Segregated Carbon Impurities, MRS Proc. 578 (1999).

[45] A.M. Tahir, R. Janish, A. Hartmaier, Ab initio calculation of traction separation laws for a grain boundary in molybdenum with segregated C impurites Ab initio calculation of traction separation laws for a grain boundary in molybdenum with segregated, Model. Simul. Mater. Sci. Eng. 21 (2013) 075005. doi:10.1088/0965-0393/21/7/075005.

[46] T.N. Nowicki, J.-M. Penisson, M. Biscondi, Oxygen Segregation in 32° [001] Molybdenum Tilt Grain Boundary I. Segregation Sites Determination, J. Phys. Colloq. 49 (1988) 403–408. doi:10.1051/jphyscol:1988547.

[47] D. Scheiber, R. Pippan, P. Puschnig, A. Ruban, L. Romaner, Ab-initio search for cohesion-enhancing solute elements at grain boundaries in molybdenum and tungsten, Int. J. Refract. Met. Hard Mater. 60 (2016) 75–81. doi:10.1016/j.ijrmhm.2016.07.003.

[48] D. Scheiber, L. Romaner, R. Pippan, P. Puschnig, Impact of solute-solute interactions on grain boundary segregation and cohesion in molybdenum, Phys. Rev. Mater. 2 (2018). doi:10.1103/PhysRevMaterials.2.093609.

[49] D. Scheiber, L. Romaner, F.D. Fischer, J. Svoboda, Kinetics of grain boundary segregation in multicomponent systems – The example of a Mo-C-B-O system, Scr. Mater. 150 (2018) 110–114. doi:10.1016/j.scriptamat.2018.03.011.

[50] G. Dehm, B.N. Jaya, R. Raghavan, C. Kirchlechner, Overview on micro- and nanomechanical testing: New insights in interface plasticity and fracture at small length scales, Acta Mater. 142 (2018) 248–282. doi:10.1016/j.actamat.2017.06.019.

[51] W.C. Oliver, G.M. Pharr, An improved technique for determining hardness and elastic modulus using load and displacement sensing indentation experiments, J. Mater. Res. 7 (1992) 1564–1583. doi:10.1557/JMR.1992.1564.

[52] W.C. Oliver, J.B. Pethica, Method for continuous determination of the elastic stiffness of contact between two bodies, United States Patent 4,848,141, 1989.

[53] X. Li, B. Bhushan, A review of nanoindentation continuous stiffness measurement technique and its applications, Mater. Charact. 48 (2002) 11–36. doi:10.1016/S1044-5803(02)00192-4.

[54] W.D. Nix, H. Gao, Indentation size effects in crystalline materials: A law for strain gradient plasticity, J. Mech. Phys. Solids. 46 (1998) 411–425. doi:10.1016/S0022-

5096(97)00086-0.

[55] M. Rester, C. Motz, R. Pippan, Indentation across size scales – A survey of indentation-induced plastic zones in copper {1 1 1} single crystals, Scr. Mater. 59 (2008) 742–745. doi:10.1016/j.scriptamat.2008.06.003.

[56] V. Maier-Kiener, K. Durst, Advanced Nanoindentation Testing for Studying Strain-Rate Sensitivity and Activation Volume, JOM. 69 (2017) 2246–2255. doi:10.1007/s11837-017-2536-y.

[57] A. Leitner, V. Maier-Kiener, D. Kiener, Essential refinements of spherical nanoindentation protocols for the reliable determination of mechanical flow curves, Mater. Des. 146 (2018) 69–80. doi:10.1016/j.matdes.2018.03.003.

[58] A. Leitner, V. Maier-Kiener, D. Kiener, Extraction of Flow Behavior and Hall–Petch Parameters Using a Nanoindentation Multiple Sharp Tip Approach, Adv. Eng. Mater. 19 (2017) 1–9. doi:10.1002/adem.201600669.

[59] S. Pathak, D. Stojakovic, S.R. Kalidindi, Measurement of the local mechanical properties in polycrystalline samples using spherical nanoindentation and orientation imaging microscopy, Acta Mater. 57 (2009) 3020–3028. doi:10.1016/j.actamat.2009.03.008.

[60] S. Kobayashi, S. Tsurekawa, T. Watanabe, Grain boundary hardening and triple junction hardening in polycrystalline molybdenum, Acta Mater. 53 (2005) 1051–1057. doi:10.1016/j.actamat.2004.11.002.

[61] M. Braunovic, C.W. Haworth, On the phenomenon of grain-boundary hardening in iron, J. Mater. Sci. 9 (1974) 809–820. doi:10.1007/BF00761801.

[62] T. Watanabe, S. Kitamura, S. Karashima, Grain boundary hardening and segregation in alpha Iron-Tin alloy, Acta Metall. 28 (1980) 455–463. doi:10.1016/0001-6160(80)90135-2.

[63] Y.T. Chou, B.C. Cai, A.D. Romig, L.S. Lin, Correlation between grain-boundary hardening and grain-boundary energy in niobium bicrystals, Philos. Mag. A. 47 (1983) 363–368. doi:10.1080/01418618308245232.

[64] S.R. Kalidindi, S.J. Vachhani, Mechanical characterization of grain boundaries using nanoindentation, Curr. Opin. Solid State Mater. Sci. 18 (2014) 196–204. doi:10.1016/j.cossms.2014.05.002.

[65] Y.M. Soifer, A. Verdyan, M. Kazakevich, E. Rabkin, Nanohardness of copper in the vicinity of grain boundaries, Scr. Mater. 47 (2002) 799–804. doi:10.1016/S1359-6462(02)00284-1.

[66] G.Z. Voyiadjis, C. Zhang, The mechanical behavior during nanoindentation near the grain boundary in a bicrystal FCC metal, Mater. Sci. Eng. A. 621 (2015) 218–228. doi:10.1016/j.msea.2014.10.070.

[67] W.A. Soer, K.E. Aifantis, J.T.M. De Hosson, Incipient plasticity during nanoindentation at grain boundaries in body-centered cubic metals, Acta Mater. 53 (2005) 4665–4676. doi:10.1016/j.actamat.2005.07.001.

[68] T. Eliash, M. Kazakevich, V.N. Semenov, E. Rabkin, Nanohardness of molybdenum in the vicinity of grain boundaries and triple junctions, Acta Mater. 56 (2008) 5640–5652. doi:10.1016/j.actamat.2008.07.036.

[69] S.J. Vachhani, R.D. Doherty, S.R. Kalidindi, Studies of grain boundary regions in deformed polycrystalline aluminum using spherical nanoindentation, Int. J. Plast. 81 (2016) 87–101. doi:10.1016/j.ijplas.2016.01.001.

[70] S. Pathak, J. Michler, K. Wasmer, S.R. Kalidindi, Studying grain boundary regions in polycrystalline materials using spherical nano-indentation and orientation imaging microscopy, J. Mater. Sci. 47 (2012) 815–823. doi:10.1007/s10853-011-5859-z.

[71] J.S. Weaver, D.R. Jones, N. Li, N. Mara, S. Fensin, G.T. Gray, Quantifying heterogeneous deformation in grain boundary regions on shock loaded tantalum using spherical and sharp tip nanoindentation, Mater. Sci. Eng. A. 737 (2018) 373–382. doi:10.1016/j.msea.2018.09.075.

[72] W.W. Gerberich, S.K. Venkataraman, H. Huang, S.E. Harvey, D.L. Kohlstedt, The injection of plasticity by millinewton contacts, Acta Metall. Mater. 43 (1995) 1569–1576. doi:10.1016/0956-7151(94)00351-H.

[73] M. Göken, M. Kempf, Pop-ins in nanoindentations - The initial yield point, Zeitschrift f. Met. Res. Adv. Tech. 92 (2001) 1061–1067.

[74] H. Bei, Y.F. Gao, S. Shim, E.P. George, G.M. Pharr, Strength differences arising from homogeneous versus heterogeneous dislocation nucleation, Phys. Rev. B - Condens. Matter Mater. Phys. 77 (2008) 2–5. doi:10.1103/PhysRevB.77.060103.

[75] Z. Wang, H. Bei, E.P. George, G.M. Pharr, Influences of surface preparation on nanoindentation pop-in in single-crystal Mo, Scr. Mater. 65 (2011) 469–472. doi:10.1016/j.scriptamat.2011.05.030.

[76] T. Ohmura, K. Tsuzaki, Analysis of grain boundary effect of bulk polycrystalline materials through nanomechanical characterization, J. Phys. D. Appl. Phys. 41 (2008). doi:10.1088/0022-3727/41/7/074015.

[77] M.G. Wang, A.H.W. Ngan, Indentation strain burst phenomenon induced by grain boundaries in niobium, J. Mater. Res. 19 (2004) 2478–2486. doi:10.1557/JMR.2004.0316.

[78] Y. Shibutani, Y. Nakahama, Heterogeneous grain boundary effect to displacement bursts of a nanoindentation, Adv. Heterog. Mater. Mech. ICHMM-2008 (2008).

[79] T.B. Britton, D. Randman, A.J. Wilkinson, Nanoindentation study of slip transfer phenomenon at grain boundaries, J. Mater. Res. 24 (2009) 607–615. doi:10.1557/jmr.2009.0088.

[80] M.D. Uchic, D.M. Dimiduk, J.N. Florando, W.D. Nix, Sample dimensions influence strength and crystal plasticity, Science. 305 (2004) 986–989. doi:10.1126/science.1098993.

[81] R. Schwaiger, M. Weber, B. Moser, P. Gumbsch, O. Kraft, Mechanical assessment of ultrafine-grained nickel by microcompression experiment and finite element simulation, J. Mater. Res. 27 (2012) 266–277. doi:10.1557/jmr.2011.248.

[82] H. Zhang, B.E. Schuster, Q. Wei, K.T. Ramesh, The design of accurate micro-compression experiments, Scr. Mater. 54 (2006) 181–186. doi:10.1016/j.scriptamat.2005.06.043.

[83] D.J. Dunstan, A.J. Bushby, The scaling exponent in the size effect of small scale plastic deformation, Int. J. Plast. 40 (2013) 152–162. doi:10.1016/j.ijplas.2012.08.002.

[84] D. Kiener, C. Motz, M. Rester, M. Jenko, G. Dehm, FIB damage of Cu and possible consequences for miniaturized mechanical tests, Mater. Sci. Eng. A. 459 (2007) 262–272. doi:10.1016/j.msea.2007.01.046.

[85] H. Bei, S. Shim, M.K. Miller, G.M. Pharr, E.P. George, Effects of focused ion beam milling on the nanomechanical behavior of a molybdenum-alloy single crystal, Appl. Phys. Lett. 91 (2007) 111915. doi:10.1063/1.2784948.

[86] P.J. Imrich, C. Kirchlechner, C. Motz, G. Dehm, Differences in deformation behavior of bicrystalline Cu micropillars containing a twin boundary or a large-angle grain boundary, Acta Mater. 73 (2014) 240–250. doi:10.1016/j.actamat.2014.04.022.

[87] N. V. Malyar, G. Dehm, C. Kirchlechner, Strain rate dependence of the slip transfer through a penetrable high angle grain boundary in copper, Scr. Mater. 138 (2017) 88–91. doi:10.1016/j.scriptamat.2017.05.042.

[88] J.P. Liebig, S. Krauß, M. Göken, B. Merle, Influence of stacking fault energy and dislocation character on slip transfer at coherent twin boundaries studied by micropillar compression, Acta Mater. 154 (2018) 261–272. doi:10.1016/j.actamat.2018.05.037.

[89] N. V. Malyar, B. Grabowski, G. Dehm, C. Kirchlechner, Dislocation slip transmission through a coherent Σ3{111} copper twin boundary: Strain rate sensitivity, activation volume and strength distribution function, Acta Mater. 161 (2018) 412–419. doi:10.1016/j.actamat.2018.09.045.

[90] N. V. Malyar, J.S. Micha, G. Dehm, C. Kirchlechner, Size effect in bi-crystalline micropillars with a penetrable high angle grain boundary, Acta Mater. 129 (2017) 312–320. doi:10.1016/j.actamat.2017.03.003.

[91] N. Kheradmand, J. Dake, A. Barnoush, H. Vehoff, Novel methods for micromechanical examination of hydrogen and grain boundary effects on dislocations, Philos. Mag. 92 (2012) 3216–3230. doi:10.1080/14786435.2012.690939.

[92] N. Kheradmand, H. Vehoff, A. Barnoush, An insight into the role of the grain boundary in plastic deformation by means of a bicrystalline pillar compression test and atomistic simulation, Acta Mater. 61 (2013) 7454–7465. doi:10.1016/j.actamat.2013.08.056.

[93] N. Kheradmand, A.F. Knorr, M. Marx, Y. Deng, Microscopic incompatibility controlling plastic deformation of bicrystals, Acta Mater. 106 (2016) 219–228. doi:10.1016/j.actamat.2016.01.006.

[94] J.S. Weaver, N. Li, N.A. Mara, D.R. Jones, H. Cho, C.A. Bronkhorst, S.J. Fensin, G.T. Gray, Slip transmission of high angle grain boundaries in body-centered cubic metals: Micropillar compression of pure Ta single and bi-crystals, Acta Mater. 156 (2018) 356–368. doi:10.1016/j.actamat.2018.06.046.

[95] M. Heller, J.S.K.L. Gibson, R. Pei, S. Korte-Kerzel, Deformation of µm- and mm-sized

Fe2.4wt%Si single- and bi-crystals with a high angle grain boundary at room temperature, Acta Mater. 194 (2020) 452–463. doi:10.1016/j.actamat.2020.04.011.

[96] S. Wurster, C. Motz, M. Jenko, R. Pippan, Micrometer-sized specimen preparation based on ion slicing technique, Adv. Eng. Mater. 12 (2010) 61–64. doi:10.1002/adem.200900263.

[97] D. Di Maio, S.G. Roberts, Measuring fracture toughness of coatings using focused-ion-beam-machined microbeams, J. Mater. Res. 20 (2005) 299–302. doi:10.1557/JMR.2005.0048.

[98] D.E.J. Armstrong, M.E. Rogers, S.G. Roberts, Micromechanical testing of stress corrosion cracking of individual grain boundaries, Scr. Mater. 61 (2009) 741–743. doi:10.1016/j.scriptamat.2009.06.017.

[99] M.T. Lessmann, A. Calvo, C.D. Hardie, M. Porton, N. Ordás, C. García-Rosales, P.M. Mummery, Fracture strength testing of a self-passivating tungsten alloy at the micrometre scale, Philos. Mag. 96 (2016) 3570–3585. doi:10.1080/14786435.2016.1177229.

[100] C. Motz, T. Schöberl, R. Pippan, Mechanical properties of micro-sized copper bending beams machined by the focused ion beam technique, Acta Mater. 53 (2005) 4269–4279. doi:10.1016/j.actamat.2005.05.036.

[101] M.W. Kapp, C. Kirchlechner, R. Pippan, G. Dehm, Importance of dislocation pile-ups on the mechanical properties and the Bauschinger effect in microcantilevers, J. Mater. Res. 30 (2015) 791–797. doi:10.1557/jmr.2015.49.

[102] S. Wurster, C. Motz, R. Pippan, Characterization of the fracture toughness of micro-sized tungsten single crystal notched specimens, Philos. Mag. 92 (2012) 1803–1825. doi:10.1080/14786435.2012.658449.

[103] B.N. Jaya, C. Kirchlechner, G. Dehm, Can microscale fracture tests provide reliable fracture toughness values? A case study in silicon, J. Mater. Res. 30 (2015) 686–698. doi:10.1557/jmr.2015.2.

[104] J. Ast, B. Merle, K. Durst, M. Göken, Fracture toughness evaluation of NiAl single crystals by microcantilevers - A new continuous J-integral method, J. Mater. Res. 31 (2016) 3786–3794. doi:10.1557/jmr.2016.393.

[105] M. Alfreider, D. Kozic, O. Kolednik, D. Kiener, In-situ elastic-plastic fracture mechanics on the microscale by means of continuous dynamical testing, Mater. Des. 148 (2018) 177–187. doi:10.1016/j.matdes.2018.03.051.

[106] T. Sumigawa, T. Shishido, T. Murakami, T. Kitamura, Interface crack initiation due to nano-scale stress concentration, Mater. Sci. Eng. A. 527 (2010) 4796–4803. doi:10.1016/j.msea.2010.04.002.

[107] D.E.J. Armstrong, A.J. Wilkinson, S.G. Roberts, Micro-mechanical measurements of fracture toughness of bismuth embrittled copper grain boundaries, Philos. Mag. Lett. 91 (2011) 394–400. doi:10.1080/09500839.2011.573813.

[108] D. Kupka, E.T. Lilleodden, Mechanical Testing of Solid-Solid Interfaces at the Microscale, Exp. Mech. 52 (2012) 649–658. doi:10.1007/s11340-011-9530-z.

[109] R. Konetschnik, R. Daniel, R. Brunner, D. Kiener, Selective interface toughness measurements of layered thin films, AIP Adv. 7 (2017) 035307. doi:10.1063/1.4978337.

[110] H. Chan, S.G. Roberts, J. Gong, Micro-scale fracture experiments on zirconium hydrides and phase boundaries, J. Nucl. Mater. 475 (2016) 105–112. doi:10.1016/j.jnucmat.2016.03.026.

[111] R. Ding, J. Gong, A.J. Wilkinson, I.P. Jones, A study of dislocation transmission through a grain boundary in hcp Ti-6Al using micro-cantilevers, Acta Mater. 103 (2016) 416–423. doi:10.1016/j.actamat.2015.10.023.

[112] Y. Zou, P. Okle, H. Yu, T. Sumigawa, T. Kitamura, S. Maiti, W. Steurer, R. Spolenak, Fracture properties of a refractory high-entropy alloy: In situ micro-cantilever and atom probe tomography studies, Scr. Mater. 128 (2017) 95–99. doi:10.1016/j.scriptamat.2016.09.036.

[113] T. Hajilou, Y. Deng, N. Kheradmand, A. Barnoush, Hydrogen enhanced cracking studies on Fe-3wt%Si single and bi-crystal microcantilevers, Philos. Trans. R. Soc. A Math. Phys. Eng. Sci. 375 (2017). doi:10.1098/rsta.2016.0410.

[114] J.D. Livingston, B. Chalmers, Multiple slip in bicrystal deformation, Acta Metall. 5 (1957) 322–327. doi:10.1016/0001-6160(57)90044-5.

[115] Z. Shen, R.H. Wagoner, W.A.T. Clark, Dislocation pile-up and grain boundary interactions in 304 stainless steel, Scr. Metall. 20 (1986) 921–926. doi:10.1016/0036-

9748(86)90467-9.

[116] Z. Shen, R.H. Wagoner, W.A.T. Clark, Dislocation and grain boundary interactions in metals, Acta Metall. 36 (1988) 3231–3242. doi:10.1016/0001-6160(88)90058-2.

[117] L.C. Lim, R. Raj, The role of residual dislocation arrays in slip induced cavitation, migration and dynamic recrystallization at grain boundaries, Acta Metall. 33 (1985) 2205–2214. doi:10.1016/0001-6160(85)90182-8.

[118] L. Patriarca, W. Abuzaid, H. Sehitoglu, H.J. Maier, Slip transmission in bcc FeCr polycrystal, Mater. Sci. Eng. A. 588 (2013) 308–317. doi:10.1016/j.msea.2013.08.050.

[119] J. Luster, M.A. Morris, Compatibility of deformation in two-phase Ti-Al alloys: Dependence on microstructure and orientation relationships, Metall. Mater. Trans. A. 26 (1995) 1745–1756. doi:10.1007/BF02670762.

[120] E. Werner, W. Prantl, Slip transfer across grain and phase boundaries, Acta Metall. Mater. 38 (1990) 533–537. doi:10.1016/0956-7151(90)90159-E.

[121] T.B. Britton, A.J. Wilkinson, Stress fields and geometrically necessary dislocation density distributions near the head of a blocked slip band, Acta Mater. 60 (2012) 5773–5782. doi:10.1016/j.actamat.2012.07.004.

[122] S. Kondo, T. Mitsuma, N. Shibata, Y. Ikuhara, Direct observation of individual dislocation interaction processes with grain boundaries, Sci. Adv. 2 (2016). doi:10.1126/sciadv.1501926.

[123] T. Ohmura, A.M. Minor, E.A. Stach, J.W. Morris, Dislocation-grain boundary interactions in martensitic steel observed through in situ nanoindentation in a transmission electron microscope, J. Mater. Res. 19 (2004) 3626–3632. doi:10.1557/JMR.2004.0474.

[124] T.R. Bieler, P. Eisenlohr, F. Roters, D. Kumar, D.E. Mason, M.A. Crimp, D. Raabe, The role of heterogeneous deformation on damage nucleation at grain boundaries in single phase metals, Int. J. Plast. 25 (2009) 1655–1683. doi:10.1016/j.ijplas.2008.09.002.

[125] B. Zhu, X. Xue, H. Kou, R. Dong, J. Li, The nucleation of microcracks under tensile stress in multi-phase high Nb-containing TiAl alloys, Intermetallics. 106 (2019) 13–19. doi:10.1016/j.intermet.2018.12.006.

[126] A.F. Knorr, M. Marx, F. Schaefer, Crack initiation at twin boundaries due to slip system

mismatch, Scr. Mater. 94 (2015) 48–51. doi:10.1016/j.scriptamat.2014.09.015.

[127] T.R. Bieler, S.C. Sutton, B.E. Dunlap, Z.A. Keith, P. Eisenlohr, M.A. Crimp, B.L. Boyce, Grain boundary responses to heterogeneous deformation in tantalum polycrystals, JOM. 66 (2014) 121–128. doi:10.1007/s11837-013-0821-y.

[128] S. Jakob, A. Leitner, A. Lorich, M. Eidenberger-Schober, W. Knabl, R. Pippan, H. Clemens, V. Maier-Kiener, Influence of crystal orientation and Berkovich tip rotation on the mechanical characterization of grain boundaries in molybdenum, Mater. Des. 182 (2019) 107998. doi:10.1016/j.matdes.2019.107998.

[129] S. Jakob, A. Hohenwarter, A. Lorich, W. Knabl, R. Pippan, H. Clemens, V. Maier-Kiener, Assessment of grain boundary cohesion of technically pure and boron micro-doped molybdenum via meso-scale three-point-bending experiments, Mater. Des. 207 (2021) 109848. doi:10.1016/j.matdes.2021.109848.

[130] K. Huber, M. O'Sullivan, M. Eidenberger-Schober, R. Storf, Sintered molybdenum part, International Patent WO 2019/060932 A1, 2019. https://patentscope.wipo.int/search/en/detail.jsf?docId=WO2019060932.

[131] G.W.C. Kaye, T.H. Laby, Tables of physical and chemical constants, 15th ed., Longman, London, UK, 1993.

[132] C.A. Schneider, W.S. Rasband, K.W. Eliceiri, NIH Image to ImageJ: 25 years of image analysis, Nat. Methods. 9 (2012) 671–675. doi:10.1038/nmeth.2089.

[133] F. Bachmann, R. Hielscher, H. Schaeben, Texture Analysis with MTEX – Free and Open Source Software Toolbox, Solid State Phenom. 160 (2010) 63–68. doi:10.4028/www.scientific.net/SSP.160.63.

[134] K. Babinsky, R. De Kloe, H. Clemens, S. Primig, A novel approach for site-specific atom probe specimen preparation by focused ion beam and transmission electron backscatter diffraction, Ultramicroscopy. 144 (2014) 9–18. doi:10.1016/j.ultramic.2014.04.003.

[135] M. Thuvander, H.-O. Andrén, APFIM Studies of Grain and Phase Boundaries, Mater. Charact. 44 (2000) 87–100. doi:10.1016/S1044-5803(99)00052-2.

[136] B.W. Krakauer, D.N. Seidman, Absolute atomic-scale measurements of the Gibbsian interfacial excess of solute at internal interfaces, Phys. Rev. B. 48 (1993) 6724–6727.

doi:10.1103/PhysRevB.48.6724.

[137] K. Babinsky, J. Weidow, W. Knabl, A. Lorich, H. Leitner, S. Primig, Atom probe study of grain boundary segregation in technically pure molybdenum, Mater. Charact. 87 (2014) 95–103. doi:10.1016/j.matchar.2013.11.001.

[138] J.O. Andersson, T. Helander, L. Höglund, P. Shi, B. Sundman, Thermo-Calc & DICTRA, computational tools for materials science, Calphad Comput. Coupling Phase Diagrams Thermochem. 26 (2002) 273–312. doi:10.1016/S0364-5916(02)00037-8.

[139] B.A. Vandyshev, A.S. Panov, Phosphorus diffusion in niobium and molybdenum, Phys. Met. Met. (English Transl.). 26 (1968) 517–521.

[140] K. Babinsky, S. Primig, W. Knabl, A. Lorich, H. Clemens, S. Sackl, Korngrenzen in technisch reinem Molybdän: Eine atomare Untersuchung mittels Atomsondentomographie, Oral Present., 62. Metallkunde-Kolloquium. (2016).

[141] R. Smith, D. Christopher, S.D. Kenny, A. Richter, B. Wolf, Defect generation and pileup of atoms during nanoindentation of Fe single crystals, Phys. Rev. B. 67 (2003) 245405. doi:10.1103/PhysRevB.67.245405.

[142] M.M. Biener, J. Biener, A.M. Hodge, A. V. Hamza, Dislocation nucleation in bcc Ta single crystals studied by nanoindentation, Phys. Rev. B. 76 (2007) 165422. doi:10.1103/PhysRevB.76.165422.

[143] C. Zambaldi, Y. Yang, T.R. Bieler, D. Raabe, Orientation informed nanoindentation of α-titanium: Indentation pileup in hexagonal metals deforming by prismatic slip, J. Mater. Res. 27 (2012) 356–367. doi:10.1557/jmr.2011.334.

[144] W.Z. Yao, J.H. You, Berkovich nanoindentation study of monocrystalline tungsten: a crystal plasticity study of surface pile-up deformation, Philos. Mag. 97 (2017) 1418–1435. doi:10.1080/14786435.2017.1299237.

[145] J. Hu, Y. Zhang, W. Sun, T. Zhang, Nanoindentation-Induced Pile-Up in the Residual Impression of Crystalline Cu with Different Grain Size, Crystals. 8 (2017) 9. doi:10.3390/cryst8010009.

[146] R. Zauter, F. Petry, M. Bayerlein, C. Sommer, H.-J. Christ, H. Mughrabi, Electron channelling contrast as a supplementary method for microstructural investigations in deformed metals, Philos. Mag. A. 66 (1992) 425–436.

doi:10.1080/01418619208201567.

[147] J. Wu, P.J. Wray, C.I. Garcia, M. Hua, A.J. Deardo, Image Quality Analysis: A New Method of Characterizing Microstructures, ISIJ Int. 45 (2005) 254–262. doi:10.2355/isijinternational.45.254.

[148] S. Zaefferer, P. Romano, F. Friedel, EBSD as a tool to identify and quantify bainite and ferrite in low-alloyed Al-TRIP steels, J. Microsc. 230 (2008) 499–508. doi:10.1111/j.1365-2818.2008.02010.x.

[149] G.M. Pharr, J.H. Strader, W.C. Oliver, Critical issues in making small-depth mechanical property measurements by nanoindentation with continuous stiffness measurement, J. Mater. Res. 24 (2009) 653–666. doi:10.1557/jmr.2009.0096.

[150] N. Gane, F.P. Bowden, Microdeformation of solids, J. Appl. Phys. 39 (1968) 1432–1435. doi:10.1063/1.1656376.

[151] K.L. Johnson, Contact mechanics, Cambridge University Press, Cambridge, UK, 1985.

[152] W.W. Gerberich, D.E. Kramer, N.I. Tymiak, A.A. Volinsky, D.F. Bahr, M.D. Kriese, Nanoindentation-induced defect-interface interactions: phenomena, methods and limitations, Acta Mater. 47 (1999) 4115–4123. doi:10.1016/S1359-6454(99)00270-0.

[153] J.R. Morris, H. Bei, G.M. Pharr, E.P. George, Size effects and stochastic behavior of nanoindentation pop in, Phys. Rev. Lett. 106 (2011) 165502. doi:10.1103/PhysRevLett.106.165502.

[154] C.R. Krenn, D. Roundy, M.L. Cohen, D.C. Chrzan, J.W. Morris, Connecting atomistic and experimental estimates of ideal strength, Phys. Rev. B. 65 (2002) 134111. doi:10.1103/PhysRevB.65.134111.

[155] M.B. Lowry, D. Kiener, M.M. LeBlanc, C. Chisholm, J.N. Florando, J.W. Morris, A.M. Minor, Achieving the ideal strength in annealed molybdenum nanopillars, Acta Mater. 58 (2010) 5160–5167. doi:10.1016/j.actamat.2010.05.052.

[156] J.L. Hay, W.C. Oliver, A. Bolshakov, G.M. Pharr, Using the ratio of loading slope and elastic stiffness to predict pile-up and constraint factor during indentation, Mat. Res. Soc. Symp. Proc. 522 (1998) 101–106.

[157] Y.J. Park, G.M. Pharr, Nanoindentation with spherical indenters: finite element studies

of deformation in the elastic-plastic transition regime, Thin Solid Films. 447–448 (2004) 246–250. doi:10.1016/S0040-6090.

[158] D.L. Joslin, W.C. Oliver, A new method for analyzing data from continuous depth-sensing microindentation tests, J. Mater. Res. 5 (1990) 123–126. doi:10.1557/JMR.1990.0123.

[159] F.H. Featherston, J.R. Neighbours, Elastic constants of tantalum, tungsten, and molybdenum, Phys. Rev. 130 (1963) 1324–1333. doi:10.1103/PhysRev.130.1324.

[160] C.R. Weinberger, B.L. Boyce, C.C. Battaile, Slip planes in bcc transition metals, Int. Mater. Rev. 58 (2013) 296–314. doi:10.1179/1743280412Y.0000000015.

[161] H. Yu, S. Das, H. Yu, P. Karamched, E. Tarleton, F. Hofmann, Orientation dependence of the nano-indentation behaviour of pure Tungsten, Scr. Mater. 189 (2020) 135–139. doi:10.1016/j.scriptamat.2020.08.014.

[162] W. Xia, G. Dehm, S. Brinckmann, Insight into indentation-induced plastic flow in austenitic stainless steel, J. Mater. Sci. (2020). doi:10.1007/s10853-020-04646-y.

[163] D. Kiener, R. Pippan, C. Motz, H. Kreuzer, Microstructural evolution of the deformed volume beneath microindents in tungsten and copper, Acta Mater. 54 (2006) 2801–2811. doi:10.1016/j.actamat.2006.02.024.

[164] N. Zaafarani, D. Raabe, R.N. Singh, F. Roters, S. Zaefferer, Three-dimensional investigation of the texture and microstructure below a nanoindent in a Cu single crystal using 3D EBSD and crystal plasticity finite element simulations, Acta Mater. 54 (2006) 1863–1876. doi:10.1016/j.actamat.2005.12.014.

[165] X. Zhang, S. Lu, B. Zhang, X. Tian, Q. Kan, G. Kang, Dislocation–grain boundary interaction-based discrete dislocation dynamics modeling and its application to bicrystals with different misorientations, Acta Mater. 202 (2021) 88–98. doi:10.1016/j.actamat.2020.10.052.

[166] S. Jakob, A. Lorich, M. Eidenberger-Schober, W. Knabl, H. Clemens, V. Maier-Kiener, Microstructural characterization of molybdenum grain boundaries by micropillar compression testing and atom probe tomography, Pract. Metallogr. 56 (2019) 776–786. doi:10.3139/147.110567.

[167] S. Brinckmann, K. Matoy, C. Kirchlechner, G. Dehm, On the influence of microcantilever

pre-crack geometries on the apparent fracture toughness of brittle materials, Acta Mater. 136 (2017) 281–287. doi:10.1016/j.chb.2018.07.039.

[168] T.R. Bieler, R. Alizadeh, M. Peña-Ortega, J. LLorca, An analysis of (the lack of) slip transfer between near-cube oriented grains in pure Al, Int. J. Plast. (2019) 1–22. doi:10.1016/J.IJPLAS.2019.02.014.

[169] S. Zaefferer, J.C. Kuo, Z. Zhao, M. Winning, D. Raabe, On the influence of the grain boundary misorientation on the plastic deformation of aluminum bicrystals, Acta Mater. 51 (2003) 4719–4735. doi:10.1016/S1359-6454(03)00259-3.

[170] T.C. Lee, I.M. Robertson, H.K. Birnbaum, An In Situ transmission electron microscope deformation study of the slip transfer mechanisms in metals, Metall. Trans. A. 21 (1990) 2437–2447. doi:10.1007/BF02646988.

[171] J. Kacher, B.P. Eftink, B. Cui, I.M. Robertson, Dislocation interactions with grain boundaries, Curr. Opin. Solid State Mater. Sci. 18 (2014) 227–243. doi:10.1016/j.cossms.2014.05.004.

[172] F. Javaid, H. Pouriayevali, K. Durst, Dislocation–grain boundary interactions: recent advances on the underlying mechanisms studied via nanoindentation testing, J. Mater. Res. (2021). doi:10.1557/s43578-020-00096-z.

[173] T. Bieler, R.L. Goetz, S.L. Semiatin, Anisotropic plasticity and cavity growth during upset forging of Ti-6Al-4V, Mater. Sci. Eng. A. 405 (2005) 201–213. doi:10.1016/j.msea.2005.05.064.

[174] T.R. Bieler, A. Fallahi, B.C. Ng, D. Kumar, M.A. Crimp, B.A. Simkin, A. Zamiri, F. Pourboghrat, D.E. Mason, Fracture initiation/propagation parameters for duplex TiAl grain boundaries based on twinning, slip, crystal orientation, and boundary misorientation, Intermetallics. 13 (2005) 979–984. doi:10.1016/j.intermet.2004.12.013.

[175] J.A. Querin, J.A. Schneider, M.F. Horstemeyer, Analysis of micro void formation at grain boundary triple points in monotonically strained AA6022-T43 sheet metal, Mater. Sci. Eng. A. 463 (2007) 101–106. doi:10.1016/j.msea.2006.10.167.

[176] J. Reiser, A. Hartmaier, Elucidating the dual role of grain boundaries as dislocation sources and obstacles and its impact on toughness and brittle-to-ductile transition, Sci.

Rep. 10 (2020) 1–18. doi:10.1038/s41598-020-59405-5.

[177] C. Bonnekoh, U. Jäntsch, J. Hoffmann, H. Leiste, A. Hartmaier, D. Weygand, A. Hoffmann, J. Reiser, The brittle-to-ductile transition in cold rolled tungsten plates: Impact of crystallographic texture, grain size and dislocation density on the transition temperature, Int. J. Refract. Met. Hard Mater. 78 (2019) 146–163. doi:10.1016/j.ijrmhm.2018.09.010.

[178] D. Wolf, Correlation between the energy and structure of grain boundaries in b.c.c. metals. II. Symmetrical tilt boundaries, Philos. Mag. A. 62 (1990) 447–464. doi:10.1080/01418619008244790.

[179] F. Schaefer, E.P.W. Lang, M. Bick, A.F. Knorr, M. Marx, C. Motz, Assessing the intergranular crack initiation probability of a grain boundary distribution by an experimental misalignment study of adjacent slip systems, Procedia Struct. Integr. 5 (2017) 547–554. doi:10.1016/j.prostr.2017.07.161.

[180] D. Scheiber, L. Romaner, F.D. Fischer, J. Svoboda, Kinetics of grain boundary segregation in multicomponent systems – The example of a Mo-C-B-O system, Scr. Mater. 150 (2018) 110–114. doi:10.1016/j.scriptamat.2018.03.011.